FINAL REPORT

MODULATION-INDUCING RETRODIRECTIVE OPTICAL SYSTEM (MIROS)

Design Development (Phase II)
14 January 1966
Contract NAS5-9716)

Prepared by

Electro-Optical Laboratory
Space and Information Systems Division
North American Aviation, Incorporated
Downey, California

for

National Aeronautics and Space Administration
Goddard Space Flight Center
Greenbelt, Maryland

ACCESSION NUMBER							DOCUMENT SECURITY CLASSIFICATION UNCLASSIFIED	

TITLE OF DOCUMENT

FINAL REPORT, MODULATION-INDUCING RETRODIRECTIVE OPTICAL SYSTEM (MIROS), DESIGN DEVELOPMENT (PHASE II)

LIBRARY USE ONLY

AUTHOR(S)

ELECTRO-OPTICAL LABORATORY

CODE	ORIGINATING AGENCY AND OTHER SOURCES	DOCUMENT NUMBER
	SPACE AND INFORMATION SYSTEMS DIV. OF NAA	SID65-1026

PUBLICATION DATE
14JAN66

CONTRACT NUMBER
NAS5-9716

DESCRIPTIVE TERMS

ABSTRACT

THE DESIGN DEVELOPMENT OF MIROS, A LIGHTWEIGHT, LOW-POWER OPTICAL SYSTEM CAPABLE OF TRANSMITTING INFORMATION TO A REQUESTING SOURCE WITHOUT UNDETECTED EAVESDROPPING, IS DISCUSSED.

THE EXPERIMENTAL DEVELOPMENT OF A SUITABLE MEMBRANE MATERIAL, MODULATION BUTTON FABRICATION TECHNIQUES, AND TESTING PROGRAMS ARE COVERED IN THIS DOCUMENT.

FINAL REPORT

MODULATION-INDUCING RETRODIRECTIVE OPTICAL SYSTEM (MIROS)

Design Development (Phase II)
14 January 1966
Contract NAS5-9716)

Prepared by

Electro-Optical Laboratory
Space and Information Systems Division
North American Aviation, Incorporated
Downey, California

for

National Aeronautics and Space Administration
Goddard Space Flight Center
Greenbelt, Maryland

SUMMARY

The modulation-inducing retrodirective optical system (MIROS) concept was initiated by NASA. Its implementation requires development of a means for modulating the return beam from a retrodirective reflector. The performance and design goals for this study were a frequency bandwidth of 20 kcps, a 50-percent depth of modulation, 10 arc-seconds return beamwidth, and an effective aperture area of 100 square centimeters when used 20 degrees off axis.

A prior Phase I Program investigated the optical, mechanical, and electrical properties of a corner reflector containing an array of optical modulating elements on one of its three surfaces. The critical problem studied was the technology of fabricating the modulating elements. The modulating element was a capacitor with a stretched, aluminized Mylar membrane forming one capacitor plate and an etched, aluminized, fused-silica disc forming the other plate. These plates are electrically driven as a single-ended configuration. The electrostatic forces deflect the membrane from its normal, optically flat position, resulting in an intensity modulation of the retrodirected energy in the far-field pattern. It was discovered that pressurization of the assembly chamber would significantly extend the bandwidth of the modulating element above its vacuum resonant frequency. This Phase II Program was conducted to extend the developments initiated in Phase I. It also included new areas of study and experimentation.

Several new membrane materials and membrane fabrication techniques were evaluated relative to the goals for a MIROS retromodulator. It was found that acceptable flatness and optical quality could be achieved with an organic Pellicle membrane, but its vacuum resonant frequency was much lower than metallic membranes. Several 1/10-mil metallic membranes were tested. Vacuum resonant frequencies of 12 kcps were reliably obtained with 1/10-mil Havar, a low-iron stainless steel. The specular reflectivity of Havar membranes was measured to be only 7 percent, relative to that of a high-quality optical flat. An attempt to mechanically polish the surface produced a small, but inadequate improvement of about 2 percent. It was considered likely that electropolishing would have produced additional improvement in specular reflectivity, but this was not tried.

A replication process involving vacuum deposition on an optical flat was used to produce a few membranes of nickel with a gold reflecting surface. Test results showed nearly ideal optical properties over the full 2-cm aperture. The measured specular reflectivity was 80 percent relative to a quality optical flat. The vacuum resonance frequencies obtainable with a nickel film are, of course, lower than that from Havar. The success in obtaining a membrane of high optical quality indicates that if a high value of vacuum resonant frequency were not a crucial requirement, further effort might quickly yield a design that meets all MIROS performance goals.

The techniques devised for the fabrication of the precision optical components of modulator elements proved satisfactory. Pilot production quantities, produced in the NAA optical shop, are uniform in height to within 500 Angstroms (1/10 wave). Their modulating mounting surfaces are parallel to their bases to within 0.5 arc-seconds, and the modulating mounting surface of each element is flat to within 1/10 wavelength of visible light. The manufacturing cost for these components in small quantities would be only $50 per modulator element.

The ability to hold these tolerances is significant because, neglecting other optical tolerances, the resulting complete MIROS retro reflector will then have a return beamwidth less than that corresponding to the individual modulator element dimension (2 cm, 10 arc-seconds).

The theory of the effect of pressurization on bandwidth and driving power was developed and experimentally verified to frequencies of about 20 kcps. Theoretical extrapolation of these data showed that a 90-kcps information bandwidth would be obtained at one atmosphere of pressure. The required drive power increases, however, with the square of the bandwidth as would be expected on fundamental grounds for any modulation technique. It should also be clear that if the bandwidth is extended significantly by this means, then the resonant frequency is essentially determined by the membrane mass and is independent of its tension. This follows by noting that the restoring force acting on the membrane is dominantly due to compression of the confined gas.

With the single-ended drive configuration under study, the driving force is proportional to the square of the applied voltage. This requires a bias voltage that considerably exceeds the signal drive voltage to obtain an adequately linear relationship between signal voltage and membrane displacement, i.e., acceptably low modulation distortion. Unfortunately, however, there is an additional requirement for the bias voltage. The membrane must be biased to such a curvature that the far-field intensity

SID 65-1026

is reduced to half that of the undeflected, flat membrane. The received intensity can then be linearly modulated at a high modulation index (80 to 90 percent). The bias voltage required to obtain this curvature is proportional to membrane tension and is independent of pressurization. This low-bias voltage requirement conflicts with the aforementioned high-voltage bias required to achieve large-bandwidth, low-distortion performance.

The net conclusion from this study is that, assuming further work would yield membranes with the mechanical properties of Havar combined with the optical properties of replicated nickel, the resulting overall performance would approximately meet the stated MIROS goals (return beamwidth of 10 arc seconds, approximately 20 kcps bandwidth, and effective aperture area of 100 sq cm). A modulation index of 42 percent would be obtained with 18 percent distortion; and higher distortion would result with a higher modulation index. In view of these remaining difficulties, in relation to the projected resultant performances, further work along this direction is not recommended.

Subsequent to completion of this program, a project review revealed a new approach. The fundamental difficulty with the approach described herein is the square law relationship between signal drive voltage and membrane deflection. This problem is eliminated in commercial electrostatic speakers by employing a push-pull configuration. A push-pull electro-mechanical configuration eliminates the need for high membrane tension (or vacuum resonant frequency), and should permit the use of replicated membranes. This new approach could be the most fruitful for continued development of the MIROS retromodulators.

Theoretical, comparative analyses were also performed on each of the following:

1. Deformable film versus piezoelectric modulators

2. Modulation by use of an interferometer to change a surface's reflectivity versus modulation by membrane deformation

3. Cube corner configuration with driven membranes (MIROS) versus a spherical reflector-corrector configuration employing piezoelectric drive (SMIROS).

It was demonstrated by analysis that the voltage and power requirements for retromodulators employing the deformable film or a piezoelectric drive depend in the same way upon depth of modulation, element area,

and modulation bandwidth. A PZT-5 piezoelectric element requires, however, approximately three times as much voltage and twenty times as much power as a membrane modulator element for the same deflecting surface area, bandwidth, and depth of modulation. The MIROS retro-reflector operates over a larger field of view than the spherical reflector-corrector configuration (SMIROS). The SMIROS configuration, however, can be designed to meet a smaller field of view requirement, and has a significantly lower requirement for the specular reflectivity character-istics of the driven mirror element. The critical problems to be studied in the use of piezoelectric material as a precision optical component are the stability and predictability of mechanical dimensions and piezoelectric parameters with temperature, time, and cycling of drive voltage.

An optically contacted MIROS corner reflector (without modulator subassemblies) was subcontracted to a supplier who had previously produced smaller corner reflector assemblies. The fabrication technique for the smaller units was found to be inadequate for the larger size. This subcontract was cancelled and the partially worked material was purchased at the supplier's material cost. Consequently, NAA was not able to deliver this component. This report describes a fabrication technique that will yield a satisfactory product. In view of its potential applications, it is recommended that the corner reflector be completed by this technique and evaluated by NASA.

CONTENTS

ILLUSTRATIONS

TABLES

INTRODUCTION

The modulation inducing retrodirective optical system (MIROS) concept, originated at the NASA Goddard Space Flight Center, imposes information-carrying modulation onto a light beam by varying the optical properties of a retrodirective reflector. With this approach, a receiving station directs an unmodulated beam of light at the MIROS transmitting station and receives the retroreflected light. By detecting the modulation resulting from the action of the MIROS retroreflector, the receiving station acquires the desired information.

The MIROS concept offers a number of unique advantages for space communication where power requirements, for example, must be kept to a minimum. (In most MIROS communication link applications, the laser can be located on the ground or on a larger spacecraft where adequate power is available.) MIROS retroreflectors can be light-weight, rugged, radiation-resistant, and long lived. These properties allow the MIROS concept to be considered for a number of applications that may prove to be of value for space applications; the following are examples.

An earth-orbiting MIROS may be useful as a communication satellite. In this application, lasers located at two widely separated ground stations would be pointed simultaneously at the satellite. Modulation applied to the beam at one ground station (the transmitter) would be detected on the satellite by an optical receiver. The detected signal would be applied to the MIROS retroreflector, causing its reflective properties to vary as a function of the modulating signal. The retroreflected radiation from the second incident beam would thus be modulated. By detecting this modulation at the second ground station (the receiver), information would be transferred from one ground station to the other.

A lunar-orbiting MIROS could be used similarly as a communications satellite for providing over-the-horizon communications between moon-based teams.

A MIROS package carried by a small excursion module or by an individual astronaut may be used to communicate with a larger space station. The small size and weight, low power consumption, and ease of pointing the MIROS package would make its use advantageous aboard a small module or by an individual; the tracking laser required for effecting the communication link would be provided in the larger vehicle.

SID 65-1026

A MIROS package planted on the moon could be used for telemetering information from scientific measurements. For this application, measurements (e. g. , temperature, pressure, seismic phenomena, and meteoric impacts) might be obtained with no electrical power required at the telemeter transmitter. This could be accomplished, for example, by mechanically coupling the sensing transducer directly to the MIROS modulator element.

Several approaches are possible for implementing the retromodulator. One approach, currently under investigation at NASA, Goddard Space Flight Center, is the use of telescope optics with a suitably curved mirror at the focal plane (this constitutes a retrodirective optical system). The telescope optics can be made into a retromodulator by incorporating a means to modulate the retrodirected light at the curved mirror surface, either through the use of interference phenomena (e. g. , by means of a Fabry-Perot interferometer incorporating piezoelectric modulating elements) or simply by defocusing the retrodirected light by mechanical movement of the mirror surface. Another approach studied at North American Aviation (NAA) is to incorporate a means of modulation into an optical corner reflector.

The latter approach, i. e. , modulatable corner reflector having 100-square-centimeter effective area, can be obtained by providing a single corner cube reflector with 33 modulators[1] or an array of three corner reflectors each with 13 modulators. Each corner reflector is constructed of three separate quartz plates bonded together by optical contacting. Two of the inside surfaces of the corner reflector are made reflective by applying an aluminum coating; the modulator elements are located on the third surface of the corner reflector.

The actual accomplishments achieved under the NAA Phase I effort are related to the discovery, definition, and partial investigation of two critical factors: (1) membrane materials problems that tended to limit the bandwidth and reflectivity of the MIROS modulator models that were fabricated and tested and (2) a "breakthrough" in modulator design that allows achievement of greatly increased bandwidth of the device.

During the Phase I program, Mylar membranes were investigated quite thoroughly. Unfortunately, Mylar is processed by rolling and the surface roughness produced low reflectivity and considerable scattered light and increased beamwidth. It was proposed that other possible materials, such as rolled sheet metals or alloys, be investigated in a

---

[1]The term "button" has been used previously to refer to both the modulator subassembly and the disc which is a component of the modulator subassembly. To clarify the situation in this report, the terms "modulator subassembly" and "disc" have been used; however, some of the older terminology ("button") has been carried over and is used in various illustrations.

Phase II program. In the course of the experimental investigation a "breakthrough" with respect to bandwidth was achieved. It was discovered that a significant increase in the first resonant frequency of the membrane could be obtained by operating the modulators under slight pressurization rather than in vacuum as had been planned. It was requested that a theoretical and experimental analysis be made on pressurization during the continuing study in Phase II.

Since there were two possible techniques for implementing the MIROS concept, a comparative analysis of the deformable film versus the piezoelectric modulator was also performed in the Phase II program.

SID 65-1026

CONTRACT GOALS

Exhibit A of the subject contract defines the goals of Phase II of the MIROS Program as follows:

1. Investigate appropriate membrane materials and fabrication techniques. The objective of this effort is to improve the MIROS retromodulator beamwidth and reflectivity by attaining membranes having adequate flatness and surface quality characteristics. Consider applicability of pellicles and metallic membranes.

2. Continue development and test of modulator units (membrane modulator, including analysis) to secure the desired characteristics (i. e., ±10 second beamwidth, 50-percent depth of modulation, 20-kcps bandwidth, improved reflectivity). Perform theoretical and experimental analysis of effects of pressurization.

3. Perform comparative analysis of the following options in the design of MIROS:

   a. Use of deformable film versus piezoelectric modulators

   b. Variation of the beam intensity by use of an interferometer to change a surface's reflectivity versus deformation of a surface's geometry in order to vary the beam spread

   c. Cube corner configuration versus a spherical reflector-corrector configuration

4. Complete the design of the MIROS retromodulator and the final design of the remainder of the MIROS package

5. Construct one MIROS corner reflector without modulator units for evaluation during Phase II. Test and evaluate the optical and mechanical properties of the unit and deliver to NASA.

SID 65-1026

TECHNICAL PROGRAM

MODULATOR SUBASSEMBLY EXPERIMENTAL DEVELOPMENT

In the final configuration, the retromodulator portion of the MIROS package will consist basically of a corner reflector, one surface of which will serve as a mounting plane for an array of modulator subassemblies (Figure 1). This section presents a discussion of the program activities and results related to the modulator subassemblies; the corner reflector will be the subject of the following section.

With the selected fabrication approach, complete modulator subassemblies may be individually evaluated before final assembly of the MIROS package. Thus, a subassembly that is below performance standards can be rejected before final assembly and the possibility of damage to the corner reflector in removing a substandard or defective modulator unit is reduced.

Fabrication Accuracy

The components of the modulator subassemblies must be made to extreme accuracy since the array of modulating membrane surfaces must have a very minimum of angular-tilt between the various surfaces and all must be coplanar within a fraction of a wavelength of light. If the required tolerances are not maintained, the spread of the beam reflected from the array will be increased and out-of-phase conditions will be introduced. To maintain the required tolerance control, all of the subassembly components were manufactured by the optical shop of the Electro-Optical Laboratory (EOL) rather than subcontracted to a vendor.

Based on the conservative assumption that the errors in all of the components will add in the most deleterious manner (i. e., there will be no compensation or cancelling), it follows that every effort should be made to ensure the highest precision for all component fabrication. The total permissible error must be rationally allocated between the corner reflector, the modulator subassemblies, and the pressure window located in front of the retrodirector. The pressure window is a refractive element and, if reasonable manufacturing specifications are adhered to, surface variations from perfect flatness will have very little affect on beam spread. The wedge angle, providing it is constant across the window, will have no affect whatsoever on beam spread since the light
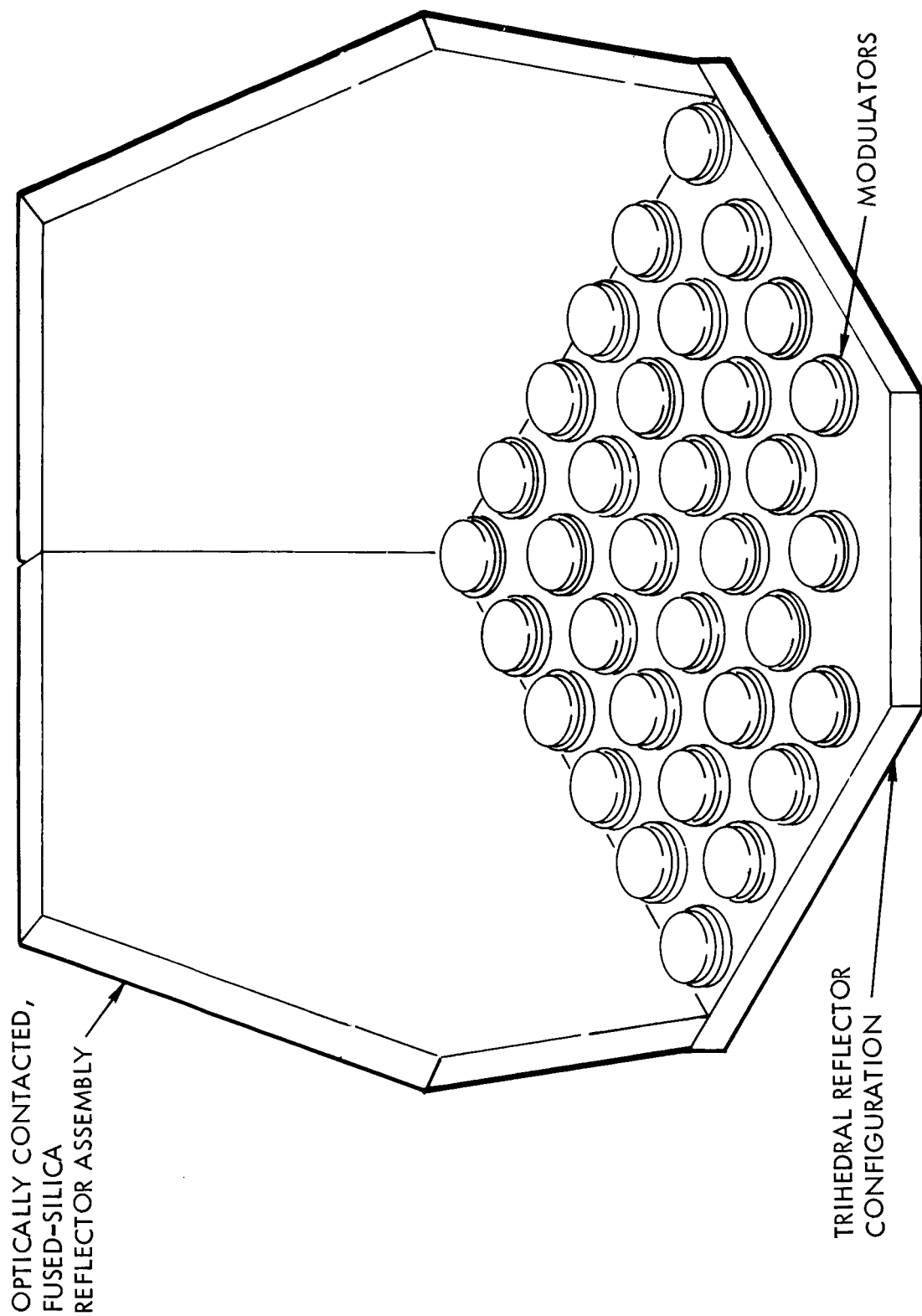
SID 65-1026

Figure 1. Corner Cube Reflector

MODULATORS

OPTICALLY CONTACTED, FUSED-SILICA REFLECTOR ASSEMBLY

TRIHEDRAL REFLECTOR CONFIGURATION

beam traverses the window in opposite compensating directions. Thus, the corner reflector and the modulator subassemblies are the major contributors to an undesirable increase in the spread of the retrodirected light beam. The tolerance on the 90-degree angles of the corner reflector has been set at 1 arc-second. Since possible errors will be located 120 degrees from each other in the aperture plane, they will not be fully additive. Therefore, the specific error for the entire reflector will be less than 3 arc-seconds.

The utmost care must be exercised in the production of the modulator subassemblies, since a 2- or 3-micron particle of dirt caught between the membrane and the mounting ring will cause a local membrane variation of several wavelengths of light. If a total contribution of 1 arc-second to the beam spread is allowed for out-of-parallelism of the modulator surfaces, then a maximum error contribution of 0.5 arc-seconds per modulator subassembly is permissible. This corresponds to a thickness variation of 500 Angstroms across the diameter of any one modulator subassembly.

The accuracy obtained in the production of components for the modulator subassemblies is demonstrated in Figure 2. The circular elements shown in the photograph are fused silica discs used as components in the modulator subassemblies. As will be evident later in discussions of fabrication techniques, the accuracy with which these discs are made is representative of the accuracy for other components. In the figure, a disc was contacted to a 4-inch-diameter test glass, which permitted transmission through the disc and the test glass to the black paper on which the assembly was resting. Thus, this disc is darker in appearance than the others and identifies the starting or reference point for the following assembly. Two discs were contacted side by side to the top of the reference disc, and subsequent contacting of two more pairs of discs produced a double staircase-type assembly as illustrated. Finally, a single disc was contacted to the top pair of step assemblies. A uniformity of height in the two step-assemblies of approximately 1/10 wavelengths of light or 2.4 microinches were necessary to allow contacting of this final disc. Since possible errors were divided between three discs, the error in both thickness and nonparallelism per disc was less than one microinch or about 250 Angstroms. This is representative of the production accuracies for such discs, and indicates that the permissible thickness variation of 500 Angstroms from one side of a modulator surface to the other can be easily maintained.

TORR-833-209A
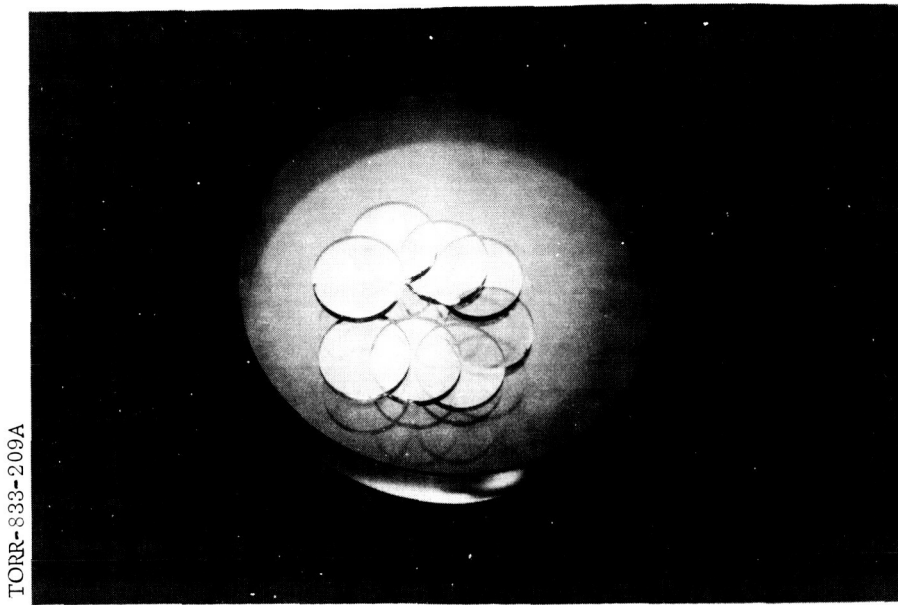
Figure 2. Double Staircase of Optically Contacted
MIROS Modulators

Fabrication Techniques

Basic Components

The modulator subassembly construction is shown in Figures 3
and 4. The assembly consists of a base plate, a disc, a support ring,
the membrane, and some method of electrical connection such as gold
lead wires or a conducting surface film. The membrane material is
mounted on the top edge of the support ring with a one thousandths of
an inch (one-mil) gap between the membrane and the top surface of the
disc. The accuracy and uniformity of this one-mil gap determines the
quality of performance of the completed modulators.

The base plate is made of optical-quality fused silica approximately
one inch in diameter and 0.1 inch thick. Since both sides of this plate
must be placed in optical contact[2] with other elements, they are polished
flat to approximately 1/10 wavelength of visible light. This is done by
first grinding and polishing one side of each base to the desired flatness
and then mounting the entire set of bases in optical contact on a pyrex
plate to finish the opposite sides of all the bases in a single operation.

---

[2]Optical contacting is discussed hereinafter.

SID 65-1026

METAL MEMBRANE

PYREX RING

FUSED SILICA
MODULATOR BUTTON

FUSED SILICA
MODULATOR BASE
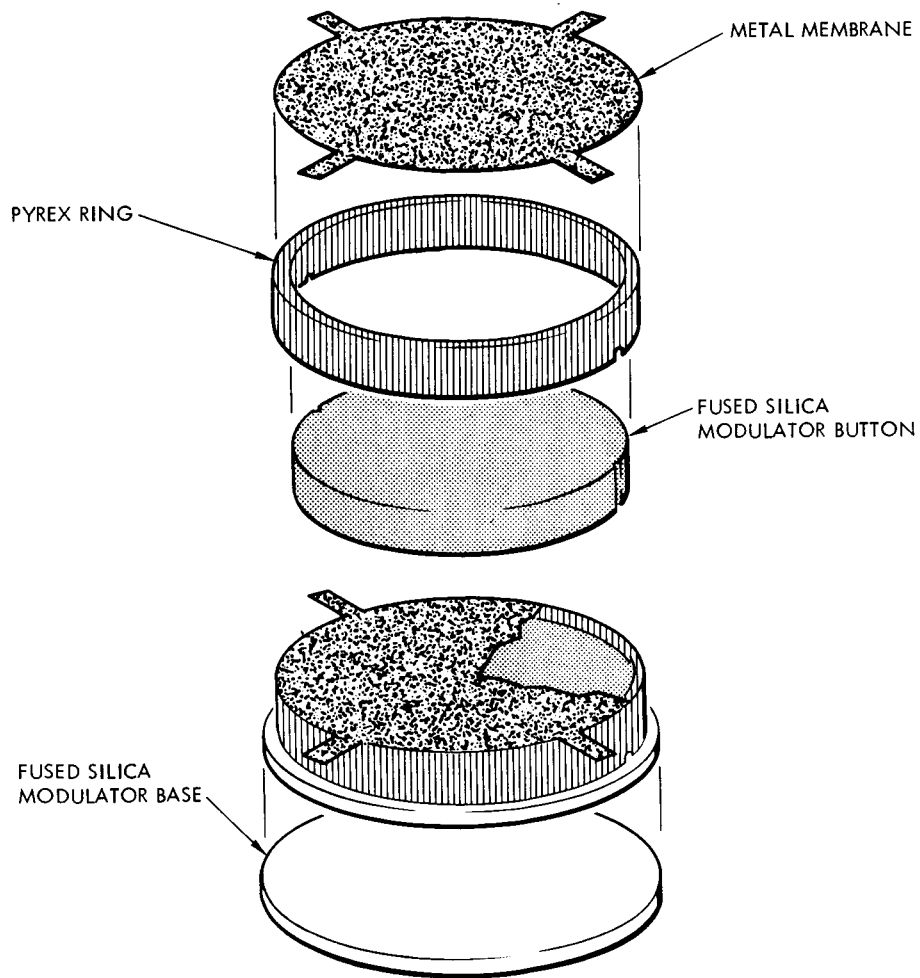
Figure 3.   Breakaway View of a Modulator Subassembly

EVAPORATED GOLD SURFACE

ACTUAL CONTACT
OF GOLD & SILVER

TAB

GOLD WIRE

DISC & RING GROOVE
FILLED WITH SILVER PAINT

0.001-INCH GAP

0.0001-INCH
METAL
MEMBRANE

PYREX RING

FUSED SILICA
MODULATOR DISC

FUSED SILICA MODULATOR BASE

Figure 4.   Cutaway View of a Modulator Subassembly

- 12 -

All bases made in this manner will have identical thicknesses. Consequently, all the membranes in the final assembly will be located in a single plane.

The modulator disc and the support ring are fabricated together as a concentric set to insure proper fit and dimensional integrity. The support ring is made from precision-bore pyrex tubing that has an internal diameter accurate to a few tenths of a mil. The discs are produced from optical-quality, fused silica bar stock. The fused silica bars are centerless ground with a final diameter just small enough to provide a snug, sliding fit into the precision bore tubing.

Two narrow slots, approximately 0.020 inches wide and deep, are cut on opposite sides of the bar, parallel to the cylindrical axis. These slots serve as breathing tubes in the final assembly and as grooves for the elec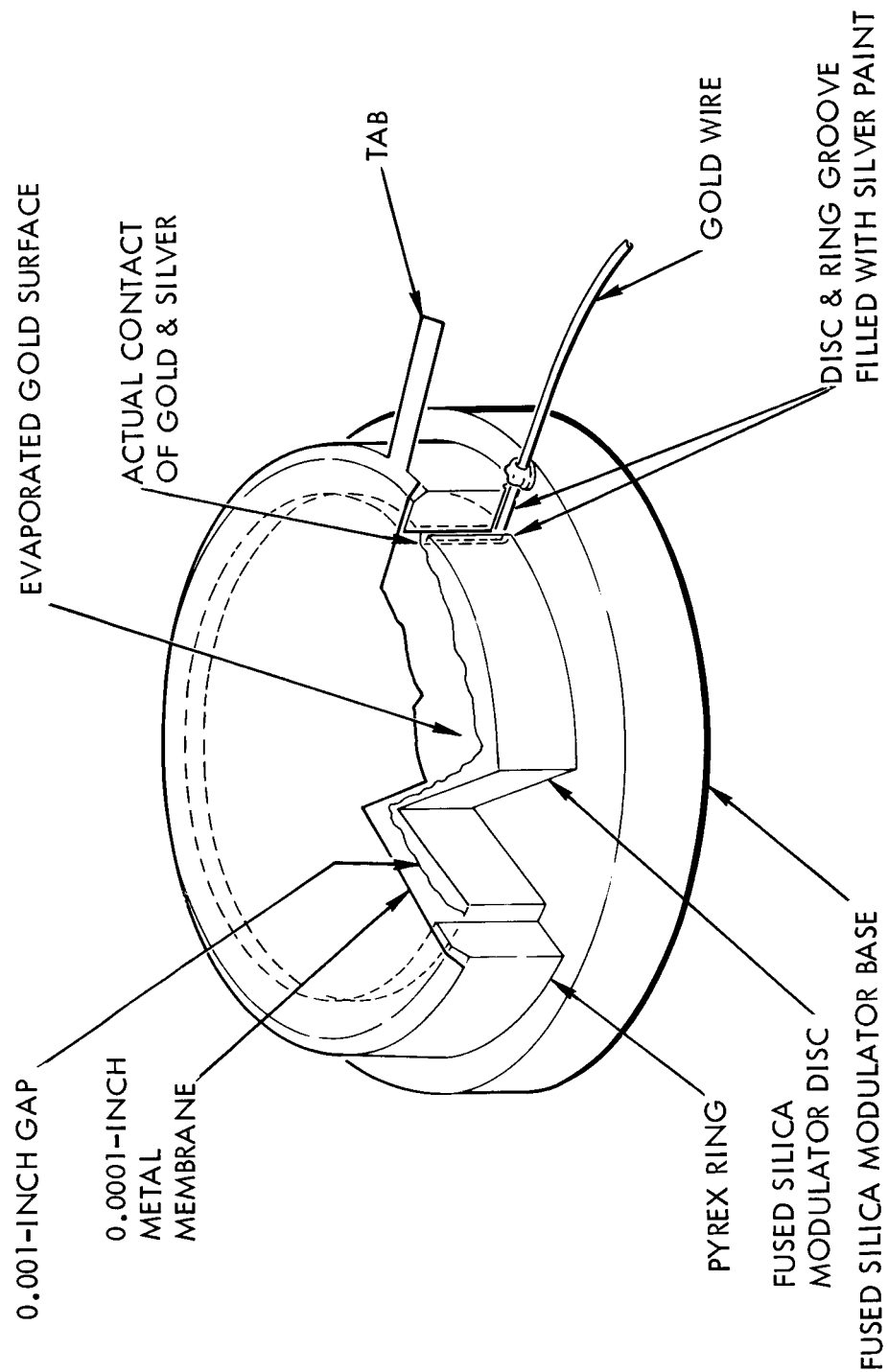trical connections to the inner capacitor surface if necessary.[3] These grooves are acid polished to relieve any processing stresses and to prevent any subsequent chipping or cracking in later operations.

The precision-bore tubing is temporarily cemented with beeswax to the fused silica-bar stock for processing. To provide protection for the bar-tubing combination, it is cemented inside a larger section of glass tubing. A thin diamond saw blade is used to make transverse saw cuts approximately 3/16 of an inch apart through the bar-and-double-tubing combination. This operation produces rough disc-and-ring combinations, each with an additional protective ring. These units are hand ground to a reasonably smooth and flat surface to facilitate subsequent blocking. After removal of the outer protective ring, the disc-and-ring combinations are blocked for finishing of the first side. This side is ground and polished flat to 1/10 of a wavelength of visible light by standard techniques.

The disc-and-ring combinations are then removed from the block, cleaned, and contacted (polished side down) to an optical flat, the surfaces of which have been previously polished to better than 1/10 of a wavelength flatness and parallel to within 0.25 arc seconds. (Figure 5 shows 27 fused-silica discs with support rings contacted to the optical flat.)

By grinding and polishing the second surface of all the units simultaneously, identical thickness and parallelism within the tolerances allowed will be attained. This second surface is also polished to a 1/10 of a wavelength flatness.

---

[3] An alternative electrical connection, a conducting surface film, is discussed elsewhere in this report.

An interferometer can be used to measure the parallelism of two surfaces by viewing the interference fringes formed between them. This technique can be used to measure and control the parallelism between the top surface of a disc and the bottom surface of the optical flat to which the disc is contacted. When these surfaces are made parallel, the two surfaces of the disc will be parallel within 0.25 arc-seconds since that is the accuracy of the parallelism of the optical flat and no additional significant error is introduced in the contacting process. After the second side is finished to the requisite accuracy, the rings are removed (see Figure 6) and polishing is continued until the thickness of the discs themselves is reduced by 0.001 (+0.0000 or -0.0001) inches. Control at this point is of the greatest importance.

As indicated in Figure 4, the top surface of the support ring is beveled on the outer edge. This provides a surface for the epoxy cement that holds the membrane to the ring. This bevel is produced by very fine grinding of the ring in an appropriate concave grinding tool. A small groove is also cut on the opposite edge to match the grooves on the sides of the disc.

After removal of the discs from the plate, each is placed on its base plate in optical contact and thus held firmly without cementing. The top surface of the disc is coated with aluminum so that it may serve as the bottom plate of the modulating capacitor. A one-mil gold-wire lead, laid in the groove in the side of the disc, is cemented to the aluminum coating with conductive epoxy. An alternate technique used for electrical connection utilized a conductive transparent coating of stannic oxy-chloride to cover all surfaces (see section on Conductive Coatings). This technique obviates the necessity of the gold-wire leads and aluminum coating of the buttons. With the transparent coating, no electrical connections need to be made to the base until final assembly in the corner reflector is completed.

After the discs and base plates are assembled, the support ring is mounted in place. The grooves in the side of the modulator button are then matched with the corresponding notches in the bottom surface or edge of the support ring. Also, the gold wire, if used, is located in the notch of the support ring.

The contacting edge of the support ring is only 1 millimeter wide. Since the ring is pyrex and the base is fused silica, optical contacting between the two dissimilar glasses is not as strong as would be required. Production models should have a fused-silica ring so that the entire assembly will be effectively one piece of fused silica. Fused silica was not used for the support ring during Phase II of the program because of the difficulty encountered in obtaining fused-silica tubing of the required precision inner diameter; for larger volume production, however, a process of selection should produce the required diameter and tolerance.

- 14 -

SID 65-1026
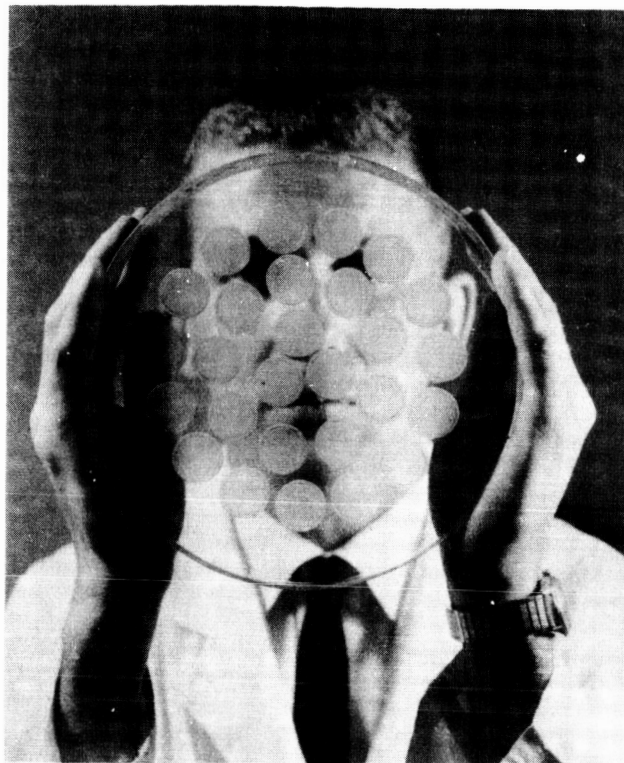
Figure 5. Optically Contacted MIROS
Modulators With Support Rings
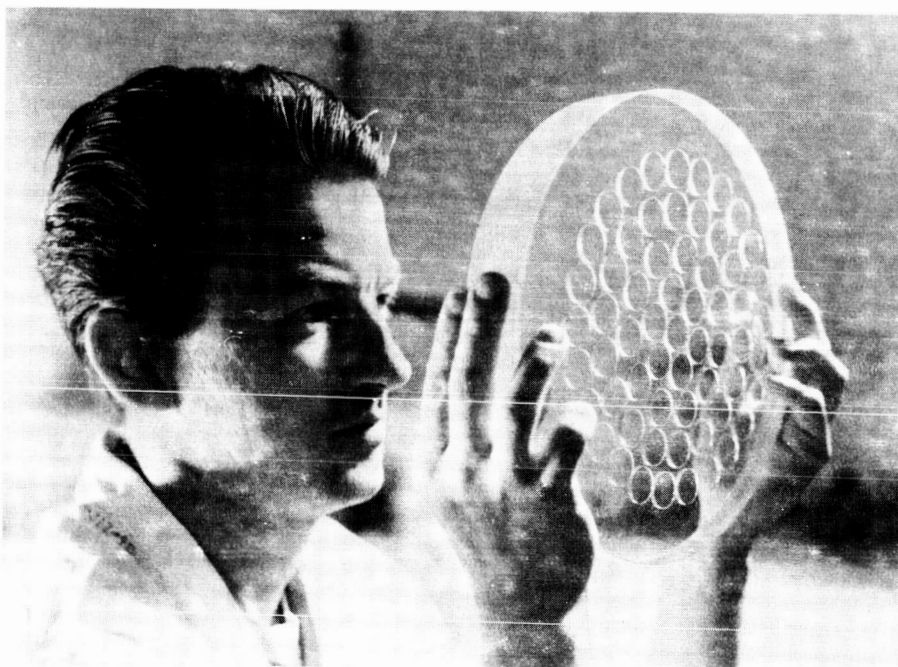
Figure 6. Optically Contacted MIROS Modulator Centers

- 15 -

After the support ring is placed in optical contact with the base plate, a small fillet of epoxy cement is placed along the join edge between the two parts. Care must be used to prevent accidental sealing of the two breathing holes that are used to equalize the pressure on the two sides of the membrane.

At this point, the assembly is ready to have the appropriate membrane mounted in place on the support ring. Assembly of the discs and support rings and the positioning of the membrane material produces a 0.001-inch gap between the membrane and the top surface of the disc. Figure 7 shows the completed assembly. The fused-silica base plate is made in the smallest diameter possible to prevent a decrease in efficiency of the final retromodulator assembly. The base plate shown in Figure 7, however, is slightly oversize.

Membranes

Techniques used for attaching the metallic membranes to the support rings will now be discussed. The complete fabrication of Mylar modulators (vacuum coating, etc.) was discussed in the MIROS Phase I
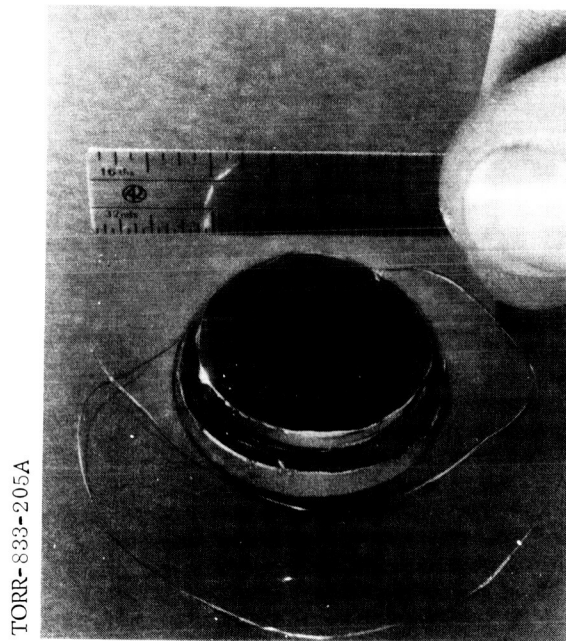
Figure 7. MIROS Modulator Subassembly

Report, and the pellicle modulators were purchased from an outside vendor; therefore, discussion of these materials will not be included here.

Extreme care must be exercised in selecting a piece of membrane material to insure that it has no lines or streaks through it and very little, if any, other deformations that may decrease reflectivity or cause the membrane to rupture while the material is under tension. After a good piece of material is selected, it is placed with care on the bottom half of the preliminary stretching jig fixture. Then the top half of the fixture is placed over the material and the peripheral screws are tightened. Uniform tightening of the screws is necessary to prevent excessive strain or deformities in the membrane.

The metal membranes are cleaned with acetone then immediately rinsed with distilled water, air dried, and finally dried by rubbing very gently with a polishing cloth. This method of cleaning increases reflectivity by eliminating oils and most minute particles that may have adhered to the material.

The assembled modulator unit is mounted on an assembling fixture and cleaned with various organic liquids, a polishing cloth, and an electrostatic brush. Extreme care must be exercised during the cleaning process. A microscope with a 10 x eyepiece and a 0.5 x objective or better is recommended. Since the air gap between the membrane and the button is 0.001 inches, particles large enough to rupture the membrane are difficult to see with the naked eye. A very thin film of acetone may be used to remove surface oils, but caution must be exercised so that the volatile liquid does not cause a loss of optical contact.

The fixture containing the membrane is placed over the modulator assembly and brought accurately into position so that the tension produced in the membrane is uniform. The modulator assembly (Figure 8) is elevated in small increments until the proper angle is established between the membrane and the slightly beveled edge of the support ring. The existence of any particles beyond 0.001 inches diameter in the air gap can be detected by slightly increasing the tension of the membrane. If such particles exist, they must be removed when the membrane fixture is lifted for application of the epoxy along the beveled edge. Removal of the membrane fixture may be required several times until visual inspection indicates that the surfaces are clean. The modulator assembly must remain at the same height through the entire cleaning process. Removing and replacing the fixture on the modulator assembly several times will not rupture the membrane if it is handled gently and the assembly is not readjusted.

SID 65-1026

After the modulator assembly is thoroughly cleaned and the membrane fixture is removed, the elevation of the modulator assembly is decreased so that epoxy can be applied to the outside beveled edge of the support ring. The membrane fixture is then replaced and the elevation of the modulator assembly is increased until the proper angle is again established between the membrane and the slightly beveled edge of the support ring. The angle of the bevel is used to control the membrane tension during fabrication. The completed jig fixture assembly is placed into an oven for 1-1/2 hours at 150 F to cure the epoxy. (Twenty-four hours are allowed for curing at room temperature.) The fixture assembly is then removed from the oven and allowed to cool for 2 hours at room temperature.

To remove the modulator assembly from the membrane fixture, the peripheral screws are loosened, relaxing the membrane as shown in Figure 9. The membrane material surrounding the modulator assembly is then carefully removed with a sharp knife, Figure 10. The completed modulator assembly is now ready for testing and the necessary electrical connections.

Conductive-Coatings

Since the upper surface of the fused-silica disc serves as one plate of a driving capacitor, this surface must be electrically conductive. Evaporated aluminum was used as the conductive coating on the first modulators assembled and tested. Several modulators with the aluminum conductive coating failed, usually from internal shorts, after varying periods of use. Careful inspection revealed small specks or areas of aluminum that had flaked off and shorted across the 0.001-inch gap. It was determined that the flaking was a result of premature evaporation of the aluminum before all outgassing had ceased and an adequate vacuum (10^{-5} Torr) had been obtained. By the establishment of new and improved evaporation procedures, it became possible to produce coatings of aluminum that were successful in subsequent tests.

Instead of aluminum deposition, there exists the possibility of coating the entire modulator disc with a conductive, transparent coating, as mentioned earlier. Prior to World War II, electrically conductive coatings of stannic oxy-chloride were produced on glass surfaces by an evaporative technique. For many years the electrical conductivity and strong adherence were properties of interest, while uniformity of thickness and transparency were not important. The Libbey-Owens-Ford Company in Pennsylvania has continued the development of this coating and alternate techniques for its production.
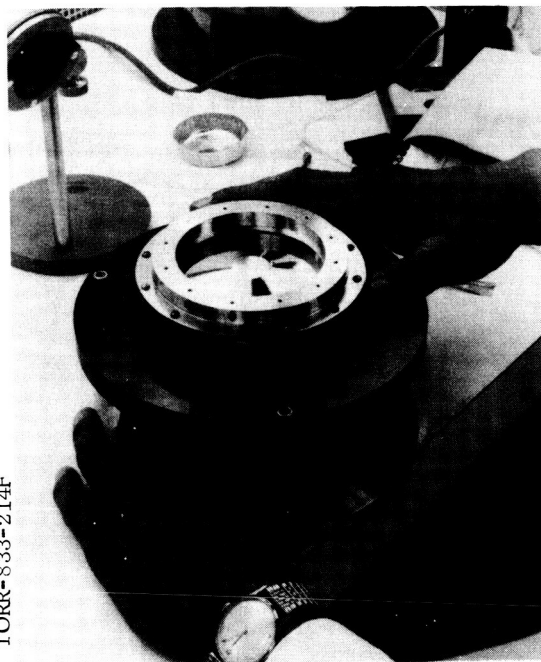
- 18 -

TORR-833-214F

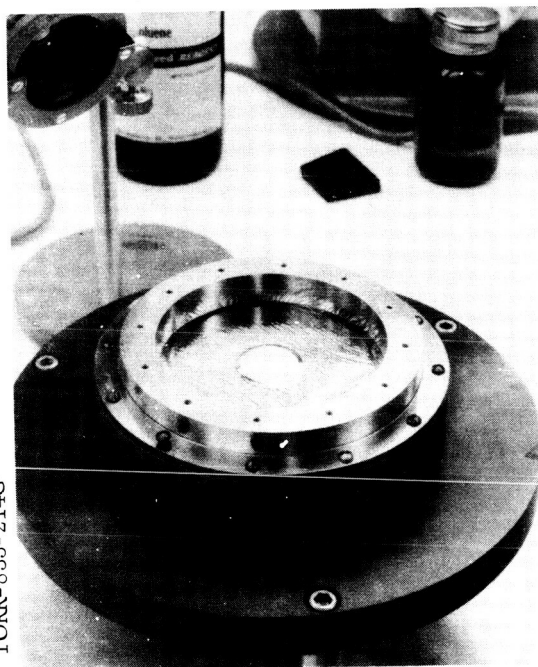Figure 8. Tensioning of
Membrane Material

TORR-833-214G
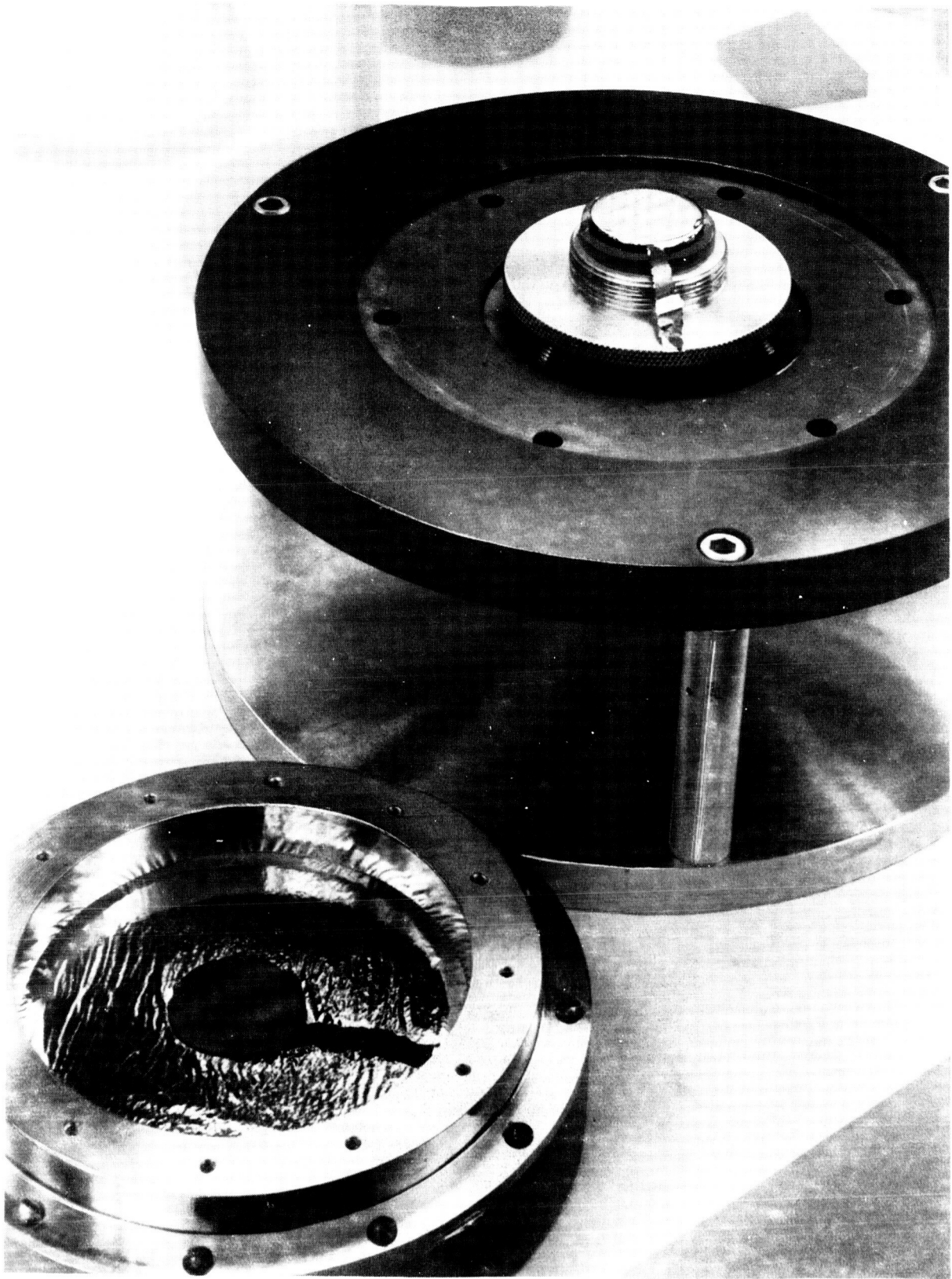
Figure 9. Membrane Relaxation
After Epoxy Has Set

- 19 -

Figure 10. MIROS Subassembly Removed from Assembly Fixture

TORR-833-214A

The electrically conductive coatings now have very satisfactory optical properties. They have an optical transmission of about 80 percent at the wavelength of interest and are quite uniform in thickness. Their adherence is demonstrated by their resistance to scrubbing and cleaning prior to optical contacting. The optical contacting itself attests to the uniformity, for it would be impossible if the thickness was not uniform within at least a few hundred Angstroms. Of four companies investigated, it appears that Libbey-Owens-Ford is the only company that has produced completely satisfactory coatings.

For ease of assembly and inspection, a continuous transparent coating on all surfaces of the disc, the base plate, and the mounting surface of the corner reflector will improve the design, the mechanical construction, and overall appearance of the modulating units. The transparent coating will also permit inspection of the interior of the completed modulator to determine the location and type of any defect if present. In addition, the continuous coating will prevent the possibility of open circuits.

Optical Contacting

When two extremely flat, transparent glass surfaces are placed together, interference fringes (light and dark lines) are observed. The shape of the fringes indicates the congruency of the surfaces, while the separation of the fringes indicates the degree of parallelism of the two surfaces (increased spacing indicates greater parallelism). The color of the bright fringes (assuming a white source is used for observation) indicates the separation of the surfaces. If two sufficiently flat and clean surfaces are placed together and pressure is applied, the pieces can be made parallel enough that the interface appears as a solid color. As more pressure[4] is applied, the surfaces will be forced closer together and the color will change towards shorter wavelengths to indicate this. When the spacing becomes less than one-half the wavelength of blue light, or about 2000 Angstroms, no color will be seen and the surface area will become completely transparent. When this condition occurs, the two pieces are said to be in optical contact. The surface separation is less than 2000 Angstroms and probably around 100 to 200 Angstroms, which represents the approximate thickness of the residual film of air adsorbed on the two separated surfaces before optical contacting. The significance of this condition is that the two pieces actually become one and, in time, lose memory of the separation. The bond is as strong as the glass itself. This method has been chosen for bonding the components of the MIROS assembly for two reasons: it is

----

4
Born and Wolf. Principles of Optics. Second Revision. New York: Macmillan (1964), p 398, eq 18 and Figure 8-13.

a very strong bond and is the only one that will allow the precision necessary. Any epoxy or cement bonding would degrade the angular precision.

Evaluation

The modulator membrane, being the "active element," is probably the most important single component of the MIROS system. The properties of this membrane largely determine the maximum intensity of the retroreflected radiation, the depth of modulation, the signal distortion, and the driving voltage and power requirements.

The aim of the evaluation portion of the program was to determine if certain modulator-improvement goals and performance requirements listed under Contract Goals could be attained. The objective was to "improve the retromodulator beamwidth and reflectivity by attaining membranes having adequate flatness and surface quality characteristics." The performance goals are a "50-percent depth of modulation and a 20 kcps bandwidth."

Membrane Materials

The desired optical properties of the membrane are strongly dependent upon how it is fabricated, how it is attached to the modulator subassembly, and the properties of the material itself. Commercially available rolled membranes were tested during Phase II of MIROS. They were found to have a coarse surface structure that affected the degree of overall specular reflection. Slight improvement was attained by polishing or by deposition of an aluminum coating. It has been discovered recently, however, that membranes formed by vacuum deposition techniques (referred to as replicated membranes) had about ten times the specular reflectivity of rolled membranes. Consideration of these came too late to permit inclusion of membrane response tests in Phase II of MIROS. However, some optical tests were performed on them in the presence of the NASA Project Engineer during the week of September 20, 1965. The optical tests have demonstrated so clearly the superiority of these replicated membranes that future efforts should be directed towards the fabrication and evaluation of them.

The performance goals are 50 percent depths of modulation and 20 kcps bandwidth. Unfortunately, distortion becomes worse with increases in either of these. Consequently, a compromise in terms of modulation depth and bandwidth is imposed by distortion limitations. Bandwidth is limited by the fundamental resonant frequency, which can be increased (see Appendix I, equation 14A) by increasing the ratio of membrane tension to density of the material.

The membrane materials selected for testing were Pellicle, Mylar, Havar, Stainless Steel and Titanium. The last three were selected on the basis of their high resonant frequency potential. Table 1 indicates the predicted highest attainable vacuum resonant frequencies which were calculated on the basis of yield strength data. The highest frequency achieved in practice was 12.7 kcps with Havar. It has been found, both theoretically and experimentally, that resonant frequency can be increased by the presence of gas on both sides of the membrane. While this pressurization is capable of extending the resonant frequencies to 20 kcps for some membrane materials, undesirable distortion effects occur. Therefore, it is desirable to have a membrane with as high a vacuum resonant frequency as possible to reduce pressurization requirements.

Table 1. Properties of Membrane Materials

Material	Specific Gravity	Yield Strength (lb/in.^{2})	Calculated Maximum Vacuum Resonant Frequency (kcps) (Diameter 2 cm — equation 14A Appendix I)
Mylar	1.3	12,000	9.6
Stainless Steel	7.9	125,000	12.6
Titanium	4.3	65,000	12.3
Havar	8.1	270,000	18.3

Optical Test Setup

The setup described here was used in a series of measurements taken to determine the effect of applying a specified voltage signal to a modulator subassembly. These effects are measured in terms of a distant observation of a beam of laser radiation that is specularly reflected from the membrane surface. This distant observation is referred to as a "far-field" observation and is optically simulated in the laboratory by the equipment shown in Figure 11. The laser, which is Perkin-Elmer Model 5200, has a

- 23 -

3. 2-CM FOCAL LENGTH

GAS LASER

COLLIMATOR 122 CM
FOCAL LENGTH

15. 3-CM APERTURE

MEMBRANE

PHOTOMULTIPLIER
TUBE

25-MICRON
PINHOLE

FOCAL LENGTH 105. 4 CM

VYCOR
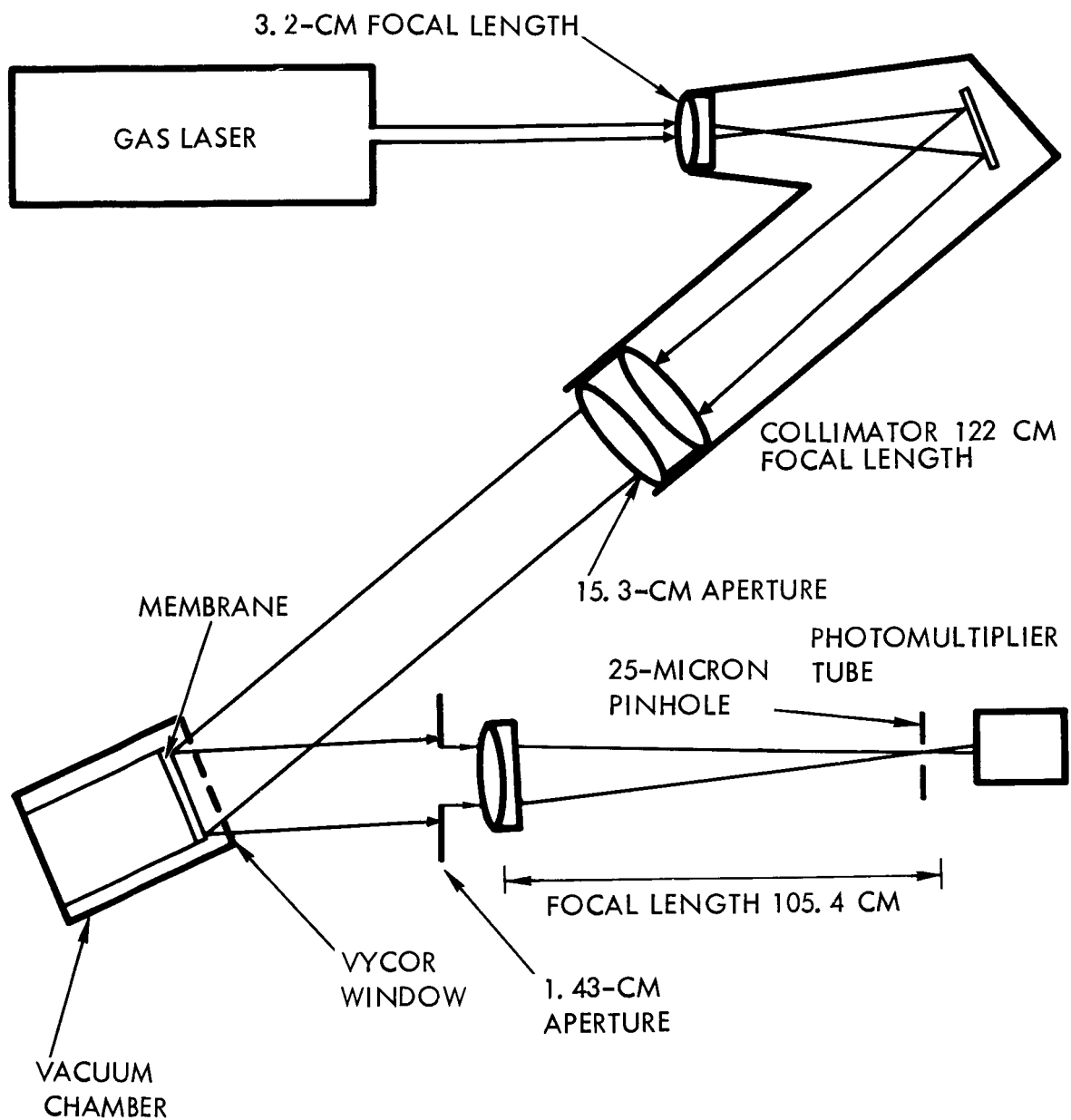WINDOW

1. 43-CM
APERTURE

VACUUM
CHAMBER

Figure 11. Optical Setup for Membrane Response Testing

0.5 milliwatt output at 6328 Angstroms. In the Perkin-Elmer Model CF 6-48 collimator, the beam is brought to a focus by the first lens, expanded, and then rendered parallel again on emerging from the second lens. The 0.2-cm laser beam diameter is expanded to approximately 7.6-cm. The collimated beam is then reflected from the surface of the membrane. The incident angle is approximately 10 degrees.

The modulator subassembly is mounted in a suitable pressurized cylindrical chamber (see Figure 12) with the surface of the membrane parallel to the cylinder ends. An optically flat Vycor window is sealed to one end of the cylindrical housing with Viton O-rings. The other end of the cylinder, which is also sealed with Viton O-rings, contains the vacuum line, electrical leads, and the modulator subassembly support. The chamber pressure can be varied from atmospheric down to approximately 150 microns of mercury by use of a Cenco-Pressovac 4 (1.3 cfm) mechanical vacuum pump. Vacuum measurements below 1 mm were made with a Cenco List No. 94178 thermocouple gage. Above 1 mm, measurements were made with a U tube manometer.

The radiation reflected from the membrane is passed through an aperture 1.43-cm in diameter and then focused by a 4-cm-diameter, 105-cm-focal-length, air-spaced achromat.[5] A pinhole, which is within 5 percent of a perfect 25-micron circle, is located at the center of the focused spot.

This optical test setup simulates an observation of radiant flux reflected from a single modulator subassembly located in space (reference Appendix II). If the modulator is at a distance of 100 miles, the pinhole corresponds to the total radiation enclosed in a circle that is 12.7 feet in diameter at the center of the reflected beam. An RCA 7265 fourteen-dynode photomultiplier tube (S-20 photocathode) is used to detect the flux passing through the pinhole.

This fundamental setup was used for tests that were performed to determine the dc transfer function, resonant frequency (vacuum and under pressure), driving voltage requirements, and signal distortion. The additional equipment required for each test is described in the report under the particular test.

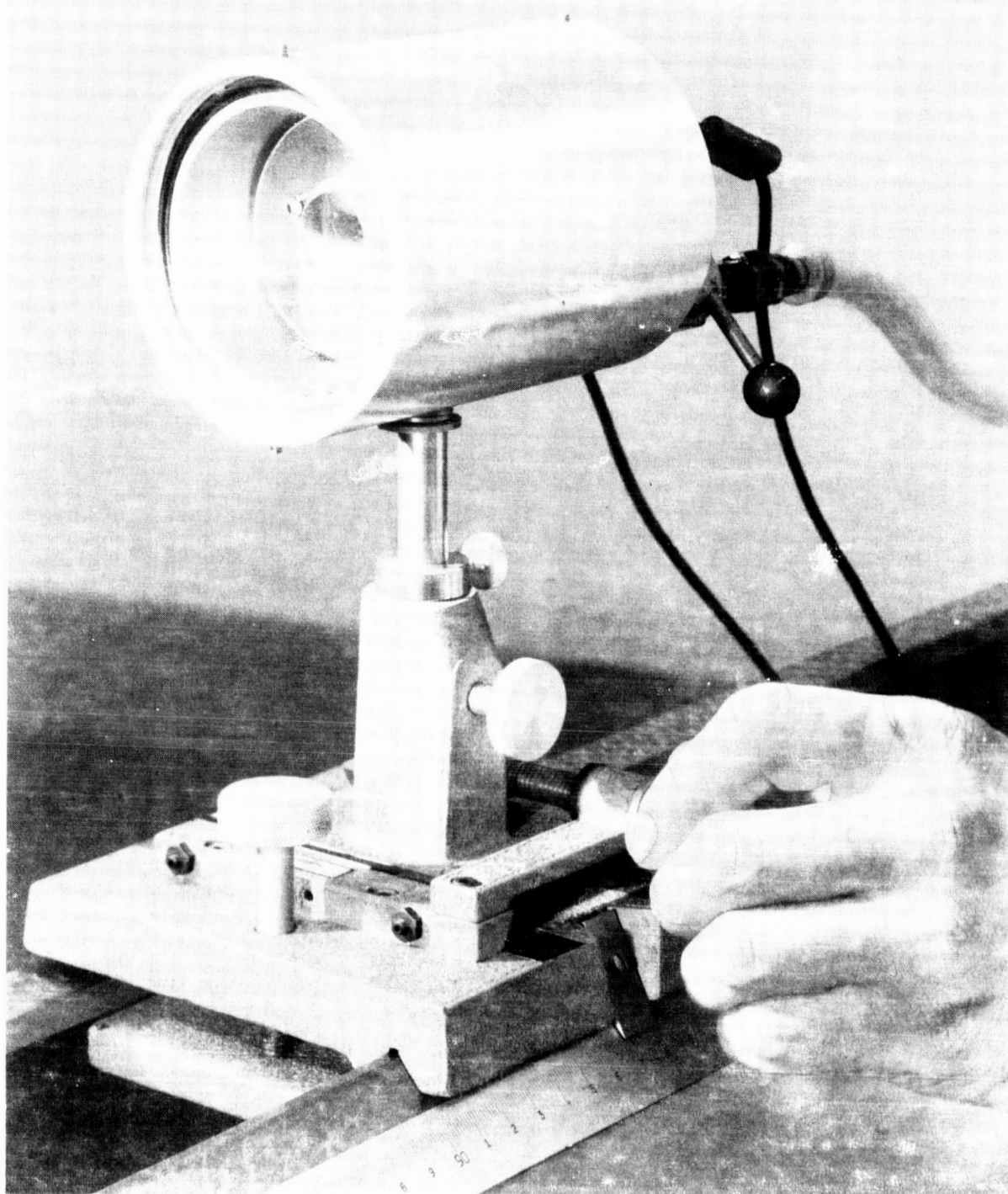[5]American Science Center Catalog No. 30202

Figure 12. Vacuum Test Chamber Containing Modulator Subassembly

DC Transfer-Function Measurements

The modulation dc transfer curve defines the relative light intensity under far-field conditions as a function of applied dc voltage.

Figure 13 presents a schematic drawing of the dc transfer test setup. The output of the PM tube is amplified by a Tektronix amplifier, Model 1121, and fed into a Moseley Model 2 DR-4, x-y recorder. A power supply is used to supply the dc voltage to bias the membrane. The magnitude of the voltage is monitored by the x-y plotter.

Examples of the dc transfer curves are shown in Figure 14, where the ordinate has been normalized to 100 percent for all materials tested. These curves were used to provide an initial assessment of the particular modulator. For example, by selecting a point at the center of the "linear" portion of the curve, the optimum bias point is determined. The curves also indicate the linearity and achievable depth of modulation (for low pressures) and were taken for complete subassemblies and are not representative of the membrane material alone. For example, they are a function of the total membrane tension, uniformity of membrane tension, internal stresses, optical characteristics of the membranes, and pinhole alignment.

Frequency Response Measurements

The frequency response measurements give the resonant frequency of the membrane as measured in the far-field as a function of pressure. A schematic of the test setup is shown in Figure 15. A Dressen Barnes Model D-50 regulated dc power supply is used to bias the membrane to the midpoint of the "linear" portion of the dc transfer curve. The wave analyzer is a Hewlett-Packard Model 302A that performs several operations. The driving voltage is supplied by a frequency-tunable oscillator in the wave analyzer, which is driven by a sweep-drive unit; the sweep-drive provides an electrical position signal for the x axis of the x-y recorder. The output of the photomultiplier is fed into a tunable receiver that is tracked to the tunable oscillator by the sweep-drive; the tunable receiver has a rectified signal output that is used to provide the y axis signal for the recorder. By linking the tunable oscillator to the tunable receiver, the output signal of the photomultiplier tube can be monitored at the same frequency as the driving frequency.

The resonant frequencies for the tested modulators at vacuum and at a pressure of 20 mm are indicated in Table 2, and the resonant frequency versus pressure curves of the modulators are shown in Figure 16. None of the materials, however, is capable of achieving a vacuum resonant frequency of 20 kcps.
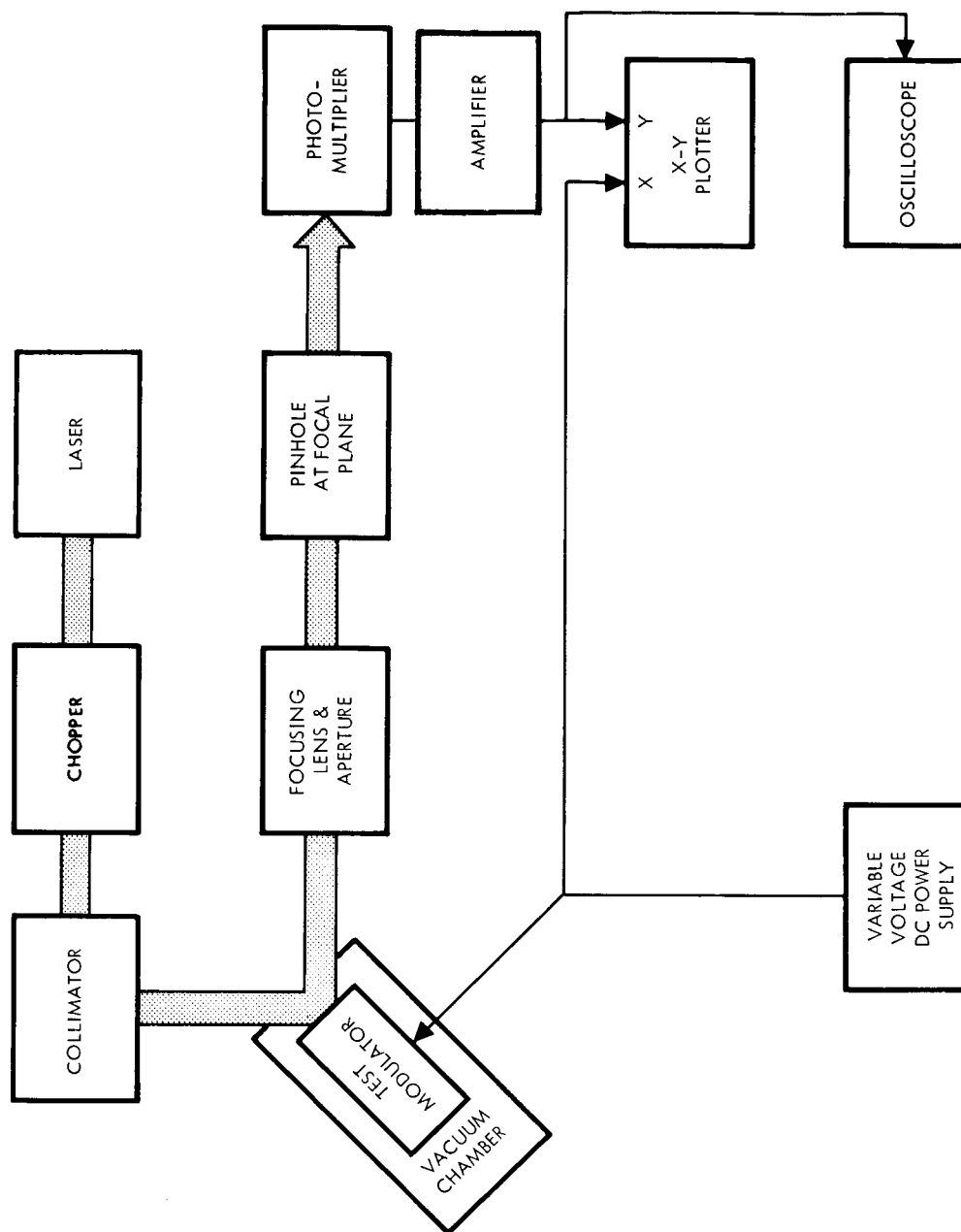
Figure 13. DC Transfer Test Setup
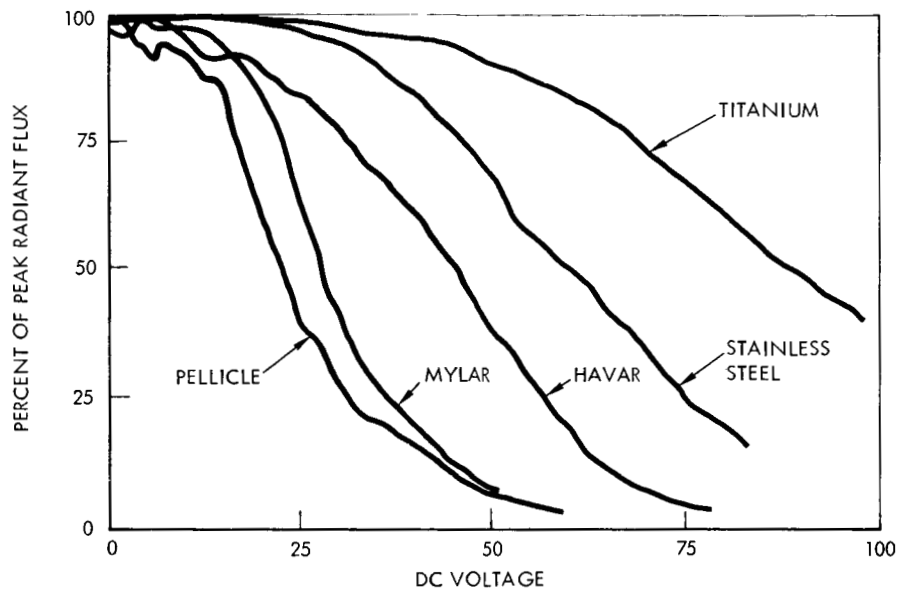
Figure 14. DC Transfer Function Test Results

Table 2. Achieved Resonant Frequency

Material	Vacuum Resonant Frequency (kcps)	Resonant Frequency at 20-mm Pressure (kcps)
Mylar	3.3	8.9
Pellicle	4.5	12.2
Stainless Steel	9.6	14.7
Titanium	10.8	17.1
Havar No. 2	12.7	17.8
Havar No. 3	10.7	16.0
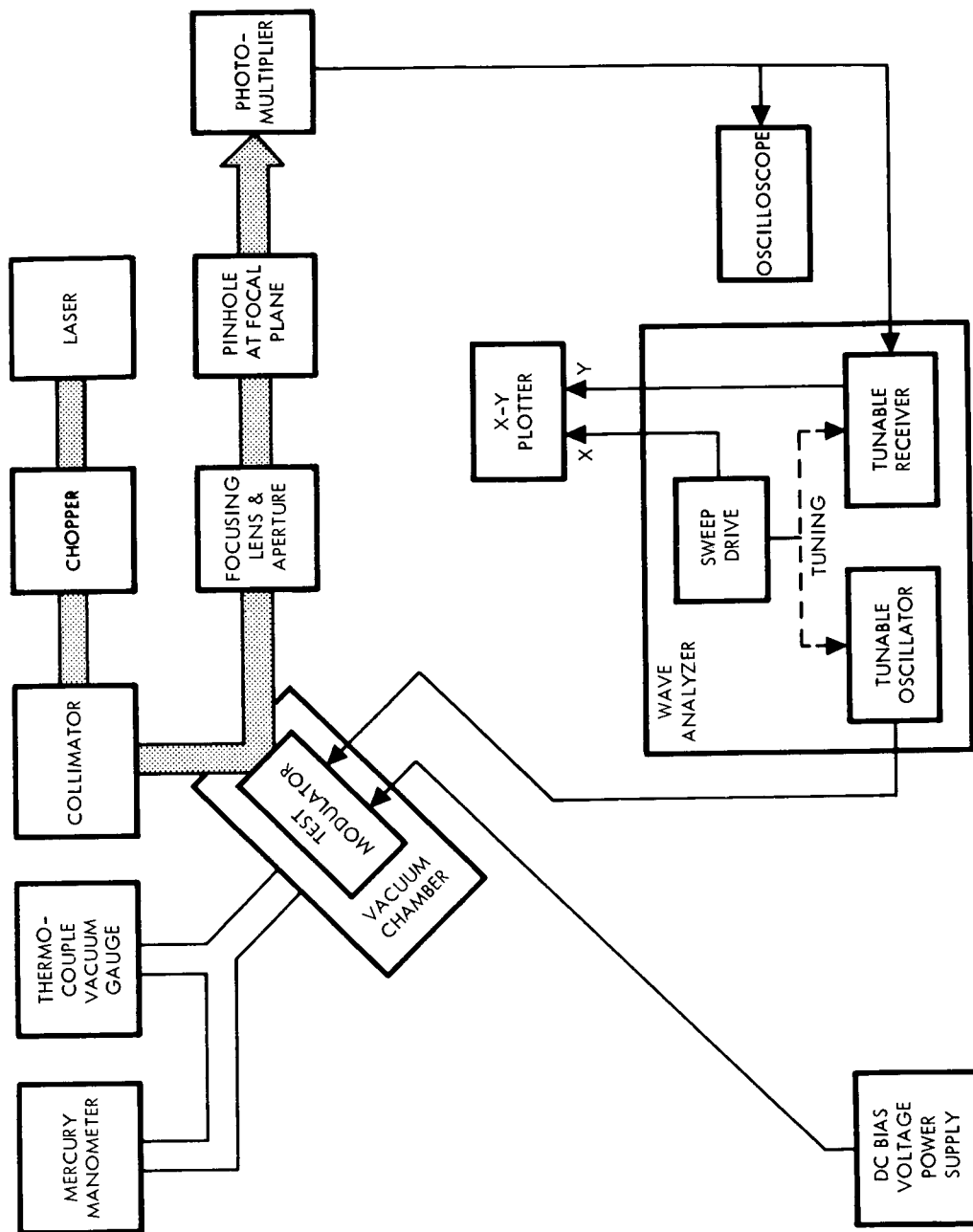
Figure 15. Frequency Response Test Setup

It was found that the shape of the experimental resonant frequency versus pressure curves can be closely described by experimentally fitting an equation of the form of the theoretical relationship given in Appendix I, Equation 11-A, which is rewritten as

$$f^2 = \frac{\alpha P}{(2\pi)^2 d\rho} + \left(\frac{4.8}{2\pi D}\right)^2 \frac{T}{\rho} \qquad (1)$$

where

D = Diameter of membrane

α = Average displacement of the membrane for unit displacement of the membrane center

P = Gas pressure about membrane

t = Thickness of membrane

d = Distance between membrane and driving electrode

f = Resonant frequency of membrane

f_o = "Vacuum" resonant frequency of membrane

For pressures below 500 microns f_o can be approximated by

$$f_o = \frac{4.8}{2\pi D} \left(\frac{T}{\rho}\right)^{1/2}$$

T = Linear tension on membrane* (force/length)

T' = Area tension on membrane* (force/area)

ρ = Area density of membrane

ρ' = Volumetric density of membrane

*Note that: $T/\rho = (T/t) \big/ (\rho/t) = (T'/\rho')$

SID 65-1026

Let

$$k = \frac{\alpha}{(2\pi)^2 d\rho} = \text{constant for a particular modulator}$$

Thus, Equation 1 can be expressed in the form:

$$f^2 = kP + f_o^2 \qquad (2)$$

By experimentally finding the resonant frequency for pressures of about 0. 1 mm and 20 mm and solving for k and f_o, Equation 2 can be used to calculate resonant frequencies over the range of 0. 1 to 30 mm (or greater). By using this procedure, interpolated values from Equation 2 were compared with experimental data from three separate Havar membranes. The results of this comparison revealed rms errors of 3. 5, 2. 1, and 0. 93 percent. Figure 17 shows the resonant frequency versus pressure curves for a pellicle and a Havar membrane. The end points were used to determine f_o and k, and Equation 2 was used to obtain intermediate values to draw the curves. The experimental values were then plotted to indicate the close nature of the "fit". Figure 18 shows a resonant frequency versus pressure curve, for a 12. 7 kcps Havar membrane, which has been extrapolated by using Equation 2. The constants were determined from experimental data taken at 0. 1- and 20-mm pressure. Caution should be exercised in using Figure 18 outside the 0. 1- to 30-mm range since this curve fitting technique has not been experimentally verified outside this pressure range.

A comparison between the k values (Table 3) of three Havar membranes shows an extreme variation of 10 percent. The data indicate that the variation in k might be a function of membrane tension. If this is true, the k value might be estimated to a high degree of accuracy (i. e. , appreciably less than the observed 10 percent variation) by simply finding the vacuum resonant frequency of the modulator.

Table 3. Resonant Frequency Data for Havar Membranes

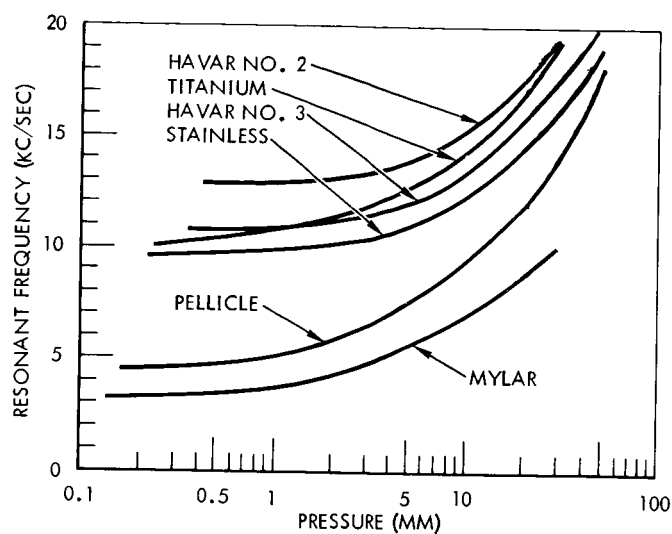| Modulator	Vacuum Resonant Frequency (kcps)	k Value $\left(\dfrac{(cps)^2}{\text{pressure in mm}} \right)$
Havar No. 2	12. 7	7.79×10^6
Havar No. 3	10. 6	7.25×10^6
Havar No. 4	8. 4	7.06×10^6

SID 65-1026

Figure 16. Characteristic Curves of Resonant
Frequency Versus Pressure
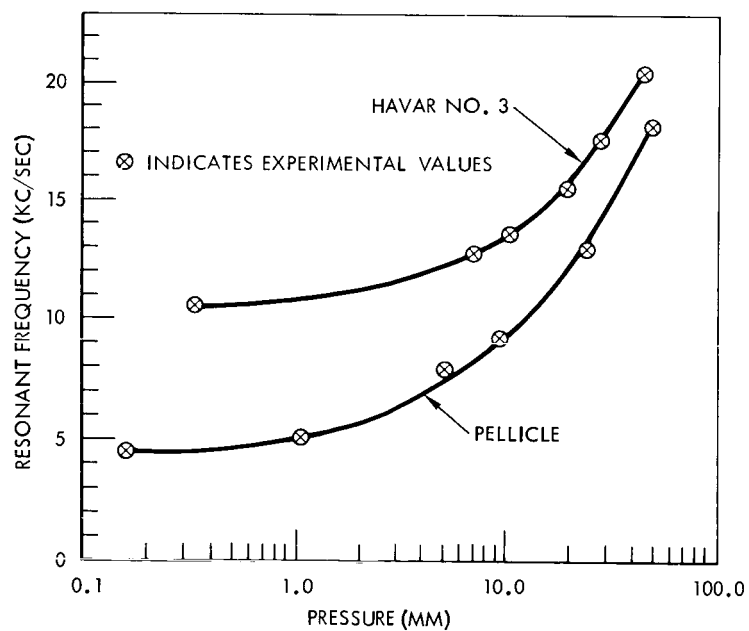
Figure 17. Comparisons of Two-Point Fit of
Theoretical Function With Experimental Data

- 33 -

SID 65-1026
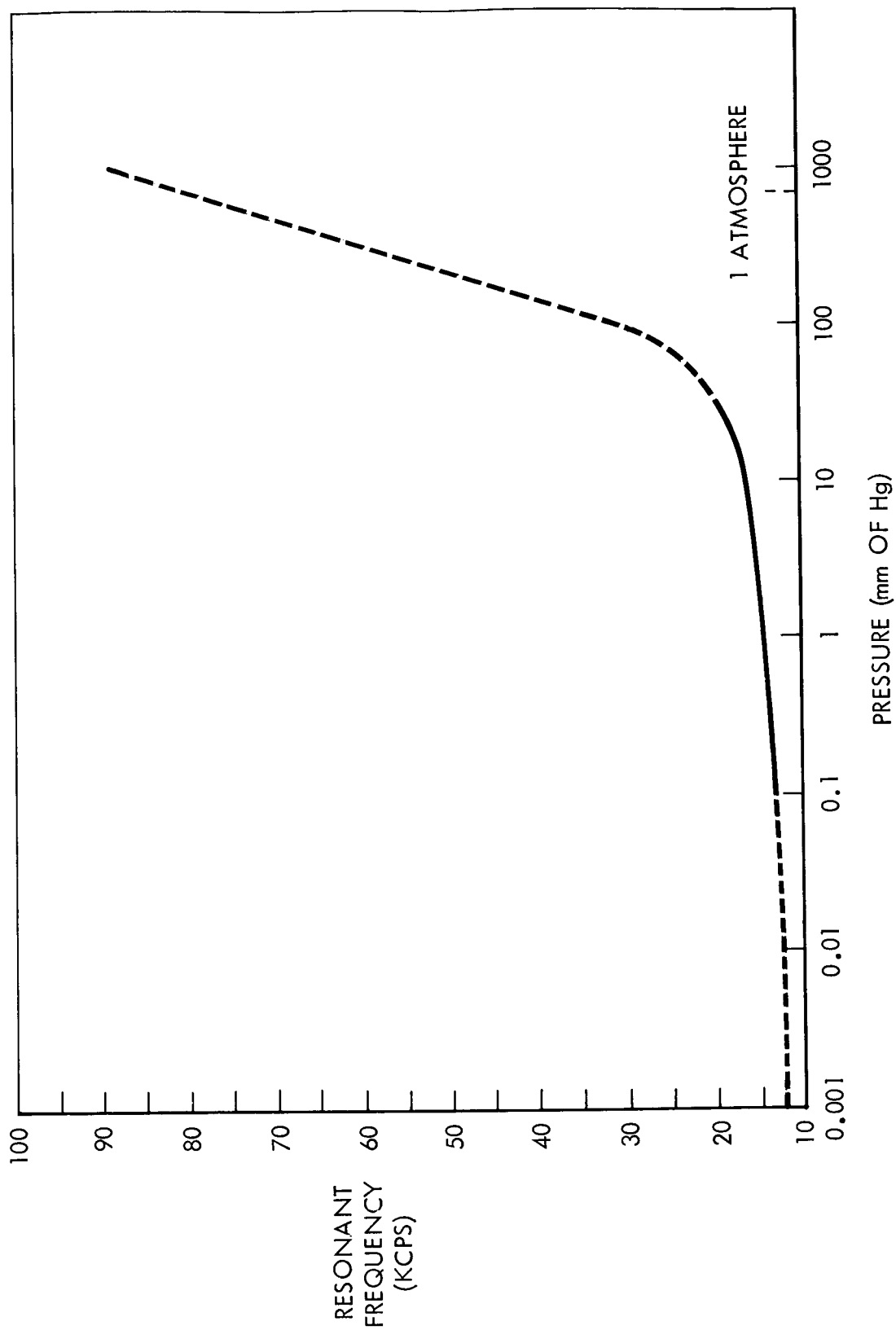
Figure 18. Resonant Frequency Versus Pressure (Extrapolated)

An important consequence of the predictability of resonant frequency with pressure is the future cost savings by a significant reduction in quality control and acceptance testing.

It should be emphasized that the data are limited to a small number of modulators. While the preliminary results are promising, it is insufficient to predict the performance of future modulators.

Distortion Measurements and Driving Voltage Requirements

Distortion is measured under far-field conditions and is defined as follows:

$$D = 100 \text{ x } \frac{\sum\limits_{i=1}^{n} A_i^2 - A_1^2}{\sum\limits_{i=1}^{n} A_i^2} \qquad (3)$$

where

A_1 = Amplitude of modulated radiation at the driving frequency

A_i = Amplitude of modulated radiation at the ith frequency which is any frequency over the entire audio range from 0.2 to 20 kcps.

Figure 19 shows a test setup schematic for distortion tests. A Dressen Barnes Model D-50 regulated dc power supply is used to bias the membrane. A Hewlett Packard Model 200 dc variable frequency sine wave generator is used to drive the membrane. At the output of the photomultiplier tube, all modulation outside the audio range (i.e., 0.2 to 20 kcps) is filtered out; the remaining signal is fed into the distortion meter. The distortion meter (H. P. MOD C-30B) is direct reading and has merely to be tuned to the driving frequency. Depth of modulation is measured by inserting a chopper between the laser and the collimator to give a 100 percent depth-of-modulation reference. These measurements were made with an rms voltmeter at the output of the photomultiplier. Simultaneously, driving voltage measurements were made with a VTVM.

Figure 20 gives the percent distortion versus driving frequency for a stainless steel modulator at different pressures and depths of modulation. When the driving frequency is at one-half of the resonant frequency, the second harmonic in the driving circuit excites the fundamental resonance of the membrane and consequently results in an apparent increase in percent distortion. This is the cause of the peak in the

Figure 19. Distortion Test Setup

distortion curve, which is at one half of the resonant frequency. The shift in the distortion peak with pressure is due to the shift in resonant frequency with pressure. However, when a membrane is pressurized such that its resonant frequency is above 20 kcps, thi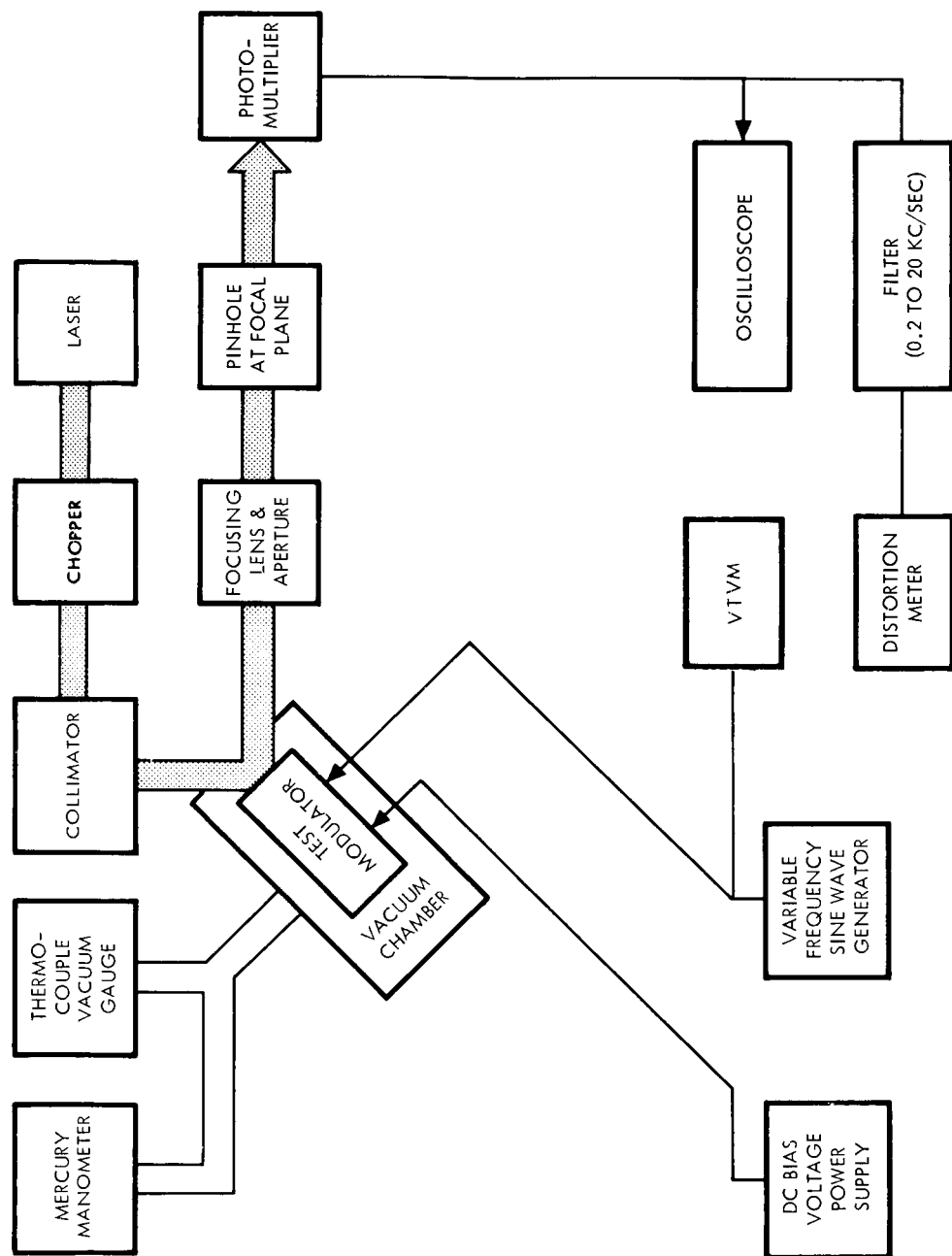s peak distortion will have a negligible effect on audio information. However, the distortion exclusive of this peak, increases with increasing pressure. This is illustrated in the 42-percent depth-of-modulation curve in Figure 20.

Figure 21 shows the driving voltage versus driving frequency at different pressures for a stainless steel membrane at a constant level of modulation. The two graphs are of the same scale to allow a comparison between 42-percent and 20-percent depth of modulation. It can be seen that for a 42-percent depth of modulation at 20 mm pressure, the driving voltage requirement becomes large. It can also be seen that the linearity of the driving voltage versus driving frequency curve improves at lower pressure.

An analysis has been completed on far-field modulation distortion for various values of modulator bias and drive signal amplitude. This analysis is presented in Appendix IV. The analysis was performed on a "single-ended," unpressurized modulator and cannot be readily extended to the pressurized case.

Optical Testing of Membrane Materials

Qualitative optical tests were performed on several membrane materials. Two of these materials, rolled metallic membranes of Havar and titanium, exhibited good mechanical properties (high resonant frequency, etc.) and one, an organic pellicle, had rather poor mechanical properties. For comparison, a series of photographs were taken of the membrane materials and an optical flat under simulated far-field conditions. Figure 22 shows the test setup used for photographing light reflected from the surface of the membrane. Figure 23 shows examples of photographs of far-field patterns from several membranes as well as an optical flat.

It can be seen from the radiant flux distribution in these photographs that, of the materials tested, the Pellicle and the Havar had the best optical qualities (specular reflectivity and flatness), while titanium, which has a bandwidth capability close to that of Havar, had poor specular reflectivity (i.e., the far-field pattern of titanium does not have a well-defined region exhibiting high radiant intensity at the center of its diffraction pattern). This accounts for the poor sensitivity exhibited by its dc transfer curve.

Based on this qualitative test and the response tests, Havar, a low iron-content stainless steel produced by the Hamilton Watch Company, was originally selected as the best membrane of these materials. As

SID 65-1026

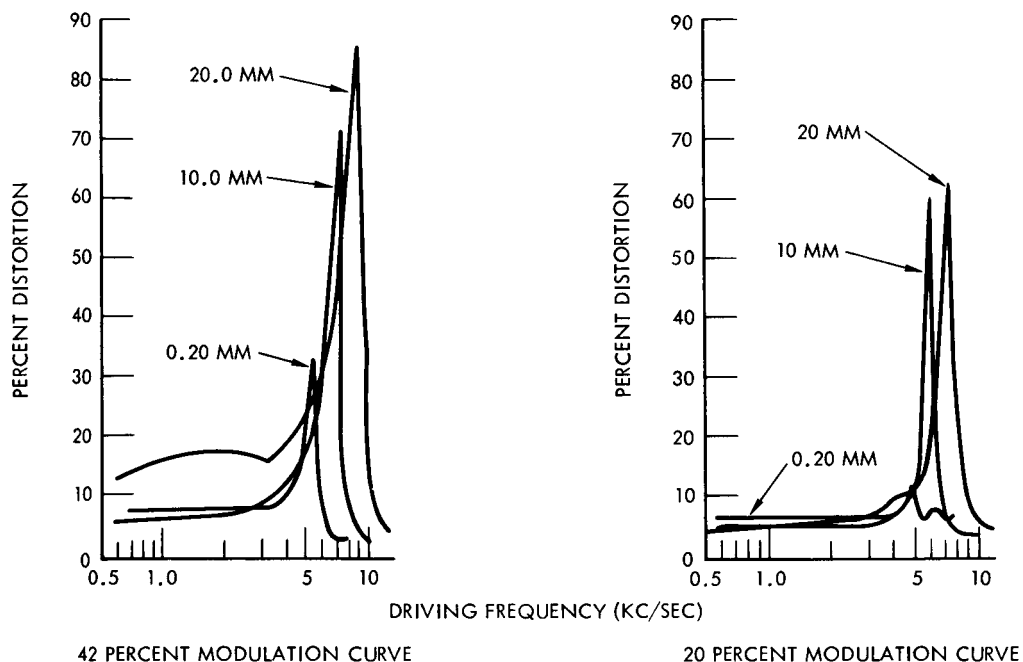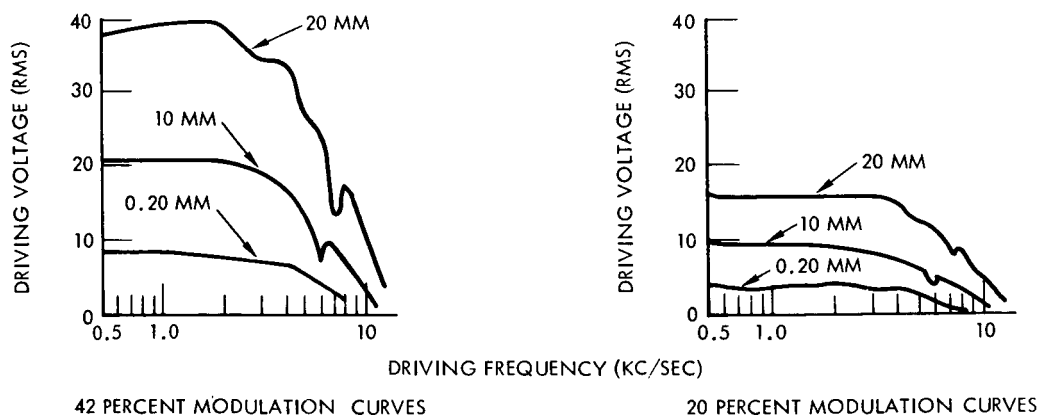Figure 20.   Distortion Versus Driving Frequency for
Stainless Steel Membrane

Figure 21.   Driving Voltage Versus Driving Frequency for
Stainless Steel Membrane

- 38 -

SID 65-1026
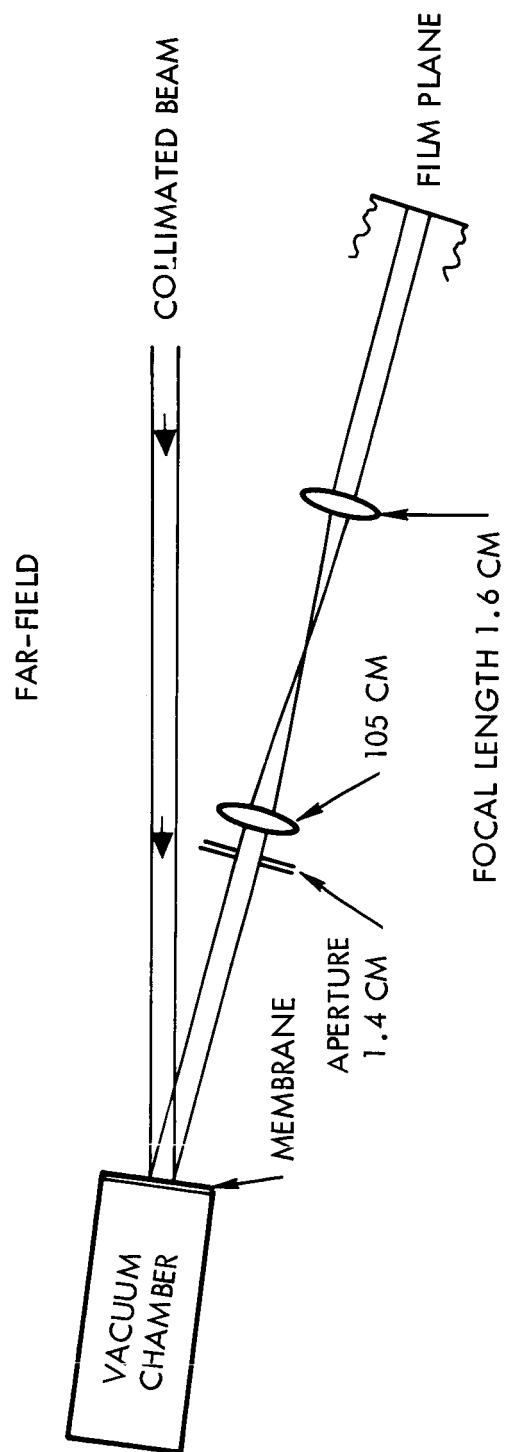
Figure 22. Test Setup for Photographing Far-Field Patterns of Laser Light Reflected Off Various Surfaces

OPTICAL FLAT
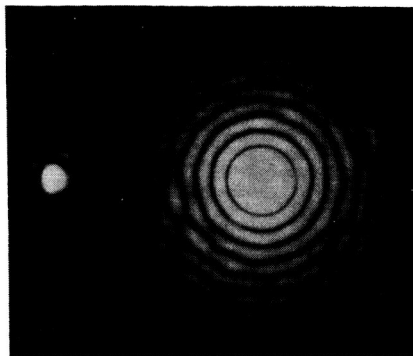
HAVAR
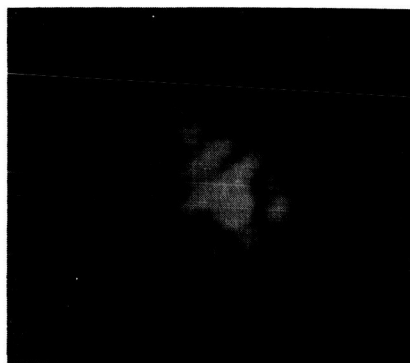
TITANIUM

PELLICLE
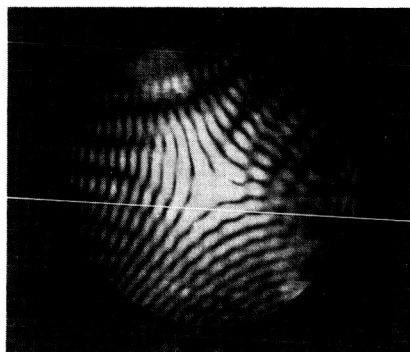
Figure 23. Far-Field Patterns of Laser Light Reflected Off Various Surfaces

shown in Table 4, it has the highest yield strength-to-specific gravity ratio, which gives it the highest potential vacuum resonant frequency of the materials studied. It also has reasonably good reflectivity and surface flatness. Later in the program, however, an improved membrane fabrication technique, known as replication, became available to us as the result of a separate program. Additional qualitative comparisons including the replicated membrane are presented in Figure 24, which shows the near-field pattern of light reflected from several surfaces. These photographs indicate very clearly the differences in surface quality of the various membranes. Because of the apparently excellent optical quality attainable by the replication process, it was decided to run a series of quantitative tests to compare a replicated nickel membrane to the Havar membrane.

Table 4. Realistic Maximum Vacuum Resonant Frequencies

Material	Yield /Specific Strength/ Gravity	Calculated Maximum Vacuum Resonant Frequency (kcps)
Mylar	9,250	9.6
Stainless Steel	15,800	12.6
Titanium	15,100	12.3
Havar	33,300	18.3

Experimental Comparison of Havar and Replicated Nickel Membranes. - A series of tests to obtain data on the power distribution in a beam of light reflected from a rolled Havar membrane and a gold-overcoated, replicated-nickel membrane was performed in the presence of the NASA Assistant Project Engineer during the week of September 20, 1965.

The tests were performed by directly measuring the radiant flux in the far-field pattern of radiation reflected from the membrane. The experimental measurement setup is illustrated in Figure 25. By using a 1.6-cm focal-length lens at the collimator, the 0.2-cm laser beam was expanded and recollimated at a diameter of 7.6-cm. The radiation was reflected off the surface to be tested, passed through a 2-cm aperture and brought to focus by a 105.4-inch-focal-length lens. The diffraction pattern was then reimaged at the plane of an adjustable aperture. The flux passing through this aperture was then detected by the photomultiplier tube. Twelve measurements were made of the flux passing through 12 different sized apertures. The aperture sizes were selected so that

OPTICAL FLAT

PELLICLE
MEMBRANE

REPLICATED THIN
FILM MEMBRANE

STAINLESS STEEL
MEMBRANE

HAVAR
MEMBRANE

MYLAR
MEMBRANE

Figure 24.   Photographs in the Near Field of Laser Light Reflected
Off Various Surfaces

- 45 -
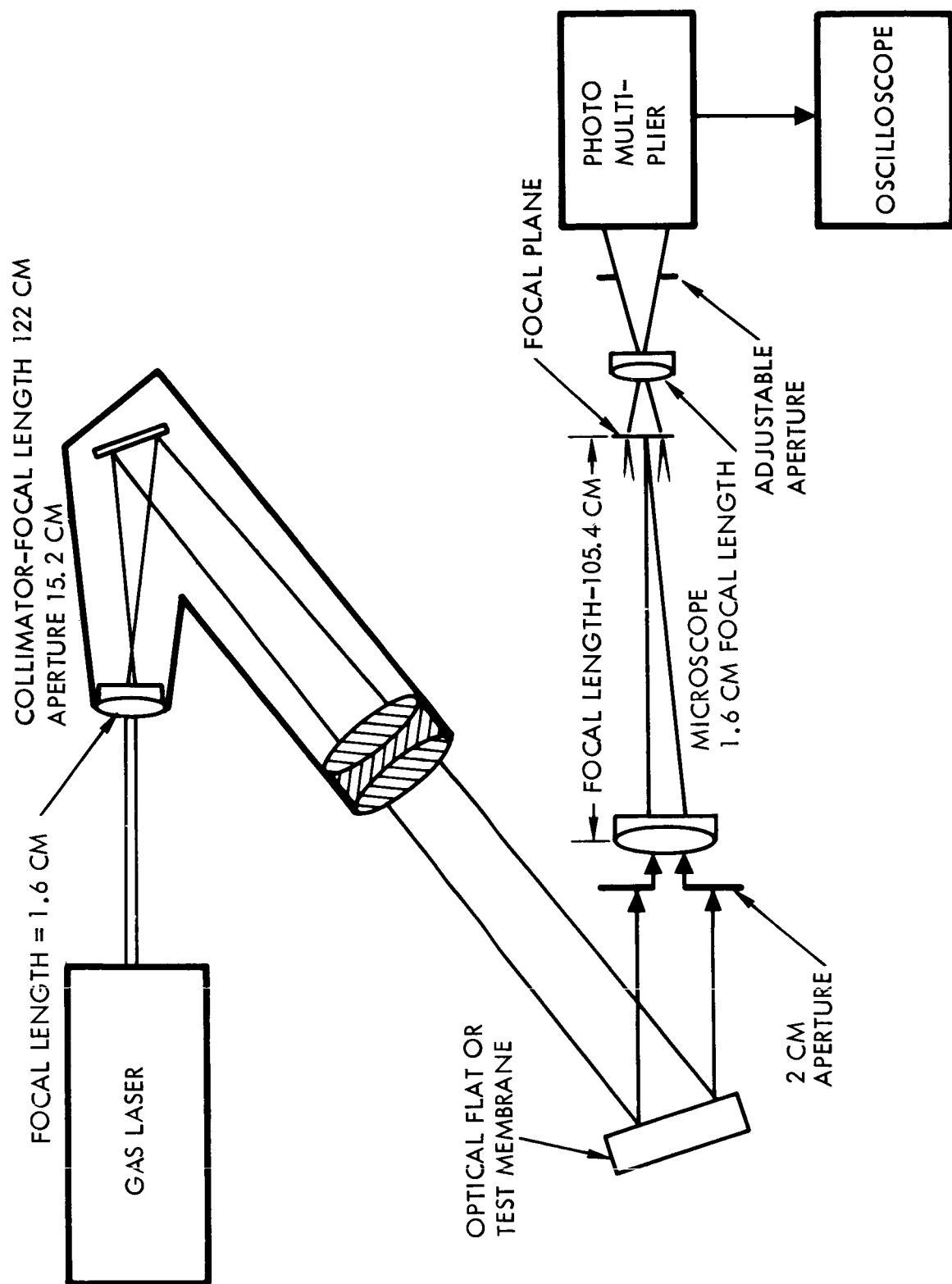
Figure 25. Optical Test Setup for Beamwidth Measurements

the smallest would admit the flux from a small portion of the central spot and the largest would admit all the flux out to the fourth dark diffraction ring. Hence, it was possible to get an indication of the angular flux distribution, and compare it to the theoretical distribution. The upper curve in Figure 26 shows the theoretically calculated[6] curve for a "perfect" reflective surface and uniformly illuminated aperture.

Measurements were then performed on the replicated nickel membrane. Figure 26 shows the actual distribution for this case. In addition, to evaluate the nickel membrane with respect to surface flatness (independent of reflectivity), these data have been normalized to 100 percent specular reflectivity (also plotted in Figure 26).

The results of the test made with the Havar membrane are also indicated in Figure 26. Comparison of this curve with the (actual) curve for replicated nickel indicates the magnitude of the improvement with the replicated nickel membrane.

A good quantitative comparison is provided by a measurement of the relative intensities from each of the surfaces in a small central region of the beam. Measurements were made of the flux within a central cone of 4.9 arc-seconds half-angle. These measurements appear in Table 5, which shows that the intensity at the center of the reflected beam from a replicated nickel membrane is approximately a factor of 10 greater than that from Havar. The improvement in the central far-field intensity is due to improved flatness and the absence of surface roughness in the replicated membrane. This improvement will allow a reduction of sagitta required for a given modulator and thus will lead to a reduction in required driving voltage and power, and a decrease in distortion for a given depth of modulation.

Table 5. Radiant Flux Contained Within a Half Angle of 4.9 Seconds Arc

Measurement	Membrane	Havar	Replicated Nickel
% of perfect reflector (Airy's pattern)		6.2	80
% of perfect reflector for membrane with 100% reflectivity		7.9	98

---

[6] Born and Wolf.
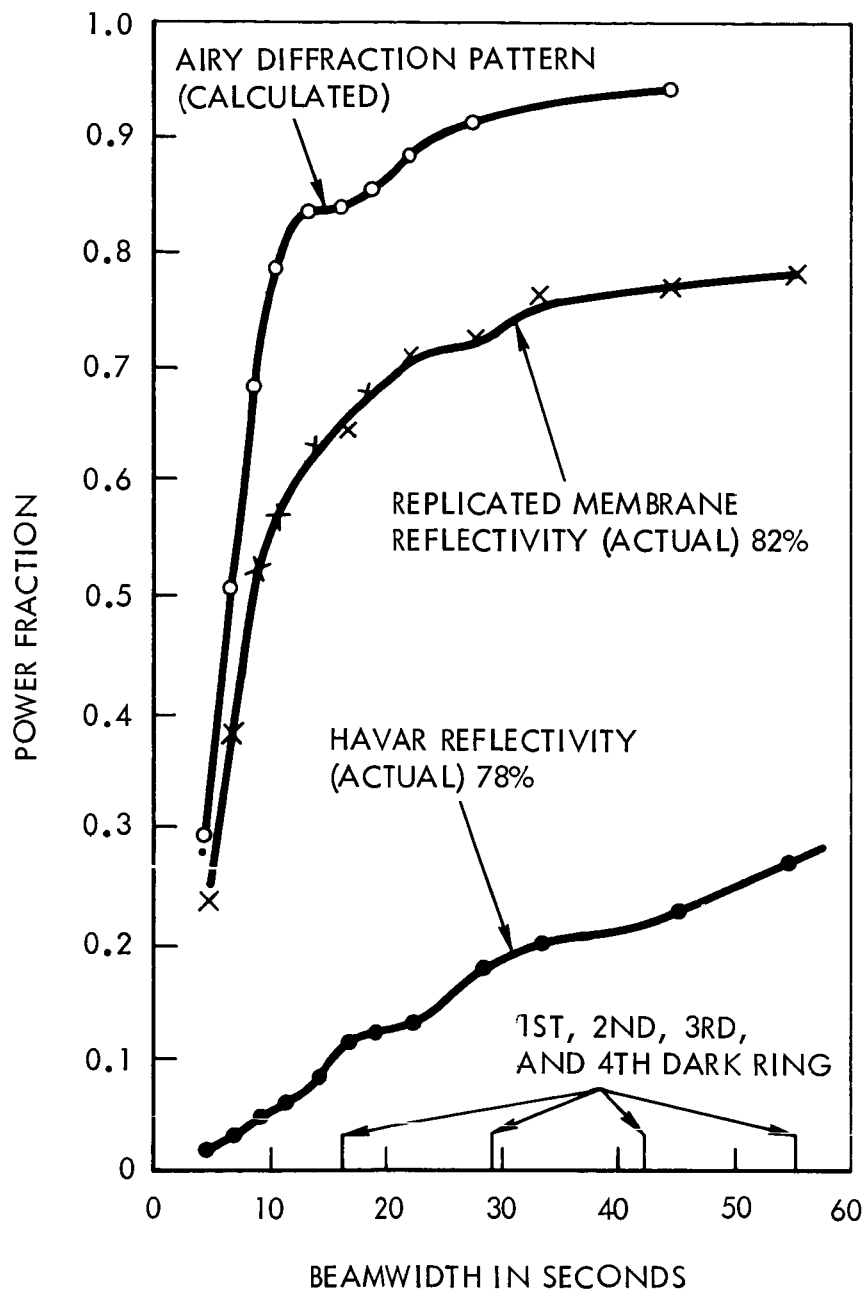
Figure 26. Beam Energy Versus Beamwidth

Since the diameter of the membrane of the modulator subassembly is limited in size (due to bandwidth considerations), it will be necessary to use an array of modulator subassemblies in the final MIROS package to obtain the required effective aperture. For performance considerations, it is important to know what the intensity distribution will be in the far-field diffraction pattern of such arrays. In particular, it is important to know if a high concentration of radiant flux will exist at the center of the far-field pattern.

A brief, subjective study of the far-field pattern produced by arrays simulating those for the MIROS package was conducted. The study was based on the assumption that the reflecting surfaces can be simulated by an array of clear apertures. By transmitting plane-parallel laser light through the apertures, the same result can be obtained that would be had by reflecting light from perfect or ideal modulator surfaces. Photographic transparencies containing various arrays of clear, circular apertures were used for this purpose. The transparencies were mounted on 35-mm slides and were used in the set-up illustrated in Figure 27. The resulting far-field patterns were then photographed on 35-mm EG&G XR film. This film was chosen to accentuate the fringes and off-axis detail of the far-field pattern. Figure 28 shows six examples of the photographs obtained. Subsequent study of the resulting photographs revealed that an array of MIROS modulators will provide, as anticipated, a high concentration of radiant flux at the center of the diffraction pattern. This, of course, does not consider the effect of nonparallelism between buttons or other imperfections in the actual MIROS package. In addition, the array of the MIROS package will be inclined with respect to the incident wave-front resulting in a far-field pattern of an array of elliptical rather than circular apertures.

CORNER REFLECTOR FABRICATION

The fabrication of the basic corner reflector to be tested and delivered was assigned to an outside supplier. Unfortunately, the supplier was unable to fabricate the component parts and assemble the corner reflector to meet a reasonable delivery schedule. NAA specialists have determined the technical reasons for the failure and have outlined in detail a fabrication technique that will yield a MIROS corner reflector assembly with a minimum of time and expense.

GAS LASER

FOCAL LENGTH ≅ 3.2 CM

1/20 λ FLAT

P-E 6-IN. f 8 COLLIMATOR

FOCAL LENGTH ≅ 105.4 CM

APERTURE
ARRAY SLIDE

DIAMETER 3 CM

FOCAL PLANE

FOCAL LENGTH = 1.6 CM
MICROSCOPE OBJECTIVE

35 MM XR FILM
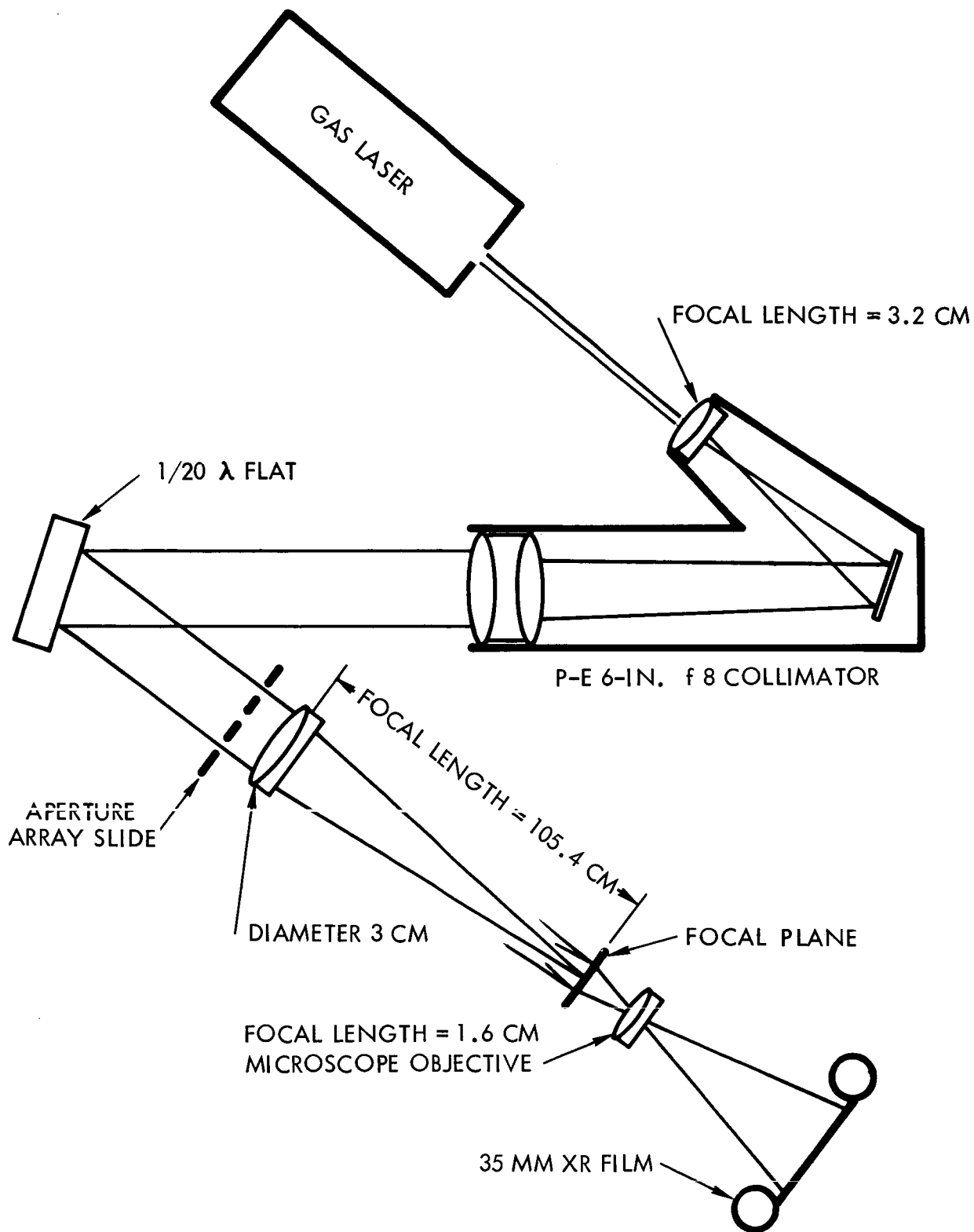
Figure 27. Multiple Aperture Setup
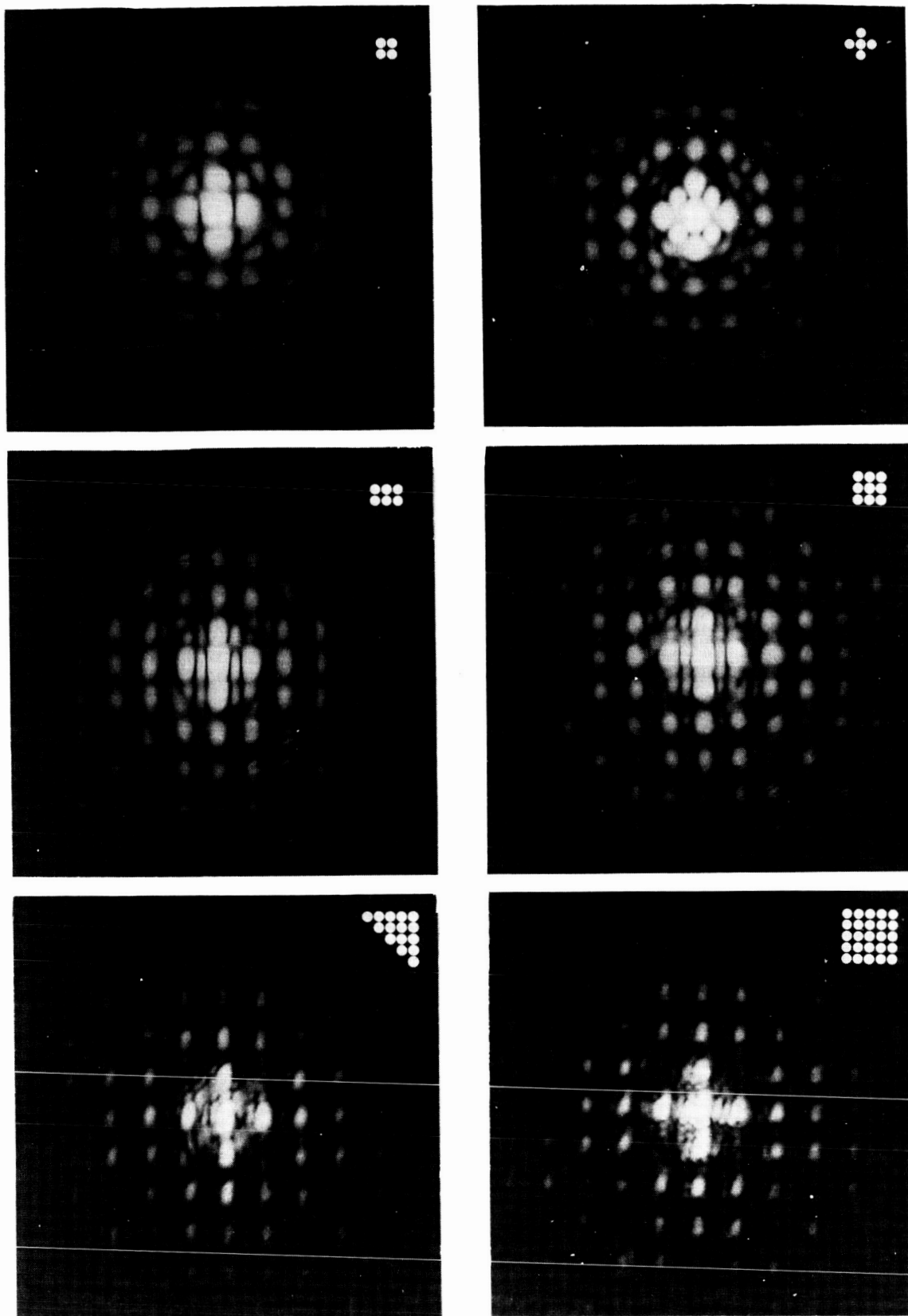
Figure 28.   Far-Field Patterns for Various Aperture Spacings

SID 65-1026

The following procedure has been carefully formulated to enable our optical technicians to meet the very exacting dimensional tolerances necessary for the fabrication of the MIROS corner reflector assembly illustrated in Figure 29.

1. Shape and flatten three high-quality fused-quartz discs from which plates A, B, and C are to be cut.

2. Cut the plates to size, aluminize surface E, and block plate C so that surface A can be finished in a special fused-quartz tooling fixture.[7]

3. Optically finish surface A perpendicular to surface E within 1 arc-second including the uncertainty of measurement, and to a flatness and surface condition that will allow optical contacting.

4. Optically contact plates C and B (surface A to surface F), then vacuum coat surfaces E and F with a reflective metallic coating for measurement purposes.

5. Grind surfaces B and C of the contacted assembly of plates C and B coplanar within 1 micron, with surface B perpendicular to surface E, and surface C perpendicular to surface F both within 30 arc-seconds.

6. Block the C and B plate assembly in a second special quartz tooling fixture.

7. Grind and polish the C and B plate assembly in the second fixture such that:

    a. Surfaces B and E are perpendicular within one arc second, including the uncertainty of measurement.

---

[7] These tooling fixtures are slotted, cylindrical devices into which the parts are cemented for optical finishing.
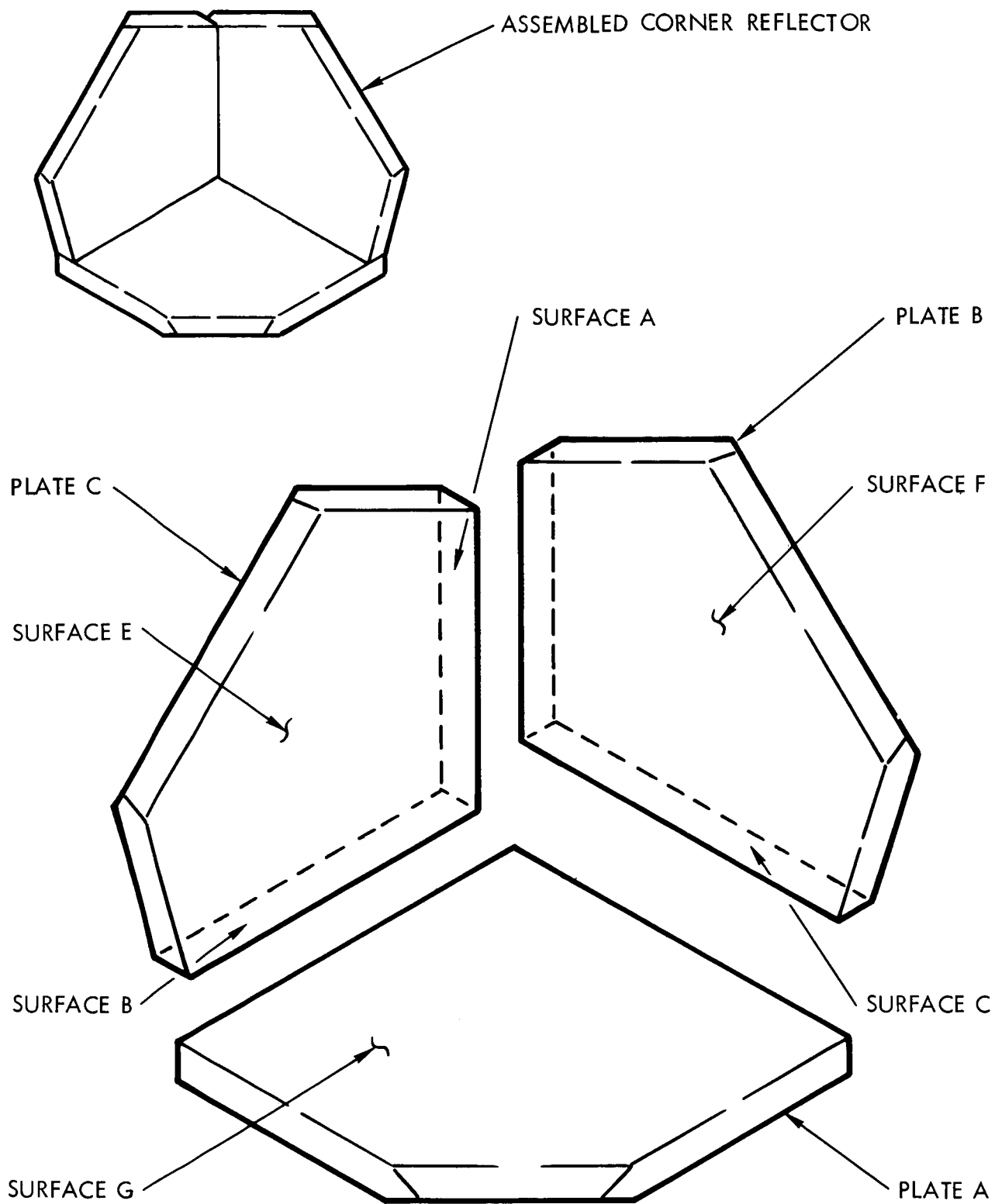
Figure 29.　MIROS Corner Reflector Assembly

b. Surfaces C and F are perpendicular within one arc second, as above.

c. Surfaces C and B are flat and coplanar within 600 Angstroms.

d. Surfaces C and B have a surface smoothness and polish that will allow optical contacting.

8. Optically contact the C and B plate assembly to plate A, thus forming the corner reflector configuration.

9. Grind mounting surfaces and assembly to final design dimensions.

10. Vacuum coat surfaces E, F, and G for measurement purposes.

11. Measure the flatness of E, F, and G and the perpendicularity of surface pairs both goniometrically and interferometrically.

A considerable time saving and increase in confidence is realized in Step 1 by fabricating plates A, B, and C from very high-quality fused quartz with very low internal strain and bubble content and by performing all of the optical processing of surfaces E, F, and G while the plates are in disc form. A great advantage in the "figuring" or final adjustment of flatness of these plates is realized from the circular symmetry of the disc shape. This advantage results from the fact that the nature of both hand and machine optical working will cause the surface of a part that lacks circular symmetry to assume a nonspherical shape (usually cylindrical or toroidal), while a circular part will work to a good spherical surface. Of course, the spherical surface of interest in this case is that of an infinite radius of curvature—a plane. Hence, a circular part can be made flat with sufficient precision to allow proper optical contacting to another sufficiently flat surface.

A nonspherical surface (resulting from working with a noncircular part) can be made spherical, with difficulty, either by hand working or by machine; but even though sphericity is obtained, it is even more

difficult to obtain "flatness." Hand working the surface affords, in the judgement of competent optical craftsmen, the greatest control of general surface shape but has two very serious disadvantages. The first is a tendency for the edge of a component, which, in this case, is a critical area, to be worked more harshly than the central portions resulting in what is called a "turned down edge." The second disadvantage is heating of the part due to handling by the optician. The heating distorts the part and makes it necessary to allow it to stabilize before any measurements or further work. This results in the necessity of short work sessions separated by long stabilization periods.

The supplier, unfortunately, expended more time on surfaces E, F, and G by trying to work with noncircular parts than they had estimated for the entire corner reflector fabrication. To complete the unit, NAA proposes to start by blocking plate C, as in Step 2, in a close fitting slot cut in a thick fused quartz disc. One face of the disc and surface A will be placed on a flat surface, then a nonshrinking, rigid, potting compound will be poured into the gap between the slotted disc and the plate. When the potting compound cures, surface A may be optically finished for both perpendicularity and flatness (Step 3).

When surface A is within tolerance, plate C can be removed from the plate C blocking fixture and optically contacted to plate B. Surfaces E and F can then be vacuum coated with a temporary coating of reflective metal to facilitate goniometric measurement accuracy (Step 4). The B and C plate assembly may then be hand and machine ground to provide the requisite geometry of surfaces B and C before blocking in the plate B and C blocking fixture (Steps 5 and 6). Surfaces C and B of the B and C plate assembly may be ground and polished as per Step 7 of the above procedure.

When Step 7 is complete, the assembly can be removed from the plate B blocking fixture and optically contacted to plate A (Step 8). The assembled corner reflector may then be ground to final design dimensions and vacuum coated (Steps 9 and 10) with a durable, overcoated, reflective aluminum film.

Five optical tests to comprehensively determine the optical characteristics of the corner reflector have been defined as follows:

1. Interferometric determination of the flatness of surfaces E, F, and G.

2. Interferometric determination of the perpendicularity of the three porro mirros formed by the intersection of surface pairs E, F; F, G; and G, E. This can be accomplished by replacing an end mirror of a Twyman-Green interferometer with each of the three pairs of mirrors.

- 58 -

SID 65-1026

3. Goniometric determination of the perpendicularity of the above pairs of mirros by comparing the angle of intersection of the surfaces, to an optical true square, accurate to 1/4 arc-second or better.

4. Interferometric analysis of the wavefront distortion produced by the reflection of plane wavefronts from the trihedral mirror (corner reflector). This is accomplished by replacing an end mirror of a Twyman-Green interferometer with the corner reflector assembly and positioning the corner reflector so the reflected beam is sent axially back through the interferometer for wavefront comparison.

5. Determination of the diffraction image degradation of the corner reflector. This can be made by measuring the energy distribution of the Airy pattern of a pinhole image projected through a diffraction limited auto-collimator applied to the corner reflector. This energy distribution can then be compared to that of diffraction limited plane mirror in the same setup. Both distributions, moreover, can be compared to the distribution predicted by theory.

Although some of the tolerances and processes necessary for the fabrication of this element are difficult and the attending measurements require extreme care and attention to detail, all are within the state of the art and well within the present capability of the NAA Electro-Optical Laboratory.

DESIGN OF THE MIROS PACKAGE

Basic Assumptions and Approach to the Design

Several factors have influenced the approach to the design. First, the end use of a MIROS package is not presently known, although several possible mission uses have been discussed. Second, the vehicle environment in which it must operate is not well known and can vary significantly. Third, the optimum configuration of the retromodulator is not yet known.

Because of the above mentioned unknowns, it was decided early in the program that the design should have a flexibility that would not be required in an instrument designed for a specific mission on a particular vehicle with known solar orientation. Therefore, the present design is larger and weighs more than might be necessary; this will allow larger retromodulators to be used if necessary. A glance at Figure 30 will show that the method of sealing is not the best one for long life under space conditions. It is, however, an effective way of sealing for short periods of time and lends itself to disassembly and reassembly. This is

2.937

2.218 DIA

HOLD DOWN BRACKET

TENS

RECEIVER APERTURE

12.00

9.125 DIA

WINDOW

MODULATOR
BUTTON

RETAINING RING

.506

CORNER REFLECTOR

O'RING SEAL

FRONT COVER

5.168

12.00

RECEIVER VIEW SEPERATED FOR CLARITY
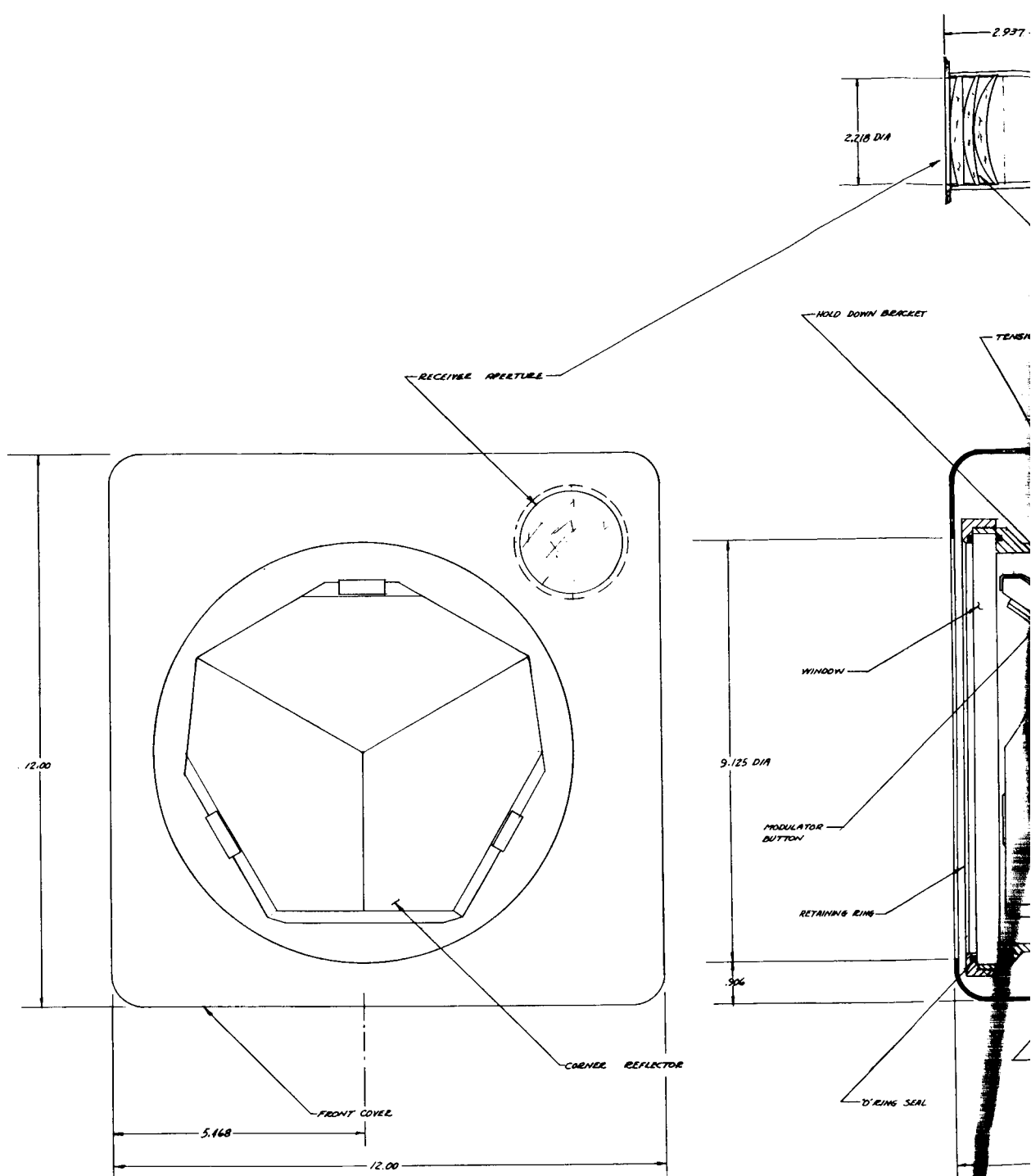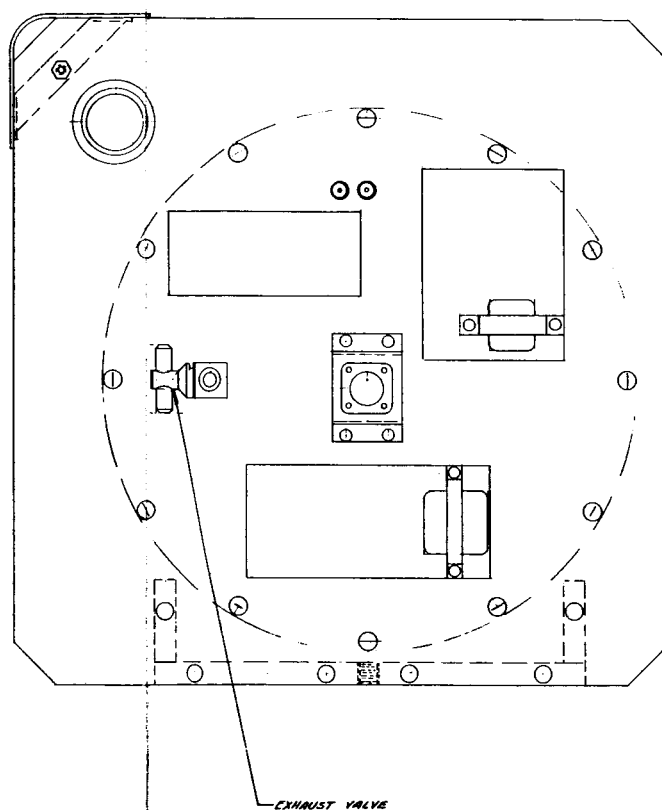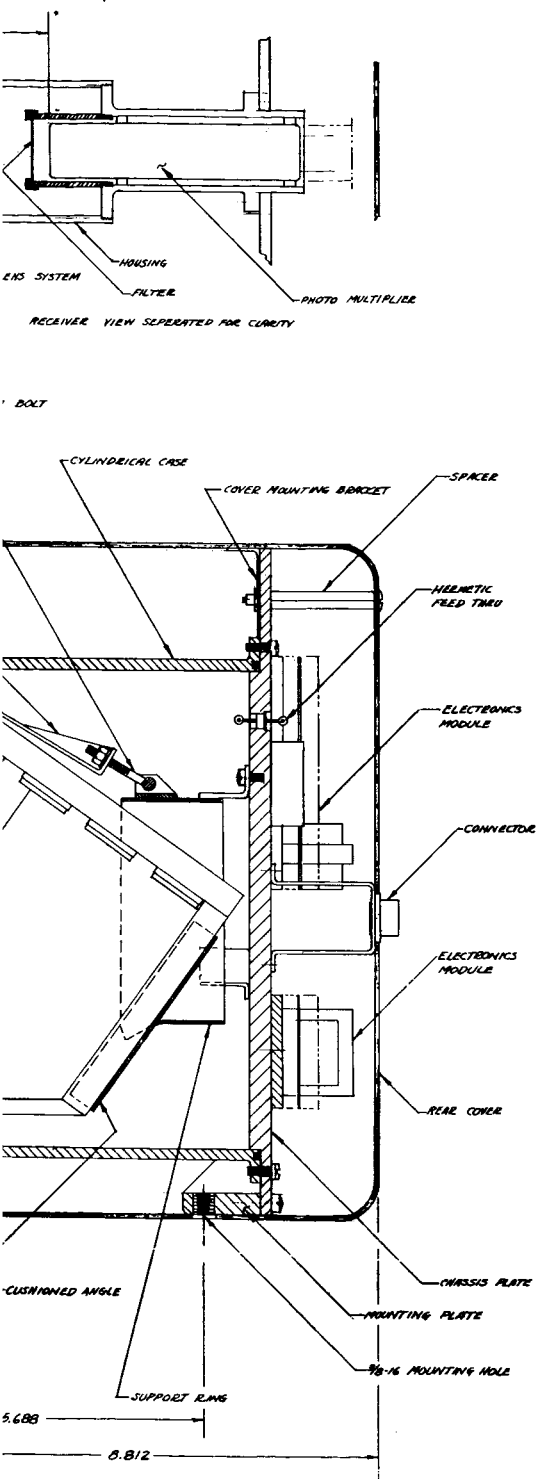
Figure 30. Modulation-Inducing Retrodirector Optical System
(MIROS) Assembly Drawing

- 61, 62 -

an example of the approach used in the design to make it easy to work with or modify, since the expected usage of this present model will be for evaluation and feasibility tests in a research and development type laboratory on the ground, even though space environments may be simulated during some of these tests. A further example of this design approach can be seen in the use of a valve on the vacuum line leading to the space around the retromodulator rather than a vacuum pinchoff tube that can only be used once. By this simple means of valving, different gases and pressures can be used to optimize the resonance rate of the modulators.

This design approach allows flexibility in the ground testing portion of the program. At the same time, redesign into an optimum package for space use is held to a minimum because the costly parts of the package will already be fabricated and proven in the shell of the present design. The retromodulator, driver amplifier, power supply, and optical receiver will only have to be repackaged in a smaller, lighter, more efficient structure.

Discussion of the Design

Design Concept

Figure 30 is an assembly drawing (Reference Drawing 74340747) of the MIROS system, and illustrates the assembly of the corner reflector and its associated hardware. The design is based on the unit being restricted to earth-bound use and testing. If the assembly is to be used on a space vehicle, the design would include permanent vacuum sealing, and eliminating the capability of easy disassembly and re-evacuating. For long periods of space use, the O-ring seals would be replaced with special solder seals, such as the indium-alloy solders. These seals are semi-permanent, which is a requirement for space use, and can be reopened if necessary.

In the assembly drawing, the support brackets for mounting the corner reflector in the vacuum chamber are sufficient for use in the laboratory or the field, but have not been analyzed for possible launch and space use. Silicone-rubber cushions between the support brackets and the corner reflector are indicated but are not drawn in full detail. The cushioned angle shown along one edge of two contacted faces is part of the support ring holding the entire reflector assembly to the chassis plate. A single casting for the support mechanism is preferred to an assembly of welded and screwed-together parts.

The support ring, which is not shown in full detail, consists of a triangular cradle with three cushioned angles supporting the three contacted edges. The cradle in turn is mounted in and is an integral

SID 65-1026

part of the support ring. As shown in the drawing, the support ring is also used to anchor the three hold-down brackets which clamp onto the three edges of the corner reflector.

Mounted on the reverse side of the chassis plate are the various electronic modules. For compactness, these could be mounted in and around the vacuum housing. The present design, however, was chosen for ease of assembly and subsequent servicing, if required. These electronic modules consist of (1) a power supply, (2) a retromodulator driver, and (3) a receiver.

By using one main piece of the structure as a common mount for all the subassemblies, alignment and stability problems are minimized. For example (Figure 30): The chassis plate is the common structure for the mounting plate and cover, the optical receiver, the retromodulator and window, the driver amplifier, and the power supply. This minimizes tolerance buildups and helps maintain boresight alignment between the retromodulator optical centerline and that of the optical receiver. While this concept uses only a few parts, the space version of the design would be still simpler — probably one lightweight casting would replace over half the structural parts of the present design.

Size and Weight

The overall size of the MIROS Package is 12 by 12 by 8.8 inches. Its weight is 26 pounds; Table 6 shows the manner in which this is distributed. Although eleven items are listed, there are naturally more parts than this; each item either represents itself, as well as those parts which make it up (in the case of an assembly), are mounted to it, or are adjacent to it.

Retromodulator

Construction. The retromodulator is a corner reflector with one of its surfaces containing modulator subassemblies (Figure 1). With this arrangement, an unmodulated light beam that enters the corner reflector leaves it as a modulated beam.

The basic portion of the retromodulator consists of the three mutually perpendicular reflecting faces of the corner reflector, which is sometimes referred to as a retrodirector or a retroreflector. The "optical axis" of the corner reflector makes equal angles with the three reflecting surfaces, which are mounted with an accuracy of one-second maximum error in the three 90-degree angles. Thus, an entering beam of light will be returned to its source with a very small beam spread, depending upon the accuracy of the corner reflector.

Table 6. Estimated Weight Distribution of MIROS Package

Item	Weight (lbs)
Retromodulator	3. 50
Covers	3. 10
Window	3. 45
Cylindrical case	4. 65
Chassis plate	3. 84
Electronics	3. 00
Mounting plate	0. 36
Support ring	0. 75
Optical receiver	1. 73
Miscellaneous hardware	1. 50
Total	25. 88 ≈ 26

The three plates which form the reflecting faces are produced with surfaces flat to better than 1/10 wavelength of light. For optical contacting surfaces, two edges of one plate and one edge of the second plate are polished flat to 1/10 wavelength of light and perpendicular to the faces to within an accuracy of one second. The first plate has one edge finished to the required accuracy and is then placed in optical contact with the reflecting face of the second plate. The two edges of these two plates, which will be contacted to the third plate, are then polished to the specified 1/10 wave flatness and one-second squareness. The third face is contacted to these two edges, forming the completed corner reflector. The three reflecting surfaces can be placed in a vacuum chamber and coated with aluminum or gold.

The overall size of the reflector provides mounting capability for 33 individual modulators on one reflecting face. This provides an on-axis effective aperture of 167 square centimeters and approximately 100 square centimeters for the 20 degree off-axis condition.

SID 65-1026

<u>Analysis (Bandwidth and Effective Aperture Area).</u> The effective
aperture area of the MIROS corner reflector is determined by the number
of the individual modulator units and their individual effective areas as
reduced by the total system transmission, vignetting, etc.

The various factors modifying the aperture area will be defined and
discussed separately. The cumulative effect can be written mathemati-
cally as follows:

$$Ac = N A_M V T$$

where

Ac = Net effective projected area of MIROS retroreflector

N   = Number of modulator buttons

A_M = Projected area of the individual modulators at the aperture

V   = All vignetting and off-axis losses

T   = All transmission and reflectivity losses.

The number of modulators can be calculated from the above equa-
tion when the effective aperture area has been specified for the off-axis
conditions. The requirement set forth in the statement of work for the
MIROS retrodirector is 100 square centimeters effective aperture area
when used 20 degrees off the nominal optical axis of the corner reflector.
The optical axis of the retroreflector is defined as an axis making equal
angles with the normals of the three reflecting surfaces.

The projected area of each individual modulator button is given by

$$A_M = \pi r^2 (\cos \theta) (n)$$

where

r = semidiameter of the modulating area, i. e. , 1 cm

θ = angle between optical axis and the normal to the modulating area

n = effective number of ways light entering the aperture of the
    corner reflector can be modulated by each individual modulator
    button.

- 66 -

The magnitude of "n" can be evaluated by considering the number of ways light entering the aperture of the corner reflector can be reflected from one specific area, such as one modulator.

Light entering the corner reflector is internally reflected three times before leaving the corner reflector and being retrodirected. Light can be reflected from a modulator button immediately after entering or immediately before leaving the aperture of the corner reflector. This will produce a doubling of the effective area of a modulator.

Light can also enter the corner reflector and be reflected from a mirror surface before striking the modulating surface, after which the light is retrodirected by the third reflection from the second nonmodulating mirror surface. There are two possible paths for the light to traverse the corner cube reflector with the modulation occurring at the second reflection.

Thus, the value of "n" is equal to 4, which yields a value of

$$A_M = \pi \, (1)^2 \left(\frac{1}{\sqrt{3}} \right) (4)$$

$$= 7.28 \text{ sq cm}$$

The value of V, the sum of all the vignetting and off-axis losses, is determined by considering the geometry of the MIROS configuration. It is assumed that the optical window is large enough to prevent any vignetting at the entrance aperture of the system.

An analysis of the off-axis properties of the corner cube reveals losses much greater than would be expected from a simple cosine relationship. For full transmission, the exit aperture should be a mirror image of the entrance aperture with no vignetting.

An analysis of the vignetting produced by off-axis utilization was given in a NASA memorandum, April 23, 1963, by Mr. Peter Minott of the Optical Systems Branch, Goddard Space Flight Center. From the theoretical curve of this report, a value of 60 percent is a reasonable value to use for "V," and is very close to the values for various orientations obtained in the Phase I program.

The transmission and reflectivity losses, "T," are produced by losses from transmission through the optical window and internal reflection within the corner cube reflector.

A plain, uncoated window of fused silica, with an index of refraction of approximately 1.46, will transmit about 93 percent of the incident radiation. A low reflection coating of magnesium fluoride, because of the poor index match with fused silica, will only increase the transmission to approximately 96 to 97 percent.

Multiple layer coatings, described as "high-efficiency coatings," can increase the total window transmission to better than 99.5 percent.

The total reflectivity loss within the corner cube reflector is the product of the reflectivities of the three reflection surfaces. The surface reflection is determined by the smoothness or surface roughness of the reflecting surface; the material, aluminum or gold, which is used as the high reflectivity surface; the wavelength of light under consideration; and the angle of incidence with which the light strikes the reflecting surface.

If the 6328 Angstrom laser light is used with the MIROS retrodirector, gold would be preferable to aluminum because of the higher reflectivity of gold at this wavelength. If there is a possibility that other visible wavelengths will be used, however, aluminum has better over-all visible reflectivity than gold.

The surface smoothness and aluminum as the reflecting material will produce a reflectivity of approximately 90 percent for the two nonmodulating fused silica surfaces.

The reflectivity of the third modulating surface is primarily a function of the surface roughness of the membrane material. The best material measured was vacuum-evaporated nickel. Nickel may not be the best material choice, but the evaporation technique of material preparation is superior to metal rolling to produce membranes.

The measured reflectivity of the nickel membrane was 85 percent. The transmission factor, "T," is the product of these reflectivities as follows:

$$T = (0.90)(0.90)(0.85)(100 \text{ percent})$$

$$= 68.9 \text{ percent}$$

A minimum number of modulating buttons, N, is thus calculated from the evaluated factors as follows:

$$Ac = N (A_M) VT$$
$$100 = N (7.28)(0.60)(0.689)$$
$$N = 100/3.010 = 33$$

SID 65-1026

Figure 2 (Phase I Final Report) illustrates the packing density of the modulators. The difficulty encountered in producing a corner cube reflector will increase with an increase in size. Perkin-Elmer have produced small corner reflectors, but were unable to produce the larger unit ordered during the Phase II program.

A single corner reflector large enough to contain 33 modulators (Figure 1) will be 20 percent larger than the size in the Phase I report, and will therefore be more difficult to produce.

If it is too expensive to produce a single large corner reflector, the modified three-unit corner reflector array, which is shown in Figure 31, would be the preferred choice for the configuration. This triple array, with 13 modulators per unit, will yield a total value of 39 for N and a total effective aperture area at 20 degrees of 117.5 square centimeters, or 196 square centimeters on axis. The answer to this problem of size and configuration will come from the process of completing the corner reflector.

Window

The window of fused silica has a clear aperture of 10.75 inches, which is large enough to prevent vignetting for off-axis angles up to 20 degrees. A thickness of 1/4 to 3/8 of an inch would be sufficient for vacuum use with a safety factor of two or three. To aid in the production of sufficiently flat surfaces, however, the window thickness was increased to 1/2 inch.

Electronic Design

The major electronic components of the MIROS package include the optical receiver, the retromodulator driver amplifier, and power supply. These are located as shown in Figure 30. Modular welded wire construction will be used throughout to provide the reliability and ruggedness required to survive the launch environment and to perform throughout the operational lifetime required in the space environment. A block diagram of the MIROS package electronics is shown in Figure 32. Electronic characteristics are summarized in Table 7.

Optical Receiver

The optical receiver is located in one corner of the MIROS package. It consists of a triplet objective lens, a replaceable spectral filter, an "end-looking" photomultiplier tube, a preamplifier, and an automatic gain control circuit. The optical axis of the receiver is boresighted parallel to the nominal "optical axis" of the retromodulator. The dynode resistors and preamplifier are mounted directly on the mounting end of the photomultiplier tube.
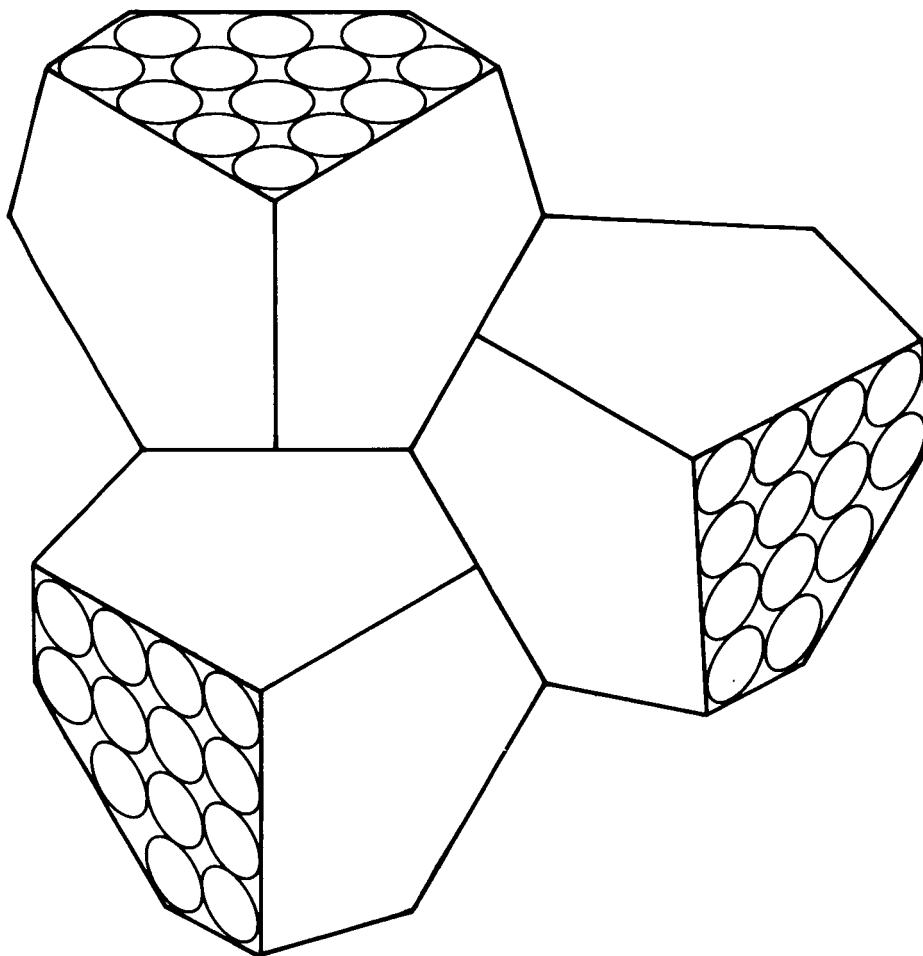
NOTE:

MODULATING SURFACE SHAPE
MODIFIED FOR MORE EFFICIENT
PACKING DENSITY OF
MODULATING ELEMENTS

Figure 31. Three-Unit Corner Reflector Array
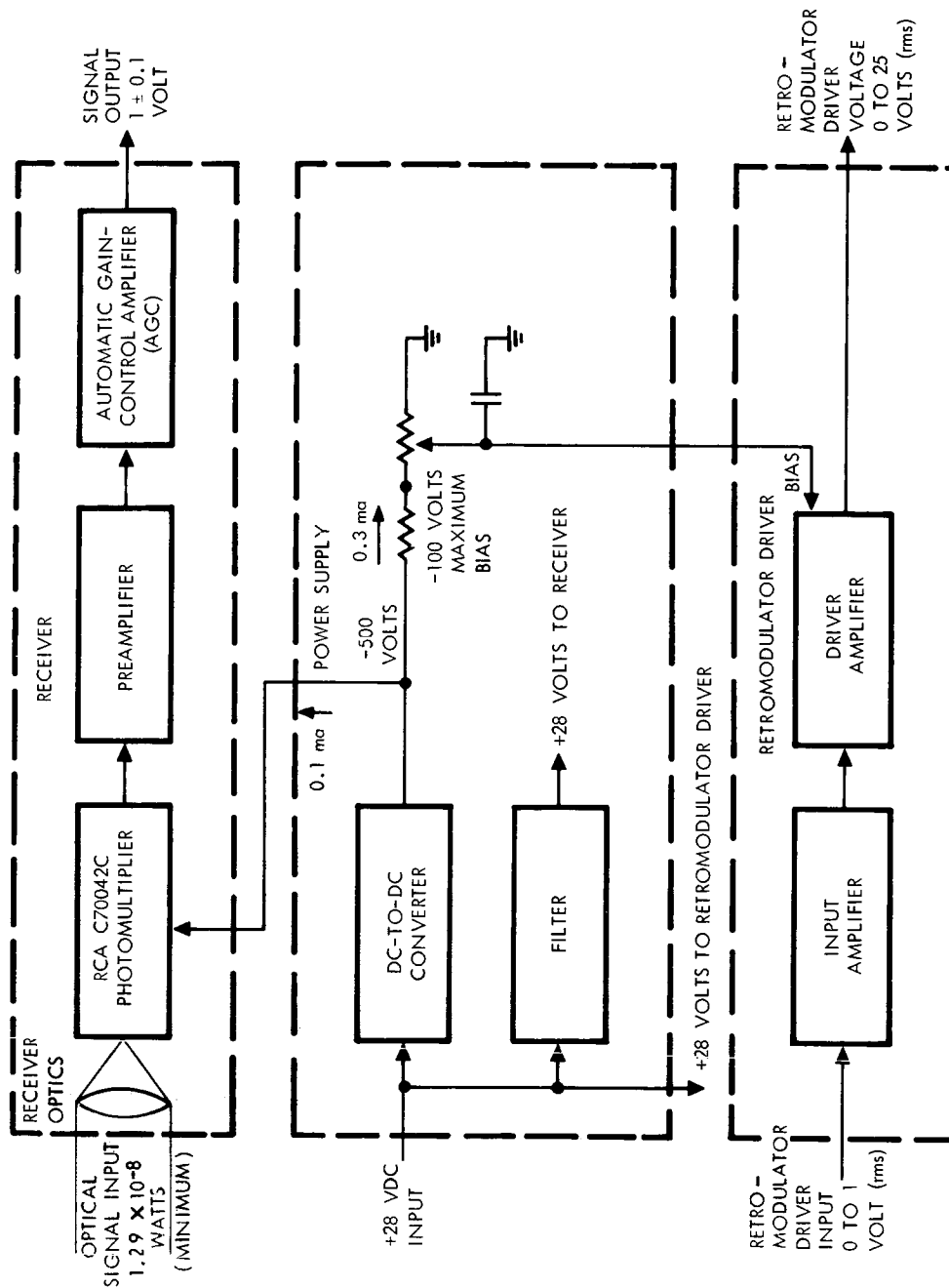
Figure 32. MIROS Electronics Block Diagram

Table 7. Electronic Component Characteristics

Component	Input	Output	Bandwidth	Dynamic Range
Receiver	Radiant power on photo-cathode: 1.29×10^{-8} watts (1000 km range) 1.29×10^{-6} watts (100 km range)	1 ± 0.1 volt over input range at an output Impedance 100 ohms	10 cps to 20 kc	10^3 maximum
Modulator driver	Voltage: 0 to 1 volt Impedance: 500 k ohms	To modulator: 0 to 25 volts (rms) with 0 to 100 volts adjustable bias	300 cps to 20 kc (±1 db over range)	
Power supply	Voltage: 28 ± 1 volts dc Current: 55 ma	28 volts dc (filtered) 500 volts dc (photo-multiplier bias)		

The optical receiver was designed to detect incident radiation from a distant transmitting laser source and to provide a signal in a form suitable for: (1) driving an optical modulator, (2) use as an input to a RF modulator, and (3) obtaining a photosignal output.

A nominal operating range of 0 to 1 volt (rms) was used for the above items to provide a reasonable operating level for all system components.

Specified receiver parameters which form the basis for the design include:[8]

1. Collecting aperture diameter = 6 cm

2. Field of view (half-angle) = 20 degrees

3. Narrow spectral filter to discriminate against radiation from the sunlit earth.

The spectral filter bandwidth used (5 Angstroms) represents an engineering compromise which provides the narrowest bandwidth obtainable at a reasonable cost. Filter transmission is approximately 45 percent at the peak wavelength of 6328 Angstroms. Optical efficiency for the filter and triplet lens combination is approximately 40 percent for the signal and slightly less for the background because of the filter rolloff.

The above requirements, together with a reasonable transmitting laser power (assumed to be 100 milliwatts), were used to determine the system sensitivity and for the receiver design and specification, as discussed in the paragraphs that follow.

Receiver Sensitivity

All system parameters used in calculating system sensitivity and range are given in Table 8 which lists the symbol, definition, units, and design value used for each.

For a system range of 1000 km the input signal power to the photodetector, P_m, = 1.29×10^{-8} watts. Background power, P_b, = 3.78×10^{-5} watts. The system signal to noise ratio (voltage) is given by:

$$S/N = \frac{\eta\, P_m}{\sqrt{2e \left[\eta\, (P_m + P_b) + I_D \right] \Delta f}} \tag{1}$$

where

η = Photocathode sensitivity (amp/watt)

P_m = Input signal power to photodetector

P_b = Input background power to photodetector

I_D = Photocathode

---

[8] RFP No. 72138, NASA, Goddard Space Flight Center, dated May 8, 1964

SID 65-1026

Table 8. Optical Receiver Parameters

Symbol	Parameter Definition	Units	Design Value
P_t	Transmitting laser power	Watts	0.100 (assumed)
θ_t	Half-angle of transmitter beam divergence cone (10 sec)	Radians	4.86×10^{-5} rad
Ω_t	Solid angle of transmitted divergence cone = $\pi\theta_t^2$	Steradians	7.42×10^{-9}
I_t	Radiant intensity of transmitted beam, assuming that all of the power is uniformly distributed within the divergence cone = $P_t/\pi\theta_t^2$	$\dfrac{\text{Watts}}{\text{Steradian}}$	1.35×10^7
A_m	Projector area of MIROS sensor optics	Meters^2	2.83×10^{-3}
R	Range	Kilometers	1000 (maximum)
τ	Atmospheric attenuation	—	0.84 (Bayley)
ω_t	Power incident on satellite collecting optics (signal) $P_t A_m \tau/\pi\theta_t^2 R^2$	Watts	3.21×10^{-8}
ϕ_M	Half-angle of the space-borne MIROS receiving field-of-view cone (20 degrees)	Radians	0.35
$\Delta\lambda_m$	Wavelength interval in which radiation is received (spectral filter bandwidth)	Angstroms	5 Angstroms centered at 6328 Angstroms
P_m	Total signal power on the MIROS receiver photodetector = $W_t \epsilon_o$	Watts	1.29×10^{-8}

Table 8. Optical Receiver Parameters (Cont)

Symbol	Parameter Definition	Units	Design Value
ϵ_{o_s}	Optical system efficiency (3 lenses + 1 filter) for signal	-	0.40
B_d	Background spectral radiance (sunlit earth, worst condition 1[1])	Watts/m²-steradian-Angstroms	1.73×10^{-2}
H_b	Background spectral irradiance at the receiver = $B_d (\pi)(\phi_M)^2$	Watts/(m²) Angstroms	6.67×10^{-3}
ω_b	Power incident on satellite collecting optics (background) = $H_b A_m (\Delta \lambda_m)$	Watts	9.45×10^{-5}
P_b	Total background power on the MIROS receiver photodetector = $\omega_b \epsilon_{o_b}$	Watts	3.78×10^{-5}
ϵ_{o_b}	Optical system efficiency (3 lenses + 1 filter) for background	-	0.40
η	Photodetector sensitivity (S20 surface at 6328 Angstroms)	Amps/watt	0.026
Δ_f	Information bandwidth	Cycles/sec	20 kc

[1] Ref D. S. Bayley (See Phase I MIROS Final Report)

For the RCA C70042C photomultiplier $I_D = 6 \times 10^{-10}$ amps and ηP_b is very much greater than ηP_m or I_D. Equation (1) reduces to

$$S/N = \frac{\eta P_m}{\sqrt{2e\eta P_b \Delta f}}$$

which for a 20 kc information bandwidth and the system parameters shown above gives:

$$S/N = 4.3 = 12.7 \text{ db.} \tag{2}$$

This increase over the value previously computed in Phase I results from a decrease in the spectral filter bandwidth from 100 to 5 Angstroms and a corresponding adjustment of the optical efficiency (filter transmission). This increases the maximum range, corresponding to a 0 db S/N, to approximately

$$R_2 = R_1 \sqrt{S/N}$$

$$= (1000) \sqrt{4.3} \approx 2000 \text{ km.}$$

Component Description

The receiver consists of a photomultiplier, a preamplifier, and an automatic gain control circuit arranged as shown in Figure 32. Components are designed to operate with the above parameters to provide a maximum operating range greater than 1000 km under worst background conditions. Dynamic range of the electronics is approximately 10^3 to provide a nominal operating range up to 1000 km with a constant output voltage of 1 volt. The receiver is noise-in-signal (background) limited and any reduction in the specified background conditions will be accompanied by an increase in system operating range.

Photomultiplier

The photodetector used is an RCA C70042 photomultiplier. This is a small, head-on, 3/4 inch, 10 stage tube which has a maximum length of 3.7 inches. It has an S20 photocathode which provides a usable spectral range from approximately 3000 to 7000 Angstroms as shown in Figure 33. This photomultiplier may be procured to a MIL-E-5272C environmental specification which should be adequate for withstanding the launch conditions associated with a Thor-Delta launch vehicle.
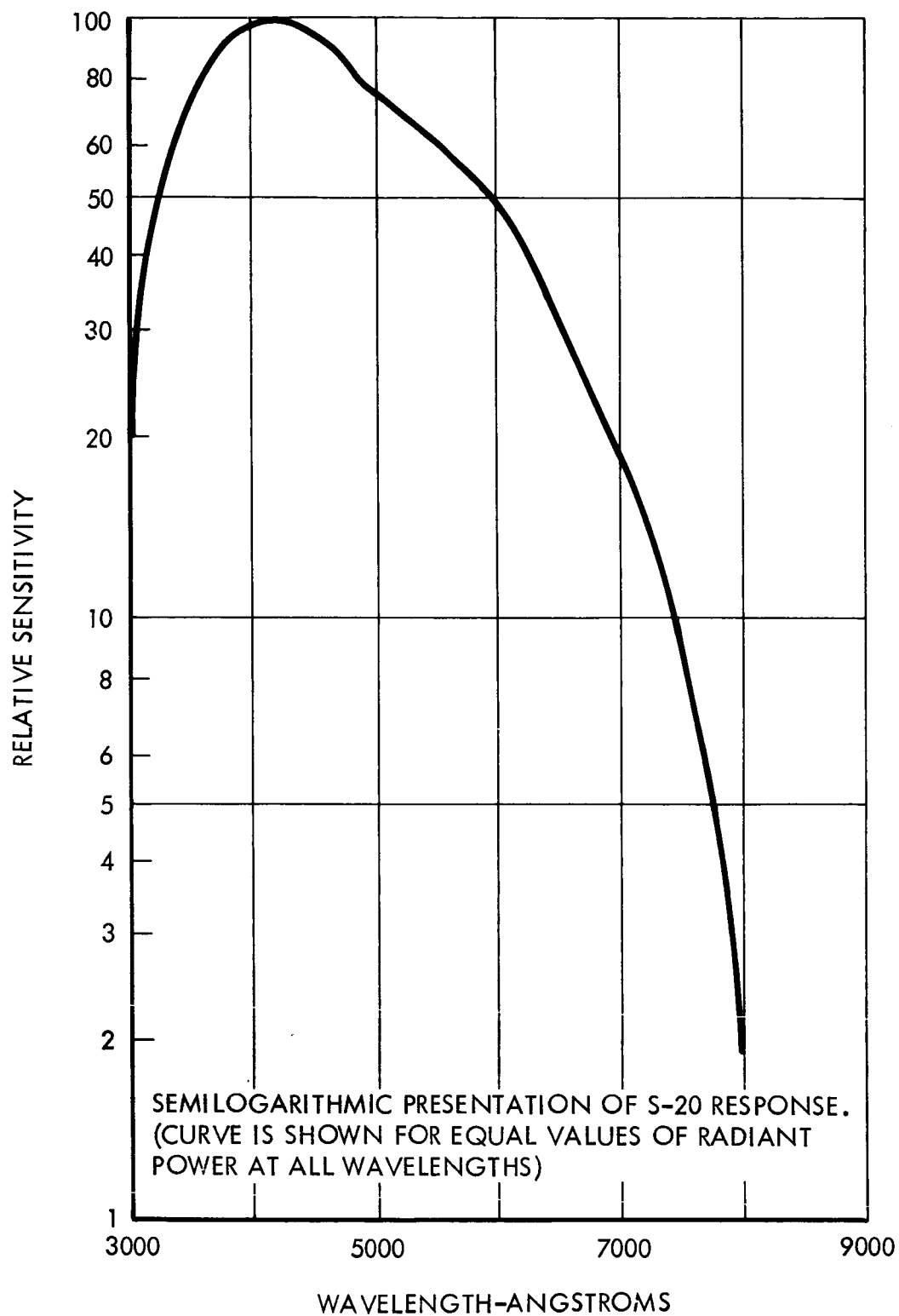
Figure 33.   Photomultiplier Spectral Sensitivity Characteristics

SID 65-1026

Choice of the photodetector and its operating configuration was determined by the input signal and background levels. As shown above these are:

$$P_b = 3.78 \times 10^{-5} \text{ watts}$$

$$P_m = 1.29 \times 10^{-8} \text{ watts}$$

which correspond to photocathode currents of

$$i_b = 9.85 \times 10^{-7} \text{ amps}$$

$$i_m = 3.35 \times 10^{-10} \text{ amps.}$$

The corresponding noise in the background current for the 20 kc bandwidth is

$$i_{b_n} = \sqrt{2 e i_b \Delta f} = 7.95 \times 10^{-11} \text{ amps}$$

and the S/N at the preamplifier input is

$$S/N = \frac{i_{b_m}}{i_{b_n}} = \frac{3.35 \times 10^{-10}}{7.95 \times 10^{-11}} = 4.3$$

Two possible design approaches were considered for the photodetector. These were: (1) use of a vacuum photodiode (S20), and (2) use of a C70042C photomultiplier connected as a photodiode or connected to provide a small amount of current amplification.

Both approaches will work for the specified system parameters; however, there are several practical advantages associated with the photomultiplier. These include:

1. S20 photomultipliers such as the RCA-C70042 are readily available at reasonable cost. S20 vacuum photodiode, however, would require a special procurement, higher cost, and a long lead time.

2. For the system parameters used, the output level from a photodiode is only slightly higher than the equivalent input noise level of the preamplifier. The use of a photomultiplier with two stages of gain will provide an operating level well above preamplifier noise but still within a safe operating current range for the tube.

3. Additional operational capability is available if desired for future applications. For example, the range available when operating against low backgrounds may be increased by using additional dynodes, increasing the photomultiplier current gain.

The operating configuration and design parameters for the photomultiplier are shown in Figure 34. For the RCA C70042C with a nominal total current gain of 10^5 the gain per stage is approximately 3.16, and for the connection shown total current gain will be approximately 10.

Preamplifier

The preamplifier is a low-noise current amplifier that has an equivalent noise input current of 5×10^{-10} amps and a bandwidth of 20 kc. Complementary low-noise 2N2586 and 2N2604 transistors are used in three direct-coupled stages with a low output impedance supplied by an emitter follower. The total amplifier has a gain of approximately 0.25 volts per microamp, and a dynamic range of greater than 10^3, which permits operation with an input current level of 0.34×10^{-4} to 0.34 to 10^{-1} microamps. This provides for a maximum operating voltage range of 0.83 to 830 millivolts at the input to the AGC amplifier.

Automatic Gain Control Amplifier

Output from the preamplifier is amplified by the AGC amplifier (Figure 35) to provide an output signal of 1 ±0.1 volt over the 100:1 dynamic range of system input levels corresponding to ranges of 100 to 1000 km.

The variable attenuator uses a pair of IN689 diodes as variable impedance elements in an L pad to provide the required attenuator characteristics. The impedance of these diodes varies with the diode current when biased in the forward direction as shown in Figure 36.

The AGC amplifier has a gain of 1250 and a bandwidth of 20 kc. To provide control current to the variable attenuator diodes, the output of this amplifier is detected, filtered, and amplified in the feedback loop. The time constant of the gain control loop is approximately 1 second, which is easily changed by an appropriate choice of low-pass filter characteristics.

The measured gain characteristic of an AGC amplifier of this type is shown in Figure 37, which indicates the threshold operating point and dynamic range for the design values stated previously.

Receiver output is obtained from an emitter follower amplifier which provides a low output impedance suitable for driving an optical retromodulator, rf modulator, recorder, or other electronic circuits.
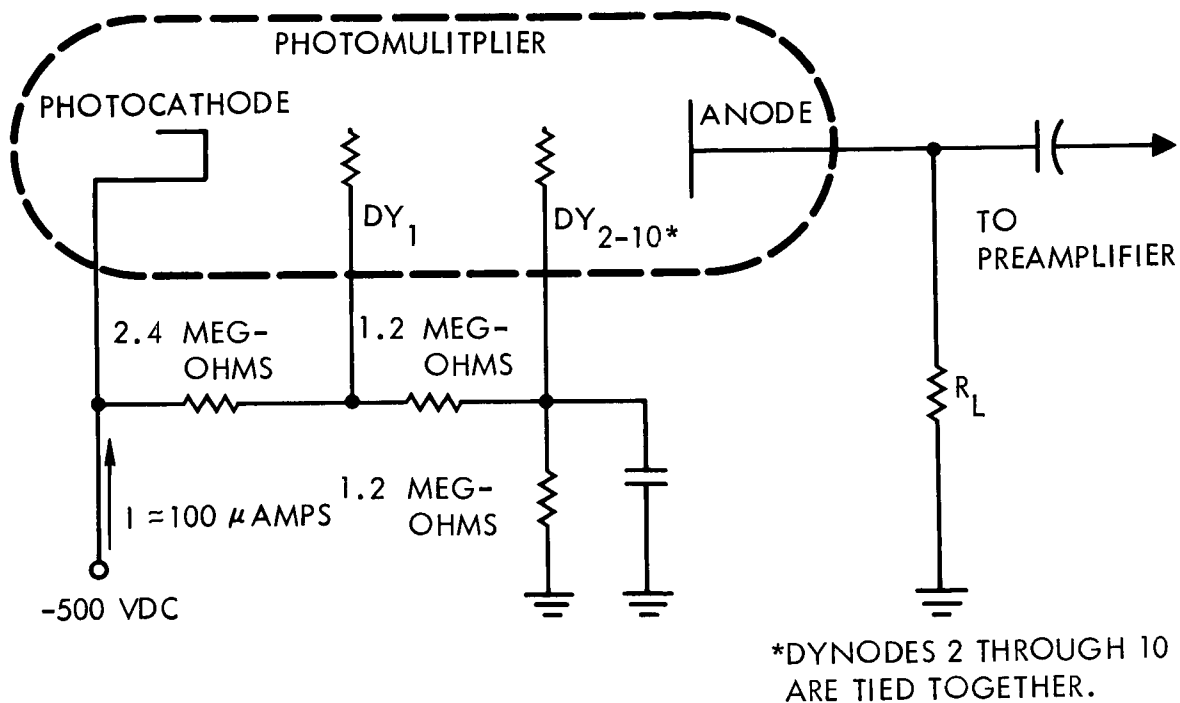
Figure 34. Photomultiplier Circuit
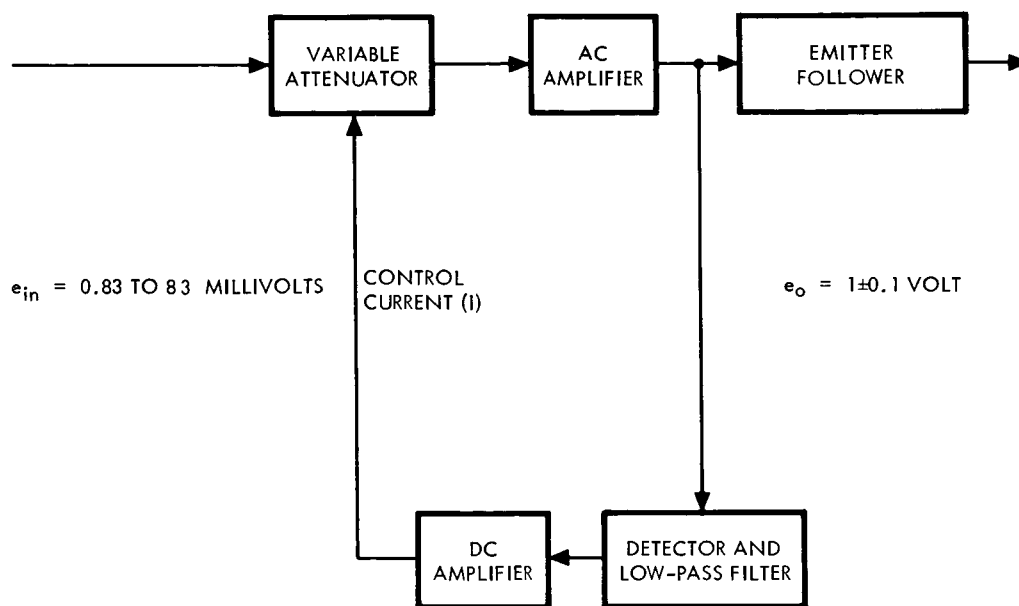
Figure 35. Automatic Gain Control Amplifier

Inside the figure:

VARIABLE ATTENUATOR → AC AMPLIFIER → EMITTER FOLLOWER

e_{in} = 0.83 TO 83 MILLIVOLTS

CONTROL CURRENT (I)

e_o = 1±0.1 VOLT

DC AMPLIFIER ← DETECTOR AND LOW-PASS FILTER

RETROMODULATOR DRIVER

The retromodulator driver has an output voltage of 0 to 25 volts
(rms) superimposed on a dc bias which is adjustable over a 100-volt
range. The input requirements are 0 to 1 volt (rms) into a 500-kilohm
input impedance, and the frequency response is flat (±1 db) over the
range of 300 cps to more than 20 kc when loaded with the MIROS retro-
modulator that electrically looks like a 0.0039 μf capacitor. This
retromodulator is composed of a maximum of 39 modulators connected
in parallel, each modulator having a capacity of approximately 100 μμf.
All characteristics were chosen to provide maximum flexibility of
operation with external input sources.

Circuitry for the amplifier consists of a class AB, push-pull,
output stage preceded by a phase-splitter and three amplifier stages.
A special output transformer drives a 1 kilohm resistive load in parallel
with the retromodulator at 25 volts (rms) output with high efficiency.
In addition, a feedback loop provides gain stabilization, reduces distor-
tion, and increases the effective amplifier bandwidth. The driver
amplifier has a closed-loop gain of 25; an open-loop gain of 1000 (60 db);
and a feedback ratio, β, of 0.04. Any slight distortion resulting from
the class AB operation is reduced by a factor of 40.

Figure 36. AC Impedance Characteristics of a IN689 Diode

SID 65-1026

Figure 37. AGC Amplifier Measured Gain Characteristics

SID 65-1026

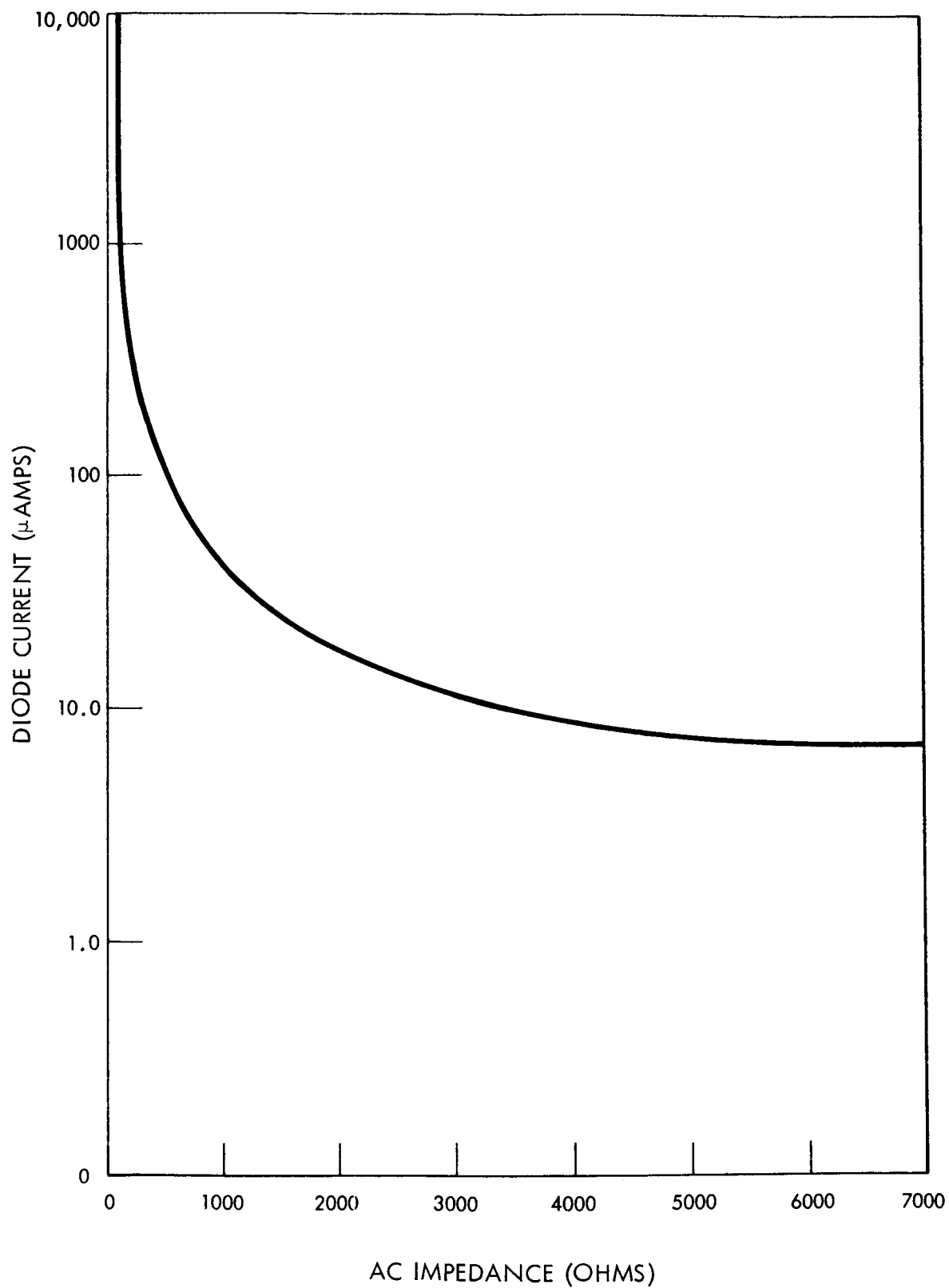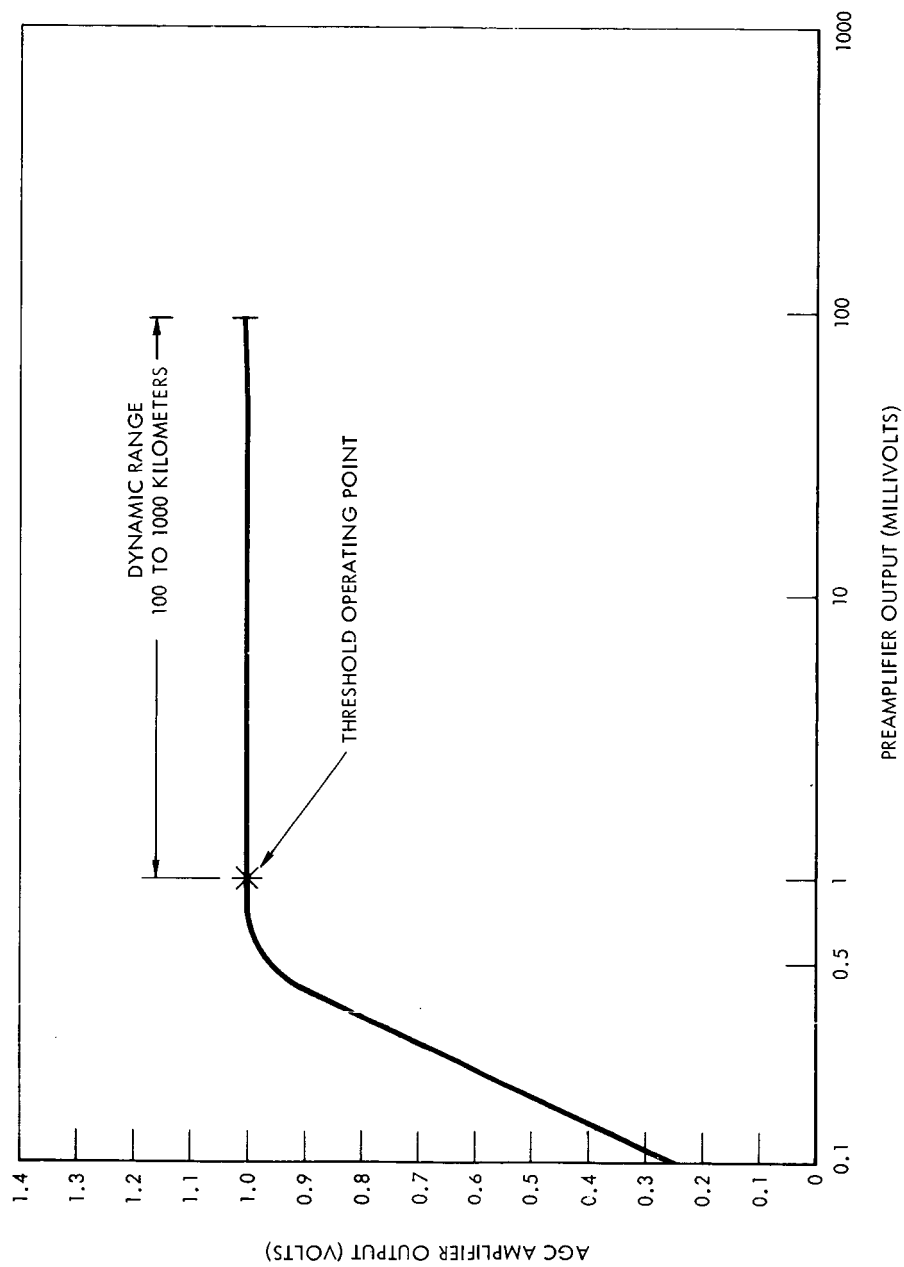Retromodulator bias is obtained from the power supply and coupled through the transformer secondary. Power requirements for the retro-modulator driver are approximately 720 milliwatts at maximum signal output and 270 milliwatts with zero signal input.

Power Supply

All power required for the MIROS unit is obtained from a 28-volt source, which is used directly to supply the modulator driver and receiver with suitable decoupling and filtering (Figure 32).

A fixed 500-volt bias for the receiver photomultiplier is obtained from a dc-to-dc converter. This circuit supplies a filtered, 500-volt output, which is also used to provide the adjustable modulator bias, as shown in Figure 32. For an expected efficiency of 35 percent, the total power required is 570 milliwatts.

The total power requirements for the system are presented in the following listing.

Receiver	Power Requirements (milliwatts)
Photomultiplier	(included in HV power supply)
Preamplifier	100
AGC amplifier	140
Modulator (maximum output)	720
HV Power supply	570
Total	1,530

Redesign for Space Application

Modification of the present design to give optimum performance in space for a specific vehicle, mission, and orientation cannot be precisely described until the actual parameters are known. However, a few gener-alities can be assumed that will allow a description of the probable trend the modification will take. If it is assumed that the instrument will never see the sun, a sun shutter to protect the photomultiplier tube is not needed. It is assumed that the method of attachment is to the outer skin of the vehicle and that microcircuits will be available with the required

reliability and economy. Based on these generalities, a configuration similar to that shown in Figure 38 is possible.

As explained earlier, this redesign would be almost entirely a replacement of mechanical structural members since the costly parts — the retromodulator, window, components of the optical receiver, and electronics — already exist. They need only be assembled into the new strucure. The retromodulator is roughly pyramidal in shape with the window at its base. The optical receiver, except for its electronics, is essentially a small cylinder. If the electronics are miniaturized using microcircuits, they can be placed nearly anywhere there is a small volume available. It is possible, then, that the configuration will be made up of a cone with a small cylinder alongside, as depicted in Figure 38. A lightweight, simple casting should replace about three-quarters of the structural parts now required. Three simple vacuum seals may be all that are required: one for the electrical leads, one for the housing, and one would be the vacuum pinch-off tubulation. The weight would probably reduce to between 12 and 15 pounds.

COMPARISON OF RETRODIRECTIVE MODULATION DEVICES

Two significantly different device concepts have been considered for achieving retrodirective optical modulation. In the MIROS concept, a corner reflector made of three mutually perpendicular mirrors is used to achieve retrodirection. One of the mirrors is made up of an array of electrostatically deformable membrane modulators of the type discussed extensively in this document. In the spherical MIROS (SMIROS) concept, a spherical optical system of the Maksutov type is used to focus light on a (spherical) reflection focal plane. A piezoelectric disc driven in a thickness expansion mode is used either to move the reflecting surface in and out of the focal plane or as part of a variable spacing and, therefore, variable reflectance Fabrey-Perot interferometer. In either mode, the motion of the piezoelectric produces modulation.

A comparative analysis of the two concepts was completed based on voltage and power requirements only. (Weight and reliability consider-ations have not been included since their inclusion would have called for detailed design and testing of near optimumly designed units of both types.) We have found that the voltage and power requirements depend on the area of the modulation element, on the modulation bandwidth it is designed for, and on the depth of modulation. These relationships are developed in Appendix V. In comparing the performance of a piezoelec-tric and a membrane modulator operating over the same bandwidth and depth of modulation and with the same area, it is shown that the piezo-electric element will require almost three times the voltage and about twenty times the power needed by the membrane modulator. It is
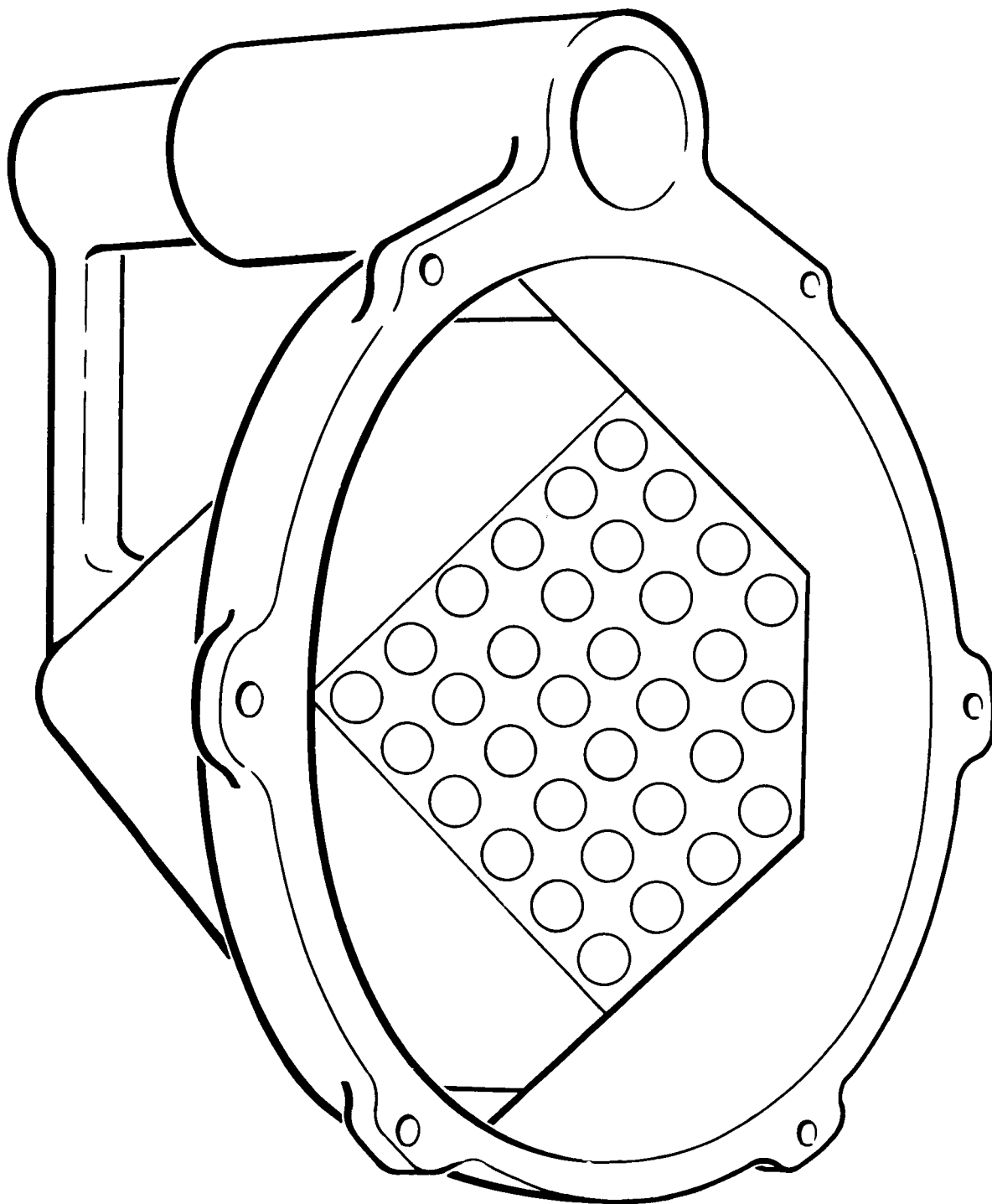
Figure 38.   MIROS Package Concept (Space Vehicle)

interesting to note that the depth of modulation, although related to the mechanical motion of the device in different ways for each of the three methods of achieving modulation, is almost the same value for equal amounts of mechanical motion. This assumes reasonable constraints on system design. For the MIROS membrane modulator, a sagittal displacement between $\lambda/8$ and $3\lambda/8$ will result in almost 75 percent depth of modulation. In the SMIROS system based on moving the reflective surface in and out of the focal plane, the depth of modulation depends on the "speed" of the optical system. For an f/1 system, measuring displacement relative to the Gaussian focal plane, displacements between $\lambda/8$ and $3\lambda/8$ will also produce almost 75 percent depth of modulation. (For an f/2 system, four times as much displacement will be required for the same depth of modulation.) For the SMIROS system, based on a variable reflectance Fabrey-Perot interferometer with a finite depth of focus, the "speed" of the optical system limits the reflectivity of the mirrors in the interferometer and, thus, the sensitivity of the interferometer. For a fast optical system, i.e., f/1, approximately the same motion is required as for the two above systems. (Practical considerations concerning maintaining alignment also limit the useful sensitivity of the Fabrey-Perot interferometer.) We may thus conclude that a reasonably designed system of any of the three types will require about $\lambda/4$ displacement for 75 percent depth of modulation.

The required area of the modulation element in the SMIROS concept depends on the collection area of the system, the solid angle over which the system operates, and the effective speed of the optical system. The faster the optical system, the smaller the required area. The required area of the modulation elements in the MIROS concept depends only on the collection area of the corner reflector. Introducing the solid angle over which the corner reflector is retrodirective, it is seen that the area of modulator elements required by MIROS is equivalent to the area of modulator elements in a SMIROS system with a speed of f/0.9, for the same collection area and solid angle. These results are derived in Appendix VI.

It can thus be seen that if a large field of view is required, the MIROS device can operate with less voltage and significantly less power than a SMIROS unit designed with the same collection area, bandwidth, and field of view. (This assumes optical systems significantly faster than f/0.9 are not possible.) If, on the other hand, the solid angle over which the retrodirective device has to operate is less than that of a cone with 25-degree half-angle, it is possible to tailor a SMIROS device to work only in a small field of view and thereby reduce the required area of the modulator element and, thus, the power and voltage. This reduction is not possible with a MIROS device. The final choice between SMIROS and MIROS, to the extent that it depends only on power and voltage requirements, must be based on detailed considerations of the mission.

APPENDIX I

PRESSURIZED MEMBRANE MODULATOR
PERFORMANCE ANALYSIS

SUBRESONANT MEMBRANE SHAPE

A stretched, circular, aluminized membrane forms the top of a cylinder, with diameter D and depth d, which contains a gas under pressure. When a driving voltage is applied between the membrane and base of the cylinder, the membrane is displaced by the electrostatic force. An expression will be developed in the following paragraphs giving the displacement of the membrane at any point as a function of membrane tension, the pressure of the enclosed gas, and the applied electrostatic force (driving voltage).

The displacement of the membrane normal to the x-y plane is given as U (x, y). The tensile forces acting on the sides of the elemental area, dx dy, of the membrane are T dx and T dy (see Figure I-1). By analogy with the vibrating string derivation, the net tension in the direction normal to the x-y plane resulting from forces T dx and -T dx is

$$(T \ dx) \ \frac{\partial^2 U}{\partial y^2} \ dy. \tag{1}$$

Similarly, the normal tension resulting from T dy and -T dy is

$$(T \ dy) \ \frac{\partial^2 U}{\partial x^2} \ dx. \tag{2}$$

Equations 1 and 2 hold for small membrane displacements.

Equating the sum of tensional forces plus the force on the membrane due to pressurization, P (U) dx dy, and the electrostatic force, F_e dx dy, to the membrane mass times acceleration, $(\rho \ dx \ dy) \frac{\partial^2 U}{\partial t^2}$, results in

$$T \ dx \ dy \ \frac{\partial^2 U}{\partial x^2} + T \ dx \ dy \ \frac{\partial^2 U}{\partial y^2} + P(U) \ dx \ dy + F_e \ dx \ dy$$

$$= \rho \ dx \ dy \ \frac{\partial^2 U}{\partial t^2}. \tag{3}$$

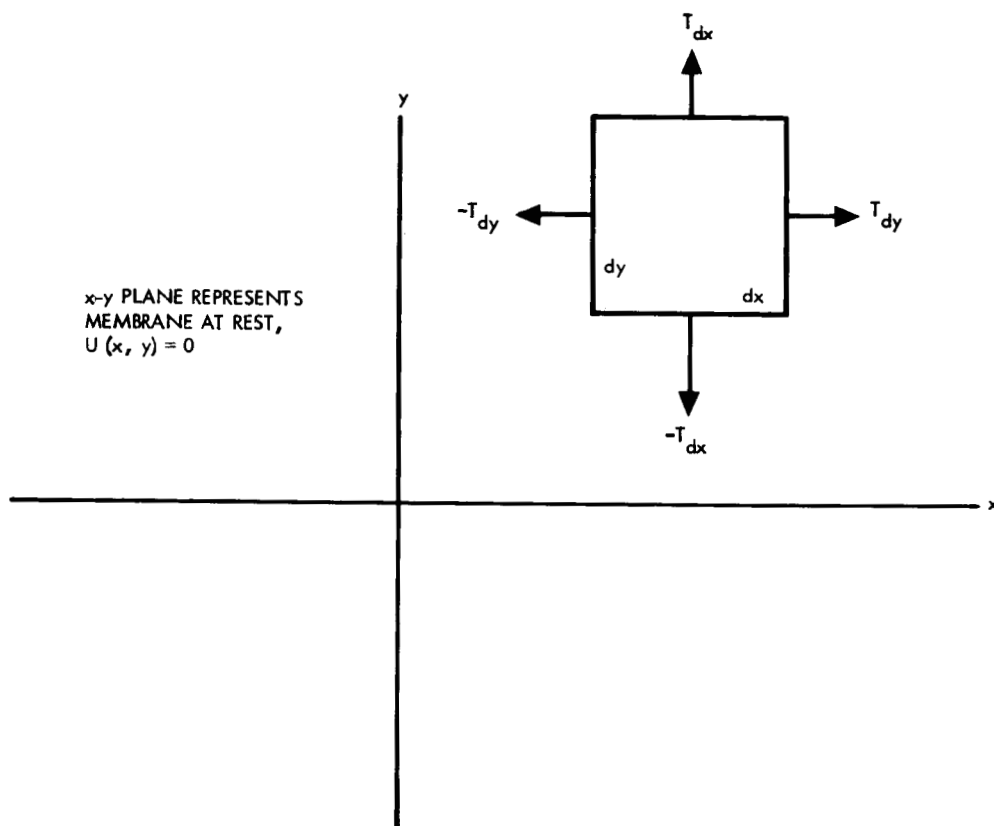(It is assumed that sonic propagation effects in the gas are negligible.)

Figure I-1. Tensile Forces Acting on the Side of Elemental Area

Consequently, P(U) is a functional expression relating the pressure on the membrane to an integral of its displacement function, U. Therefore, P(U) is not a function of x and y but of the functional form of U.

Dividing through by T dx dy, the equation becomes

$$\frac{\partial^2 U}{\partial x^2} + \frac{\partial^2 U}{\partial y^2} + \frac{P(U) + F_e}{T} = \frac{\rho}{T} \frac{\partial^2 U}{\partial t^2}. \tag{4}$$

The solution of this second-order linear partial differential equation describes the membrane's displacement at any point, and hence is a general description of the membrane's shape. Here the main concern is with the membrane's shape when it is driven below its resonant frequency. Equation 4 will now be solved for the case of subresonance. Mathematically, this is expressed by setting $\frac{\rho}{T} \frac{\partial^2 U}{\partial t^2} = 0$. Hence,

$$\frac{\partial^2 U}{\partial x^2} + \frac{\partial^2 U}{\partial y^2} = - \frac{P(U) + F_e}{T}. \tag{5}$$

The solution of this equation yields

$$U(x, y) = \left[\frac{F_e + P(U)}{4T}\right] \left[\left(\frac{D}{2}\right)^2 - (x^2 + y^2)\right]. \tag{6}$$

This solution is of the form $Z = K \left[\left(\frac{D}{2}\right)^2 - (x^2 + y^2)\right]$, which is the equation of a spherical paraboloid. Thus, the shape of the membrane below resonance is a spherical paraboloid (paraboloid of revolution).

The membrane sagitta per unit radius, $\frac{U}{S}$, as a function of electrostatic force (driving voltage) can be obtained from Equation 6 as follows:

$$\frac{U}{S} = \frac{F_e + P(U)}{4T} \tag{7}$$

where

$$S = \left(\frac{D}{2}\right)^2 - (x^2 + y^2).$$

I-3

MAGNITUDE OF DRIVING VOLTAGE

The membrane modulator will have a broad modulation bandwidth. This bandwidth can be conceptually achieved either by pressurization of the system or by an increase in the tension applied to the membrane. Assuming these approaches are equally feasible for any resonant frequency, i.e., that T could be made as large as desired, the question arises as to how will the choice of approach vary the magnitude of the applied driving voltage.

Before this question can be answered directly, $P(U)$ must be expressed in terms of the system parameters and the resulting expression substituted into Equation 7. $P(U)$ can be written as

$$P(U) = \beta \int_{membrane} U(x, y) \, dx \, dy \qquad (8)$$

Where β, the pressurization, is equal to the cylinder gas pressure divided by its volume, P/V. The membrane deflection must be small compared to d or $\dfrac{U}{S} \left(\dfrac{D}{2}\right)^2 << d$. $P(U)$ expressed in polar coordinate form for computation purposes is

$$P(U) = \beta \int_{o}^{2\pi} d\theta \int_{o}^{\frac{D}{2}} \left[\frac{F_e + P(U)}{4T}\right]\left[\left(\frac{D}{2}\right)^2 - r^2\right] r \, dr \qquad (9)$$

$$= \pi\beta \left(\frac{F_e + P(U)}{2T}\right) \frac{\left(\frac{D}{2}\right)^4}{2} - \frac{\left(\frac{D}{2}\right)^4}{4}$$

$$= \pi\beta \left(\frac{F_e + P(U)}{2T}\right) \frac{\left(\frac{D}{2}\right)^4}{4} .$$

Therefore,

$$P(U) = \frac{\pi\left(\frac{D}{2}\right)^4 \beta F_e}{8T} \Bigg/ \left(1 - \frac{\pi\left(\frac{D}{2}\right)^4 \beta}{8T}\right). \qquad (10)$$

Substituting Equation 10 into Equation 7 and rearranging the terms gives

$$\frac{U}{S} = \frac{F_e}{4} \left[\frac{1}{T - \frac{\pi \left(\frac{D}{2}\right)^4 \beta}{8}} \right].$$ (11)

Note that the membrane sagitta varies linearly with the electrostatic force in all cases. β has been defined in terms of pressure; however, by making use of the angular resonant frequency expression of the pressurized system, pressure can be eliminated.

From the Final Report on Project MIROS—Phase I (SID 65-117), page 57,

$$\omega^2 - \omega_o^2 = \frac{\alpha p}{\rho d}$$ (11A)

where ω is the resonant frequency achieved with tension and pressurization, and ω_o is the resonant frequency which would be obtained if there were no pressurization. α is a factor approximately equal to 2/5. Thus,

$$\beta = \frac{p}{V} = \frac{4p}{\pi D^2 d}$$ (12)

$$p = \frac{(\omega^2 - \omega_o^2) \rho d}{\alpha}.$$ (13)

Therefore,

$$\beta = \frac{4 (\omega^2 - \omega_o^2) \rho d}{\pi D^2 d \alpha} = \frac{4 \rho (\omega^2 - \omega_o^2)}{\pi D^2 \alpha}.$$ (14)

At this point it is possible to directly evaluate the voltage requirements for either the pressurized or tensional case.

Pressurized Case

In this approach, the membrane tension, T, is considered to be zero. Hence, ω_o equals zero $\left(\omega_o = \frac{4.8}{D} \sqrt{\frac{T}{\rho}} \right)$. (14A)

I-5

Ω will be used to represent the resonant angular frequency of the system. Therefore, β is expressed as

$$\beta = \frac{4\rho\,\Omega^2}{\pi D^2 \alpha} \; .$$ (15)

Substituting this expression into Equation 11 gives

$$\frac{U}{S} = F_e \left[\frac{2\alpha\,\pi D^2}{\pi \left(\dfrac{D}{2}\right)^4 4\rho\Omega^2} \right]$$ (16)

rewritten as

$$\frac{U}{S} = \frac{8\alpha}{\rho} F_e \left(\frac{1}{D\Omega}\right)^2 \; .$$ (17)

This expression gives the electrostatic force (driving voltage) required to achieve a given sagitta for a given angular frequency (bandwidth), Ω.

Tensional Case

In this approach, an unpressurized system is assumed. Hence, $\beta = 0$. Again, the resonant angular frequency of the system is represented by Ω. The membrane tension, T, is given by

$$T = \left(\frac{\Omega D}{4.8}\right)^2 \rho$$ (18)

therefore,

$$\frac{U}{S} = F_e \left[\frac{(4.8)^2}{4\Omega^2 D^2 \rho} \right]$$ (19)

$$\frac{U}{S} = \frac{5.76}{\rho} F_e \left(\frac{1}{\Omega D}\right)^2 \; .$$ (20)

Comparing this result with that of the pressurized case shows that for a given angular frequency, Ω, the driving voltage required is approximately the same in both cases. This is a very important result for it states that the driving voltage required for a given resonant frequency is independent of the approach (pressurization or tensional) used for obtaining that resonant frequency.

SID 65-1026

BREAKDOWN VOLTAGE

The magnitude of the driving voltage required for a given resonant frequency (modulation bandwidth) is limited by the dielectric material and the modulator gap size. The minimum gap size required to obtain a given modulation bandwidth without exceeding the modulator breakdown voltage will now be considered.

As shown in the Final Report on Project MIROS – Phase I, Section 1, page 20, the membrane sagitta, Δ, is related to the applied voltage by the following relationship

$$\Delta = \frac{\epsilon_o D^2}{32\,T} \left(\frac{V}{d}\right)^2 \tag{21}$$

T represents the membrane tension (force per unit length); D, the membrane diameter; ϵ_o, the permittivity of free space; d, the gap size; and V, the driving voltage. (MKS system of units.) Also expressed in the report mentioned previously is the angular frequency expression for the unpressurized system (resonant frequency achieved by tension only). Namely,

$$\omega_o = \frac{4.8}{D} \sqrt{\frac{T}{\rho}} \tag{22}$$

rewritten as

$$T = \frac{\rho \omega_o^2 D^2}{(4.8)^2} \cdot \tag{23}$$

Substituting Equation 23 into Equation 21 gives

$$\Delta = \frac{\epsilon_o D^2 (4.8)^2}{32\,\rho\,\omega_o^2\,D^2} \left(\frac{V}{d}\right)^2 \tag{24}$$

which when rewritten to solve for $\left(\dfrac{V}{d}\right)^2$ becomes

$$\left(\frac{V}{d}\right)^2 = \frac{32\,\rho\,\omega^2\,\Delta}{\epsilon_o (4.8)^2} \cdot \tag{25}$$

ω_o^2 is changed to ω^2 in Equation 25 with the understanding that the result now applies for pressurized as well as unpressurized systems.

The reason is that for a given resonant frequency $\frac{V}{d}$ is the same whether that frequency was achieved by pressurization or tension. ω^2 represents the system angular resonant frequency.

The modulator breakdown electric field, voltage divided by gap size, for a dielectric at 25 degrees centigrade is

$$\left(\frac{V}{d}\right)_B = 30 \times 10^5 \gamma \left(\frac{p}{p_o}\right) \frac{volts}{meter} \tag{26}$$

for p greater than 1 mm of Hg.

γ is a constant characteristic of the dielectric (gas used), and its value for air is unity. $\frac{p}{p_o}$ is the ratio of the modulator chamber pressure to standard sea-level pressure. By using the resonance expression for the pressurized system (assuming that the systems concerned are those whose resonant frequencies are much larger than the tension's resonant frequency, ω_o),

$$p = \frac{\omega^2 \rho d}{\alpha} \tag{27}$$

p can be eliminated from Equation 26

$$\left(\frac{V}{d}\right)_B = \frac{30 \times 10^5}{p_o} \gamma \left(\frac{\omega^2 d\rho}{\alpha}\right). \tag{28}$$

For a breakdown not to occur,

$$\left(\frac{V}{d}\right)_B > \left(\frac{V}{d}\right). \tag{29}$$

Hence,

$$\frac{30 \times 10^5 \gamma}{p_o} \left(\frac{\omega^2 d\rho}{\alpha}\right) > \left(\frac{32\rho \omega^2 \Delta}{\epsilon_o (4.8)^2}\right)^{1/2}. \tag{30}$$

Squaring both sides,

$$\frac{9 \times 10^{12} \gamma^2}{\alpha^2 p_o^2} \left(\omega^4 d^2 \rho^2\right) > \frac{32\rho \omega^2 \Delta}{\epsilon_o (4.8)^2}. \tag{31}$$

I-8

Rearranging terms yields

$$\frac{\epsilon_o \gamma^2}{\alpha^2 p_o^2} \frac{9 \times 10^{12} \times 25}{32} > \frac{\Delta}{\omega^2 d \rho} .$$ (32)

Solving for $\omega^2 d$,

$$\omega^2 d > \frac{32 \Delta \alpha^2 p_o^2}{9 \times 25 \times 10^{12} \epsilon_o \gamma^2 \rho} .$$ (33)

Letting $\epsilon_o = 8.85 \times 10^{-12} \frac{\text{farad}}{\text{meter}}$

$\alpha = 2/5$

$\gamma = 1$ (air)

$\Delta = 6.3 \times 10^{-7}$ meters

$p_o = 1.01 \times 10^5$ newtons per meter^2

$\rho = \rho't$, where $\rho' = 1.3 \times 10^3$ kilograms per meter^3 and $t = 6.3 \times 10^{-6}$ meters,

$$\omega^2 d > 2 \times 10^3 \text{ meters per second}^2 .$$

Thus for a given resonant frequency, the gap size, d, must be made large enough so that the relationship of Equation 33 is satisfied. Note that if a pressurization is safe (i.e., one in which the required voltage can be applied without breakdown), then increasing the pressure, thus raising the resonant frequency and the required voltage, will never lead to an unsafe condition (i.e., one in which the required voltage exceeds breakdown).

NOMENCLATURE

α Average displacement of the membrane for unit displacement of membrane center

β Cylinder gas pressure divided by its volume

γ Constant; characteristic of the dielectric (gas used)

Δ Membrane sagitta due to applied voltage

ϵ_o Permittivity of free space

ρ Area density of the membrane

Ω Resonant angular frequency of a system achieved by tension or pressurization only

ω Angular resonant frequency of the pressurized system

ω_o Angular resonant frequency of the unpressurized system

d Depth of cylinder (distance from the capping membrane to the bottom of the cylinder)

D Diameter of cylinder

f Frequency in cycles per second of the pressurized system

F_e Electrostatic force per unit area

f_o Frequency in cycles per second of the unpressurized system

p Cylinder gas pressure

$\dfrac{p}{P_o}$ Ratio of modulator chamber pressure to standard sea-level pressure

$P(U)$ Functional expression relating the pressure on the membrane, P, to an integral of its displacement function, U

T Tensile force per unit length (tension)

U (x, y)   Displacement of the membrane normal to the nominal plane

$\dfrac{U}{S}$ Membrane sagitta per unit radius

V   Applied membrane driving voltage

$\left(\dfrac{V}{d}\right)_B$ Modulator breakdown electric field

APPENDIX II

SPECIFICATIONS AND ANALYSIS OF THE OPTICAL ASPECTS OF MIROS LABORATORY MEASUREMENTS

LABORATORY MEASUREMENT AND SPACE SITUATION MEMBRANE RELATIONSHIP

Figure II-1 shows the light source wave front plane (associated with the collimated beam after reflection by the membrane and immediately after passing through the imaging lens) and the image plane, separated by a distance, R, which is equal to the focal length of the lens. Applying the Kirchoff-Fresnel theory[9] to this situation yields

$$u\,(\vec{x}) = \alpha \int_{\substack{\vec{v} \\ \text{plane}}} U\,(\vec{v})\; \frac{\exp\, ik\,(\vec{v},\vec{x})}{(\vec{v},\vec{x})}\,(1 + \cos\theta)\; d\vec{v} \tag{1}$$

for the image electric vector at $\vec{x}$. The complex constant, α, contains all the terms which do not directly enter into the integration. θ is the inclination angle, and $(\vec{v},\vec{x})$ is the distance from the point $\vec{v}$ to the point $\vec{x}$ of the image. Specifically,

$$(\vec{v},\vec{x}) = \sqrt{(\vec{v}-\vec{x})^2 + R^2}. \tag{2}$$

Expanding in series form gives

$$(\vec{v},\vec{x}) = \sqrt{R^2 + v^2 + x^2 - 2\,\vec{v}\cdot\vec{x}}$$

$$= R\,\sqrt{1 + \frac{v^2}{R^2} + \frac{x^2}{R^2} - \frac{2\vec{v}\cdot\vec{x}}{R^2}}$$

$$\simeq R\,\left\{1 + \frac{v^2}{2R^2} + \frac{x^2}{2R^2} - \frac{\vec{v}\cdot\vec{x}}{R^2}\right\}. \tag{3}$$

9
  Born and Wolf. Principals of Optics. New York: Pergamon Press (1959), pp 379.

SID 65-1026

WAVE FRONT PLANE
OF THE LIGHT BEAM
IMMEDIATELY AFTER
PASSING THROUGH
THE IMAGING LENS

$\left(\overrightarrow{v}, \overrightarrow{x} \right)$

θ

$\overrightarrow{v}$

$\overrightarrow{x}$
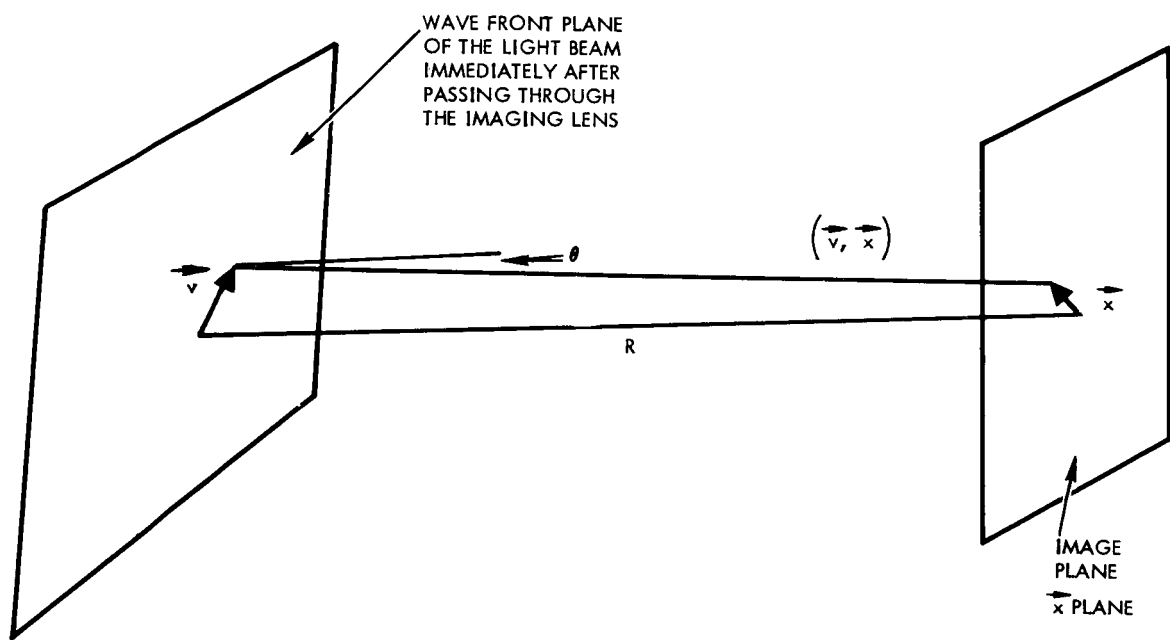
R

IMAGE
PLANE

$\overrightarrow{x}$ PLANE

Figure II-1.   Wave Front Plane and Image Plane

Therefore,

$$u(\vec{x}) = \alpha \int d\vec{v}\, U(\vec{v}) \exp i\,k\,R \frac{\left\{1 + \dfrac{v^2}{2R^2} + \dfrac{x^2}{2R^2} - \dfrac{\vec{v}\cdot\vec{x}}{R^2}\right\}(1+\cos\theta)}{R\left\{1 + \dfrac{v^2}{2R^2} + \dfrac{x^2}{2R^2} - \dfrac{\vec{v}\cdot\vec{x}}{R^2}\right\}}. \quad (4)$$

Since $\dfrac{v^2}{R^2}$, $\dfrac{x^2}{R^2}$, and $\dfrac{\vec{v}\cdot\vec{x}}{R^2}$ are much less than unity, these higher order terms may be dropped from the R expansion in the denominator. Furthermore, $(1+\cos\theta)$ is a constant and can be brought outside the integral and combined with α to form a new constant, δ.

$$u(\vec{x}) = \delta \int U(\vec{v})\,\frac{\exp i\,k\,R}{R}\left\{1 + \frac{v^2}{2R^2} + \frac{x^2}{2R^2} - \frac{\vec{v}\cdot\vec{x}}{R^2}\right\} d\vec{v}. \quad (5)$$

$U(\vec{v})$ represents the planar wave front deviation from flatness due to the imaging lens, membrane aberrations, and membrane movement (modulation). The membrane aberration and modulation are represented by $\exp i\,\emptyset_{ab}(\vec{v})$ and $\exp i\,\emptyset_{mod}(\vec{v})$, respectively. The deviations introduced by the lens can be derived by considering the lens envelope to be spherical and using the sagitta formula. Specifically,
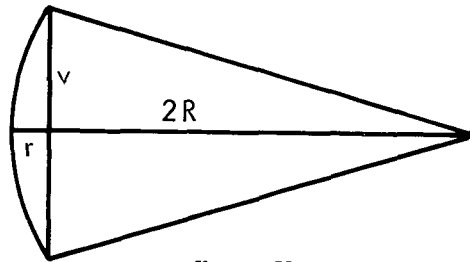
$$\frac{r}{v} = \frac{v}{2R}$$

$$r = \frac{v^2}{2R}. \quad (6)$$

Therefore, the expression of the deviation due to the lens is

$$\exp\ -\left\{\frac{i\,k\,v^2}{2R}\right\}$$

and

$$U(\vec{v}) = \exp\left\{i\,\emptyset_{ab}\,(\vec{v}) + i\,\emptyset_{mod}\,(\vec{v}) - i\,k\,\frac{v^2}{2R}\right\}\ .$$

Thus,

$$u(\vec{x}) = \delta\ \int d\vec{v}\,\exp\left\{\frac{i\,k\,v^2}{2R} + i\,\emptyset_{ab}\,(\vec{v}) + i\,\emptyset_{mod}\,(\vec{v})\right\}\ \frac{\exp}{R}\left\{i\,k\right.$$

$$\left.\left[R + \frac{v^2}{2R} + \frac{x^2}{2R} - \frac{\vec{v}\cdot\vec{x}}{R}\right]\right\}\ .\tag{7}$$

By bringing the constants outside the integral sign, they can be combined into a new constant, β .

$$u(\vec{x}) = \beta\ \int d\vec{v}\,\exp\left\{i\,k\left[\frac{x^2}{2R} - \frac{\vec{v}\cdot\vec{x}}{R}\right]\right\}\ \exp\left\{i\,\emptyset_{ab}\,(\vec{v}) + i\,\emptyset_{mod}\,(\vec{v})\right\}.$$
$$\tag{8}$$

Since $k\,x^2/2R \ll 1$ in the vicinity of the focal spot, it can be neglected. Therefore,

$$U(\vec{x}) = \beta\ \int d\vec{v}'\,\exp\left\{- i\,k\,\vec{v}\cdot\left(\frac{\vec{x}}{R}\right)\right\}\ \exp\left\{i\,\emptyset_{ab}\,(\vec{v}) + i\,\emptyset_{mod}\,(\vec{v})\right\}\ .$$
$$\tag{9}$$

When the collimated light beam is reflected from a satellite membrane, R, θ, $\vec{v}$, and $\vec{x}$ are replaced by R', θ', $\vec{v}'$, and $\vec{x}'$; the lens is removed from the problem; R' is made very large; and values of $\vec{x}'$ are considered much larger than $\vec{v}'$. The electric vector of the reflected light beam is given by

$$u(\vec{x}') = \alpha'\ \int d\vec{v}'\ U(\vec{v}')\ \frac{\exp i\,k\,(\vec{v}',\vec{x}')}{(\vec{v}',\vec{x}')}\ (1 + \cos\theta').\tag{10}$$

The term $(\vec{v}',\vec{x}')$ can be represented by

$$(\vec{v}',\vec{x}') \simeq R'\ \left(1 + \frac{v'^2}{2R'^2} + \frac{x'^2}{2R'^2} - \frac{\vec{v}'\,\vec{x}'}{R'^2}\right)\ .\tag{11}$$

This follows the same reasoning used to derive Equation 3; however, $U(v')$ in this case involves only the membrane aberration and modulation variations, $\exp i \emptyset_{ab} (\vec{v}')$ and $\exp i \emptyset_{mod} (\vec{v}')$.

θ' is small; therefore, $\cos \theta' \simeq 1$. Thus,

$$u(\vec{x}') = 2\alpha' \int d\vec{v}' \exp \left\{ i \emptyset_{ab} (\vec{v}') + i \emptyset_{mod} (\vec{v}') \right\} \frac{\exp}{R'} \left\{ i k R' \right. \tag{12}$$

$$\left. \left[1 + \frac{v'^2}{2R'^2} + \frac{x'^2}{2R'^2} - \frac{\vec{v}' \cdot \vec{x}'}{R'^2} \right] \right\} .$$

After redefining the constant β to cover the constants brought outside integral sign, and since $R' \gg 1$, the equation becomes

$$u(\vec{x}') = \beta' \int d\vec{v}' \exp \left\{ i \emptyset_{ab} (\vec{v}') + i \emptyset_{mod} (\vec{v}') \right\} \exp \left\{ -i k \vec{v}' \cdot \left(\frac{\vec{x}'}{R'} \right) \right\} . \tag{13}$$

Comparing Equations 9 and 13 reveals that both are of the same form; they differ only by a scaling constant,

$$K \left(i.e., \quad \frac{\vec{x}}{R} = K \frac{\vec{x}'}{R} \right) .$$

Therefore, the assertion is proved that measurements made in the laboratory using a lens and working in the focal plane can be directly extrapolated to space application.

APPENDIX III

TECHNIQUE FOR CONVERTING SPOT INTENSITY MEASUREMENTS TO MEMBRANE DISTORTION STATISTICS

In this experiment, collimated light is reflected from a nominally flat membrane and brought to focus by a lens. The total intensity of the image in a small circle of radius r is then determined experimentally for various values of r. The quality (flatness, reflectivity, etc.) of the flat membrane determines the image intensity. Theoretically, the value of the image intensity can be derived from the modulation transfer function as follows:

The image intensity at a point $\vec{x}$ in the image focal plane[10] is given by

$$u(\vec{x})\, u^*(\vec{x}) = \int d\vec{f}\, e^{2\pi i \vec{f} \cdot \vec{x}}\, \tau(f) \tag{1}$$

where

$$\tau(\vec{f}) = \left(\tau_{\text{ideal}}(\vec{f})\right)\left(\tau_{ab}(\vec{f})\right). \tag{2}$$

$\tau_{\text{ideal}}(f)$ is the modulation transfer function[11] for a diffraction–limited lens in the absence of wave front distortion; τ_{ab} is the modulation transfer function for an aberrated membrane when "feeding" the lens.

$$\tau_{\text{ideal}}(\vec{f}) = \frac{2}{\pi}\left\{\cos^{-1}\left(\frac{\lambda f F}{D}\right) - \left(\frac{\lambda f F}{D}\right)\sqrt{1 - \left(\frac{\lambda f F}{D}\right)^2}\right\} \tag{3}$$

$$\tau_{ab}(\vec{f}) = \exp\left\{-2\left[D_{UU}(\lambda f F)\right]\left(\frac{2\pi}{\lambda}\right)^2\right\} \tag{4}$$

where F is the focal length of the lens and F/D is the f-number.

$D_{UU}(\lambda f F)$ is the aberration structure function, i.e., the mean square elevation difference between two points on the membrane due to membrane imperfections. This is expressed mathematically as

---

[10] This expression is the repeated Fourier transform — Erdelyi, A. Bateman Manuscript Project, Tables of Integral Transforms. Vol. I, No. 1, pp. 117. McGraw-Hill (1954).

[11] f represents spatial frequency

$$D_{uu}(r) = < \left[U(\vec{x}) - U(\vec{x}') \right]^2 > \qquad (5)$$

where $r = |\vec{x} - \vec{x}'|$. $U(\vec{x})$ represents the elevation of the membrane above the nominal plane at $\vec{x}$. Hence,

$$u(\vec{x}) \, u*(\vec{x}) = \int d\vec{f} \, e^{2\pi i \vec{f} \cdot \vec{x}} \frac{2}{\pi} \left\{ \cos^{-1}\left(\frac{\lambda f F}{D}\right) - \left(\frac{\lambda f F}{D}\right)\sqrt{1 - \left(\frac{\lambda f F}{D}\right)^2} \right\}$$

$$\times \exp\left\{ -2 \left[D_{UU}(\lambda f F) \right] \left(\frac{2\pi}{\lambda}\right)^2 \right\}. \qquad (6)$$

By summing the intensities at all points of the image within a circle of radius r, the total image intensity is obtained:

$$I(r) = \int_o^r d\vec{x} \, u(\vec{x}) \, u*(\vec{x}) =$$

$$\int_o^r d\vec{x} \, \frac{2}{\pi} \int d\vec{f} \exp\left[2\pi i \vec{f} \cdot \vec{x} \right] \left\{ \cos^{-1}\left(\frac{(\lambda f F)}{D}\right) - \left(\frac{\lambda f F}{D}\right)\sqrt{1 - \left(\frac{\lambda f F}{D}\right)^2} \right\}$$

$$\times \exp\left\{ -2 \left[D_{UU}(\lambda f F) \right] \frac{2\pi}{\lambda}^2 \right\} \qquad (7)$$

$$= \frac{2}{\pi} \int d\vec{f} \left\{ \cos^{-1}\left(\frac{\lambda f F}{D}\right) - \left(\frac{\lambda f F}{D}\right)\sqrt{1 - \left(\frac{\lambda f F}{D}\right)^2} \right\} \exp\left\{ -2 \left[D_{UU}(\lambda f F) \right] \right.$$

$$\left. \left(\frac{2\pi}{\lambda}\right)^2 \right\} \times \int_o^r x \, dx \int_o^{2\pi} d\theta \exp 2\pi i \, f \, x \cos\theta \, . \qquad (8)$$

Let

$$L = \int_o^{2\pi} d\theta \, e^{2\pi i \, f \, x \cos\theta} \qquad (9)$$

and since

$$L = 2\pi J_o (2\pi f \, x), \qquad (10)$$

$$\int_o^r x \, dx \, L = \int_o^r x \, dx \, 2\pi J_o (2\pi f \, x) = \frac{r}{f} J_1 (2\pi f \, r) \qquad (11)$$

$$I(r) = \int_0^r d\vec{x}\, u(\vec{x})\, u*(\vec{x}) = \frac{2}{\pi} \int d\vec{f} \left\{ \cos^{-1}\left(\frac{\lambda f F}{D}\right) - \left(\frac{\lambda f F}{D}\right) \sqrt{1 - \left(\frac{\lambda f F}{D}\right)^2} \right\} \quad (12)$$

$$\times \exp\left\{ -2\left[D_{UU}(\lambda f F)\right] \left(\frac{2\pi}{\lambda}\right)^2 \right\} \frac{r}{f} J_1(2\pi f\, r)$$

$$= 4r \int_0^\infty df\, J_1(2\pi r\, f) \left\{ \cos^{-1}\left(\frac{\lambda f F}{D}\right) - \left(\frac{\lambda f F}{D}\right) \sqrt{1 - \left(\frac{\lambda f F}{D}\right)^2} \right\} \exp$$

$$\left\{ -2\left(\frac{2\pi}{\lambda}\right)^2 D_{UU}(\lambda f F) \right\}.$$

Since

$$\int_0^\infty r\, J_1(k\, r)\, J_1(k'\, r)\, dr = \frac{1}{k'}\, \delta(k' - k), \quad (13)$$

then

$$\int_0^\infty I(r)\, J_1(2\pi\, f'r)\, dr =$$

$$4 \int_0^\infty df \int_0^\infty r\, J_1(2\pi f\, r)\, J_1(2\pi\, f'r)\, dR \left\{ \cos^{-1}\left(\frac{\lambda f F}{D}\right) - \left(\frac{\lambda f F}{D}\right) \sqrt{1 - \left(\frac{\lambda f F}{D}\right)^2} \right\}$$

$$\times \exp\left\{ -2\left(\frac{2\pi}{\lambda}\right)^2 D_{UU}(\lambda f F) \right\} \quad (14)$$

$$\int_0^\infty I(r)\, J_1(2\pi f'r)\, dr =$$

$$4 \int_0^\infty df\, \frac{1}{2\pi f'}\, \delta(2\pi f' - 2\pi f) \left\{ \cos^{-1}\left(\frac{\lambda f F}{D}\right) - \left(\frac{\lambda f F}{D}\right) \sqrt{1 - \left(\frac{\lambda f F}{D}\right)^2} \right\}$$

$$\times \exp\left\{ -2\left(\frac{2\pi}{\lambda}\right)^2 D_{UU}(\lambda f F) \right\} . \quad (15)$$

$$\delta(2\pi f' - 2\pi f) = \frac{1}{2\pi}\, \delta(f' - f) \quad (16)$$

$$\int_0^\infty I(r) J_1 (2\pi f' r) dr = \frac{4}{(2\pi)^2 f'} \left\{ \cos^{-1}\left(\frac{\lambda f' F}{D}\right) - \left(\frac{\lambda f' F}{D}\right)\sqrt{1 - \left(\frac{\lambda f' F}{D}\right)^2} \right\}$$

$$\times \exp\left\{-2\left(\frac{2\pi}{\lambda}\right)^2 D_{UU} (\lambda f' F)\right\} \quad (17)$$

$$\exp\left\{-2\left(\frac{2\pi}{\lambda}\right)^2 D_{UU} (\lambda f' F)\right\} = \frac{\pi^2 f' \displaystyle\int_0^\infty I(r) J_1 (2\pi f' r) dr}{\cos^{-1}\left(\frac{\lambda f' F}{D}\right) - \left(\frac{\lambda f' F}{D}\right)\sqrt{1 - \left(\frac{\lambda f' F}{D}\right)^2}} \quad (18)$$

Let $\lambda f' F = \ell$

$$D_{UU}(r) = \frac{\lambda^2 \ell n}{8\pi^2}\left[\frac{\left(\frac{\lambda F}{D}\right)\left\{\cos^{-1}\left(\frac{\ell}{D}\right) - \left(\frac{\ell}{D}\right)\sqrt{1 - \left(\frac{\ell}{D}\right)^2}\right\}}{\pi^2 \left(\frac{\ell}{D}\right)\displaystyle\int_0^\infty I(r) J_1\left(2\pi\left(\frac{\ell}{D}\right)\left(\frac{D}{F\lambda}\right)\right) r\, dr}\right] \quad (19)$$

With this equation a set of I (r) measurements can be converted into statistical results on membrane deformation.

D_{UU} (r) can be considered to be a measure of surface roughness and can be used to characterize a given surface. By substituting the values of I (r) and the values for ℓ, λ, and D into the D_{UU} (r) equation, the degree of surface roughness (membrane distortion) between points separated by a distance, r, is obtained.

EXPERIMENTAL SETUP FOR MEASURING MEMBRANE NONFLATNESS

The experimental set-up for measuring membrane nonflatness is shown in Figure III-1. Light from a point source is directed through a pinhole into a collimator, which uses a glass wedge and an f/8 lens (48-inch focal length) to achieve collimation (Figure III-2). Before reaching the membrane, the collimated light passes through an iris, regulating the usable area of the membrane. The light is reflected off the membrane and passes through a diffraction-limited imaging lens (a converging lens with a 52 cm focal length). It is important that the imaging lens have as large a focal length as practical, since this gives diffraction-limited depth of focus (focal length squared times wavelength) that is easy to work with (noncritical). The depth of focus should be about 0.0025 inches. The light then passes through a chopper and is brought to a focus onto a pin-hole, behind which is a rigidly mounted photodetector. The pinhole is

.actually a series of different size circular exposures on a piece of opaque film (the placement and size of the holes must be very accurately controlled). This film is mounted on an adjustable holder which must possess three degrees of motional freedom. The side to side and up and down movements of the holder must be capable of very fine control (better than 0.001-inch increments); the forward and backward movements are not critical and can be done by any means compatible with the other movement controls.

Initially, a 1/10 wavelength optical flat is used to accurately align and adjust the apparatus, expecially the adjustable detector pinhole which is placed for maximum light transmission.

The membrane is replaced by a mirror, and a series of intensity measurements are taken. On the first measurement the vertical and horizontal adjustments are used to obtain maximum intensity with the smallest pinhole. This pinhole must be smaller than the Airy disc so that there is negligible light intensity variation across its diameter. On each subsequent measurement the vertical and horizontal adjustments are used to center the new pinhole pattern in the exact position of the previous pattern. The following 30 readings are taken: 10 readings in increments of 10^{-4}, starting with a 0.0001-inch pinhole diameter; 10 readings in increments of 10^{-3}, starting with a 0.001-inch pinhole diameter; and 10 readings in increments of 10^{-2}, starting with 0.01-inch pinhole diameter. These values are substituted for I (R) in the aberration structure function computer program and that function is computed.
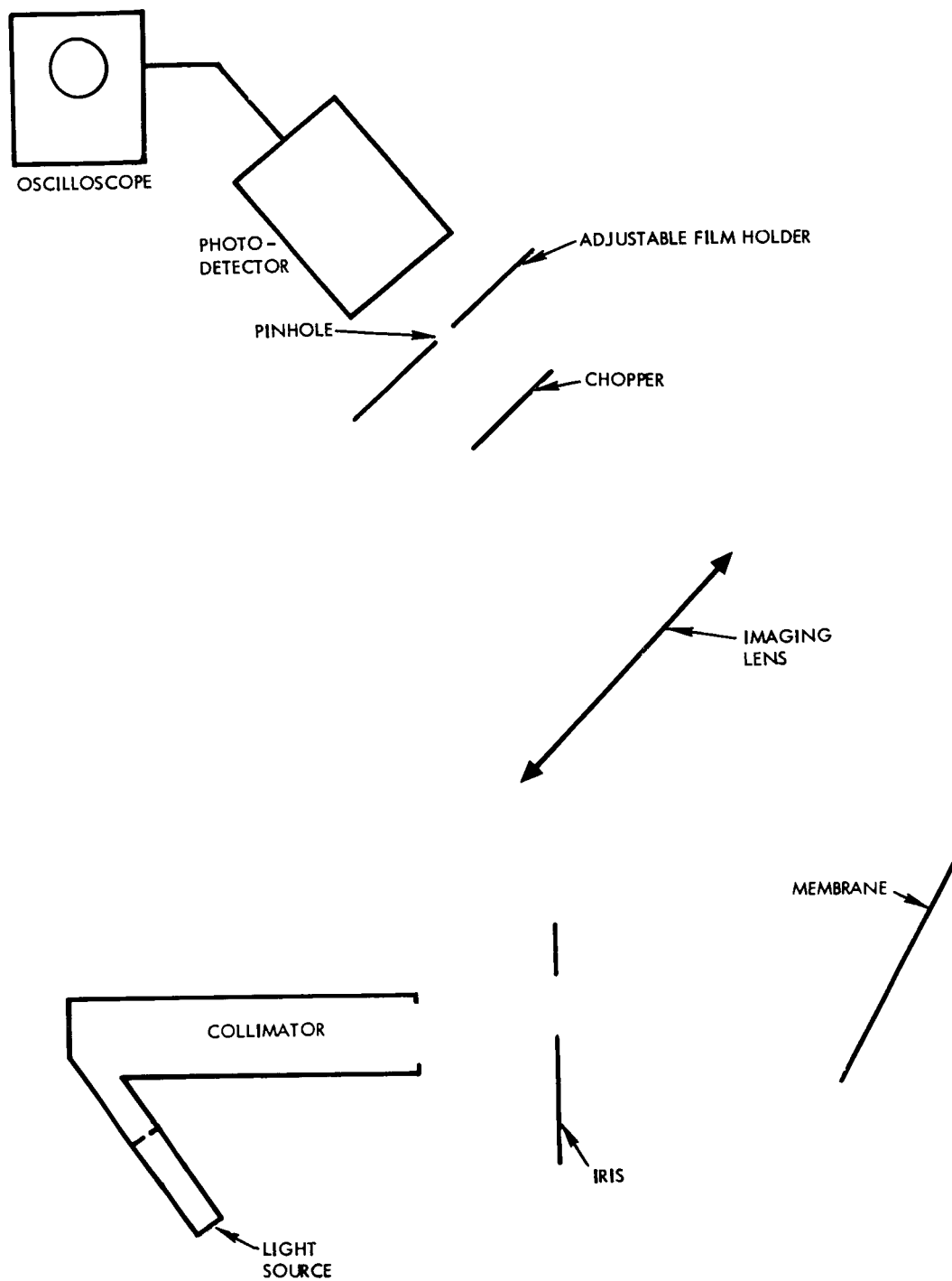
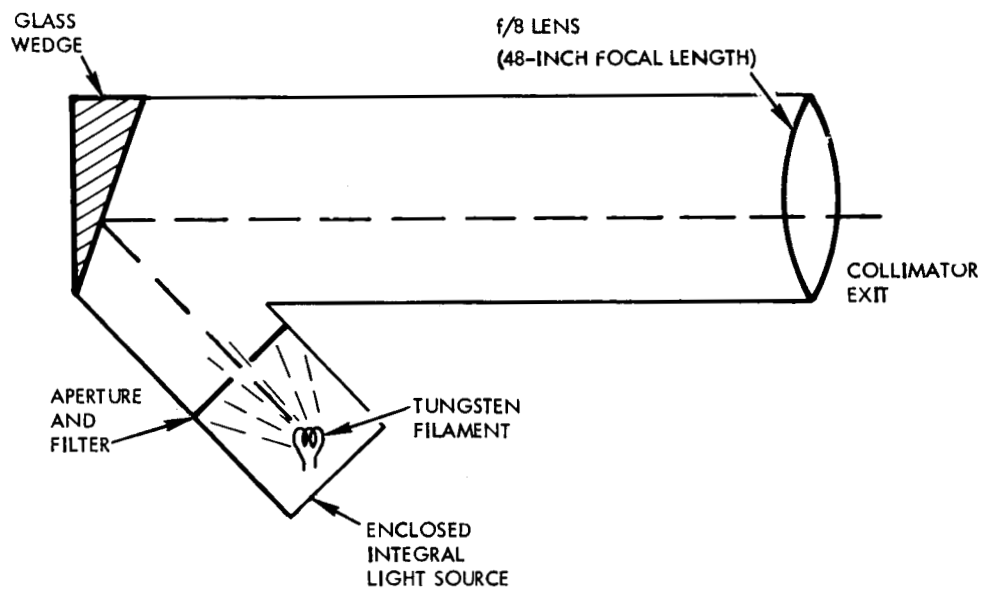Figure III-1. Experimental Setup for Measuring Membrane Nonflatness

SID 65-1026

Figure III-2. Light Directed Into a Collimator

APPENDIX IV

SIGNAL DISTORTION IN A MEMBRANE MODULATOR

INTRODUCTION

With a voltage, V, applied to the membrane modulator, a spherical depression is developed in the membrane mirror, whose sagitta is

$$\Delta = aV^2 \tag{1}$$

where "a" is a constant of proportionality. The intensity of a collimated beam reflected from such a mirror as observed in the far field is

$$I = I_o \frac{\sin^2 \Delta}{\Delta^2} \tag{2}$$

where I_o is the peak light intensity attainable. Assume the applied voltage to be

$$V = b + c \cos \omega t \ . \tag{3}$$

The purpose of this analysis is to determine the magnitude of the fundamental component of I (i.e., the component at ω) and the fractional harmonic distortion present in I, as a function of the proportionality constant "a," the bias voltage "b," and the amplitude of the applied signal voltage "c." The results of this analysis are then interpreted so as to choose parameter values for the MIROS system which will yield the best compromise between maximizing the undistorted signal output and minimizing the fractional harmonic distortion in the signal output.

ANALYTIC PROCEDURE

Combining Equations 1 and 2 yields the relative intensity in the far field as

$$R = \frac{I}{I_o} = \frac{\sin^2 (aV^2)}{(aV^2)^2} \ . \tag{4}$$

For convenience,

$$\theta = \omega t \tag{5}$$

$$G = c/b \tag{6}$$

$$K = ab^2 \ . \tag{7}$$

Using the above definitions, Equation 4 may be rewritten as

$$R = \frac{\sin^2 \left[K(1 + G \cos \theta)^2 \right]}{\left[K(1 + G \cos \theta)^2 \right]^2} \ . \tag{8}$$

It is intended to express R in a Fourier series of the form

$$R = A_o + A_1 \cos \theta + A_2 \cos \theta + \ldots \tag{9}$$

where

A_o = amplitude of d-c term in R

A_1 = amplitude of fundamental term in R

A_n = amplitude of nth harmonic in R

and where

$$A_o = \frac{1}{2\pi} \int_{-\pi}^{+\pi} R(\theta) \, d\theta = \frac{1}{\pi} \int_{o}^{\pi} R(\theta) \, d\theta \tag{10}$$

IV-2

SID 65-1026

$$A_n = \frac{1}{\pi} \int_{-\pi}^{+\pi} R(\theta) \cos n\theta \, d\theta$$

$$= \frac{2}{\pi} \int_{o}^{\pi} R(\theta) \cos n\theta \, d\theta \quad (n \geq 1) \; . \tag{11}$$

The fractional harmonic distortion is defined as

$$D = \frac{\sqrt{\dfrac{A_2^2}{2} + \dfrac{A_3^2}{2} + \dfrac{A_4^2}{2} + \ldots}}{A_1/\sqrt{2}}$$

$$= \frac{\sqrt{A_2^2 + A_3^2 + A_4^2 + \ldots}}{A_1} \tag{12}$$

and is the ratio of the rms harmonic distortion to the rms amplitude of the fundamental component in the received intensity. Although the fractional harmonic distortion can be calculated by directly evaluating A_2, A_3, and all higher order terms of significance, it is more convenient to utilize the following procedure.

Equation 9 may be transposed and averaged over θ to yield

$$\left[R(\theta) - A_o - A_1 \cos \theta \right]^2 = \left[A_2 \cos 2\theta + A_3 \cos 3\theta + \ldots \right]^2 \; . \tag{13}$$

Explicitly writing the average over θ in Equation 24, and noting that the cosine terms on the right side of the equation are orthogonal, yields

$$\frac{1}{2\pi} \int_0^{2\pi} \left[R(\theta) - A_o - A_1 \cos \theta \right]^2 d\theta = \frac{1}{\pi} \int_0^{\pi} \left[R(\theta) - A_o - A_1 \cos \theta \right]^2 d\theta$$

$$= \frac{A_2^2}{2} + \frac{A_3^2}{2} + \frac{A_4^2}{2} + \ldots \tag{14}$$

The fractional distortion can now be evaluated by combining Equations 12 and 14 to yield

$$D = \frac{\sqrt{\frac{2}{\pi} \int_0^{\pi} \left[R(\theta) - A_o - A_1 \cos \theta \right]^2 d\theta}}{A_1} . \tag{15}$$

RESULTS

A_o and A_1 (the d-c and fundamental terms of the Fourier expansion of the relative intensity, respectively) were evaluated by computer integration from Equations 8, 10, and 11. The fractional distortion, D, was evaluated by computer integration from Equation 15, using the previously obtained results for A_o and A_1. Results were obtained for

$$K = ab^2 = 0.5, \ 0.75, \ 1.00, \ 1.25, \ 1.5, \ 1.75, \ 2.00$$

$$G = \frac{c}{b} = \frac{\text{amplitude of sinusoidal modulation signal}}{\text{d-c bias signal}}$$

$$= 0 \text{ to } 1.00 \text{ in } 0.1 \text{ steps}$$

where "a" is defined through Equations 1 and 2.

The information of interest is the behavior of A_1 and of D, as a function of K and G. The most suitable value of K is that which maximizes

the undistorted output-amplitude (= A_1) while simultaneously minimizing the fractional distortion (= D) over all values of G (= the ratio of signal amplitude to d-c bias).

To facilitate understanding of the answers, the plots of both A_1 and D are presented in two groups. In one group, A_1 and D are plotted (in Figures IV-1 and IV-2, respectively) as a function of G, for K = 0.75, 1.0, and 1.25; this group of K parameter values seems most desirable in terms of maximizing A_1 and minimizing D. In the second group, A_1 and D are plotted (in Figures IV-3 and IV-4, respectively) as a function of G, for K = 0.5, 1.0, 1.5, 1.75, and 2; this group of K parameter values (with the exception of K = 1.0, which is included to permit easy reference to the first group of graphs) seems relatively undesirable in terms of maximizing A_1 and minimizing D. The two groups of graphs are plotted separately to avoid confusion of too many lines on a single plot.

CONCLUSIONS

Figures IV-1 and IV-3 show that the undistorted output (= A_1) increases with increasing K, for a specified G, up to K = 1.5; for values of K greater than 1.5, A_1 does not necessarily increase with K at all values of G, and may actually decrease.

Figures IV-2 and IV-4 show that the fractional distortion (= D) is minimized in the region of K = 1.0 to K = 1.25, and becomes significantly greater as K is made less than 1.0 or greater than 1.25.

Since the undistorted amplitude has an insignificant increase when K is increased from 1.25, while the distortion rapidly increases (particularly at small values of G), it appears that the optimum value of K is between 1.0 and 1.25. If K is chosen to be 1.25, the following harmonic distortion characteristics are predicted by Figure IV-2:

$G = \dfrac{\text{a-c amplitude}}{\text{d-c bias}}$	% Distortion
0.1	2.9
0.3	7.9
0.5	12.3
0.7	19.0
0.9	26.1

Achievement of these essentially optimum results can be obtained by adjusting: (1) the membrane tension, and (2) the applied d-c bias, so that

$$K = ab^2 = 1.25$$

where "a" is defined in Equations 1 and 2, and "b" is defined in Equation 3 of this appendix.
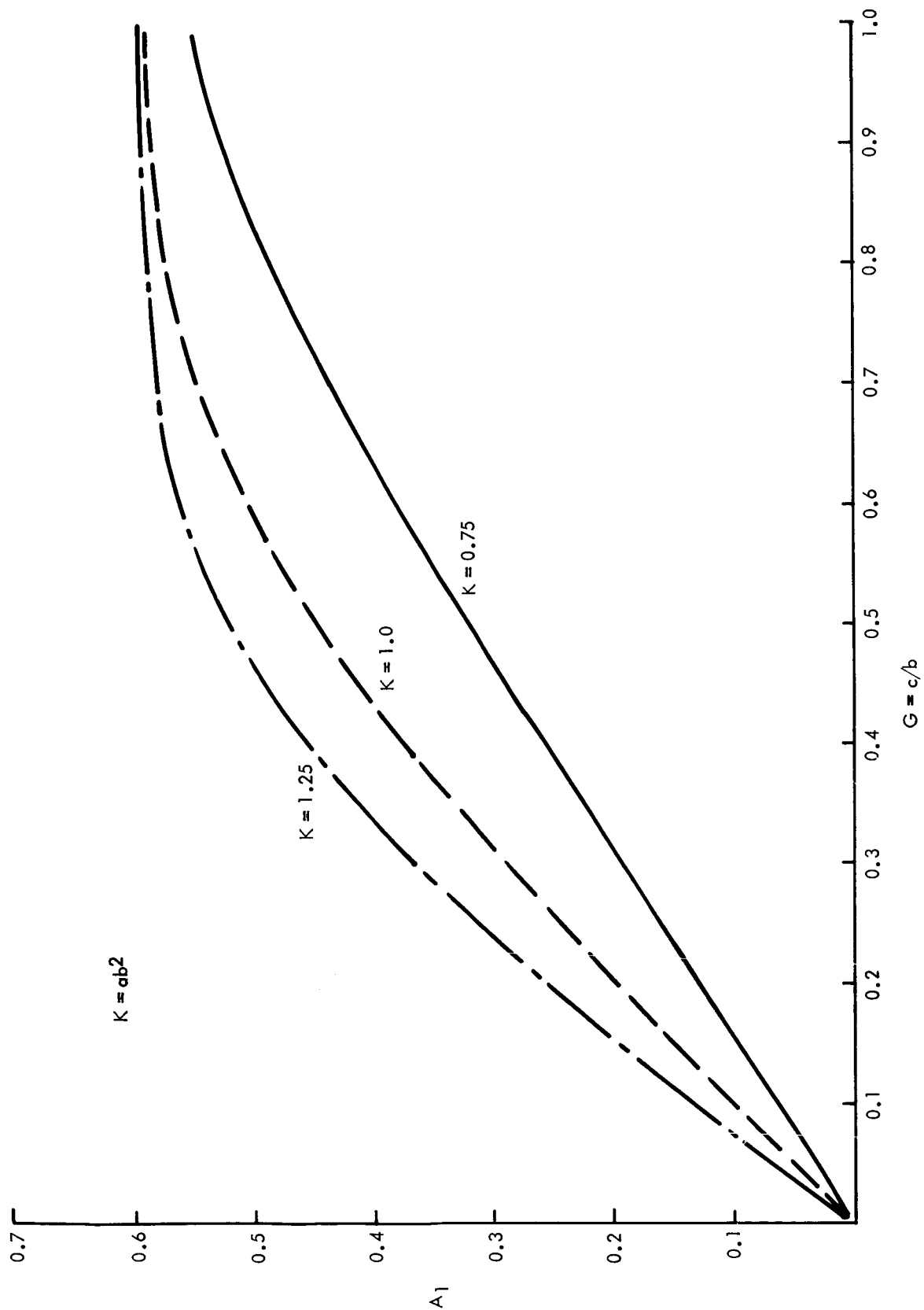
Figure IV-1. Relative Amplitude of Undistorted Output as a Function of G for K
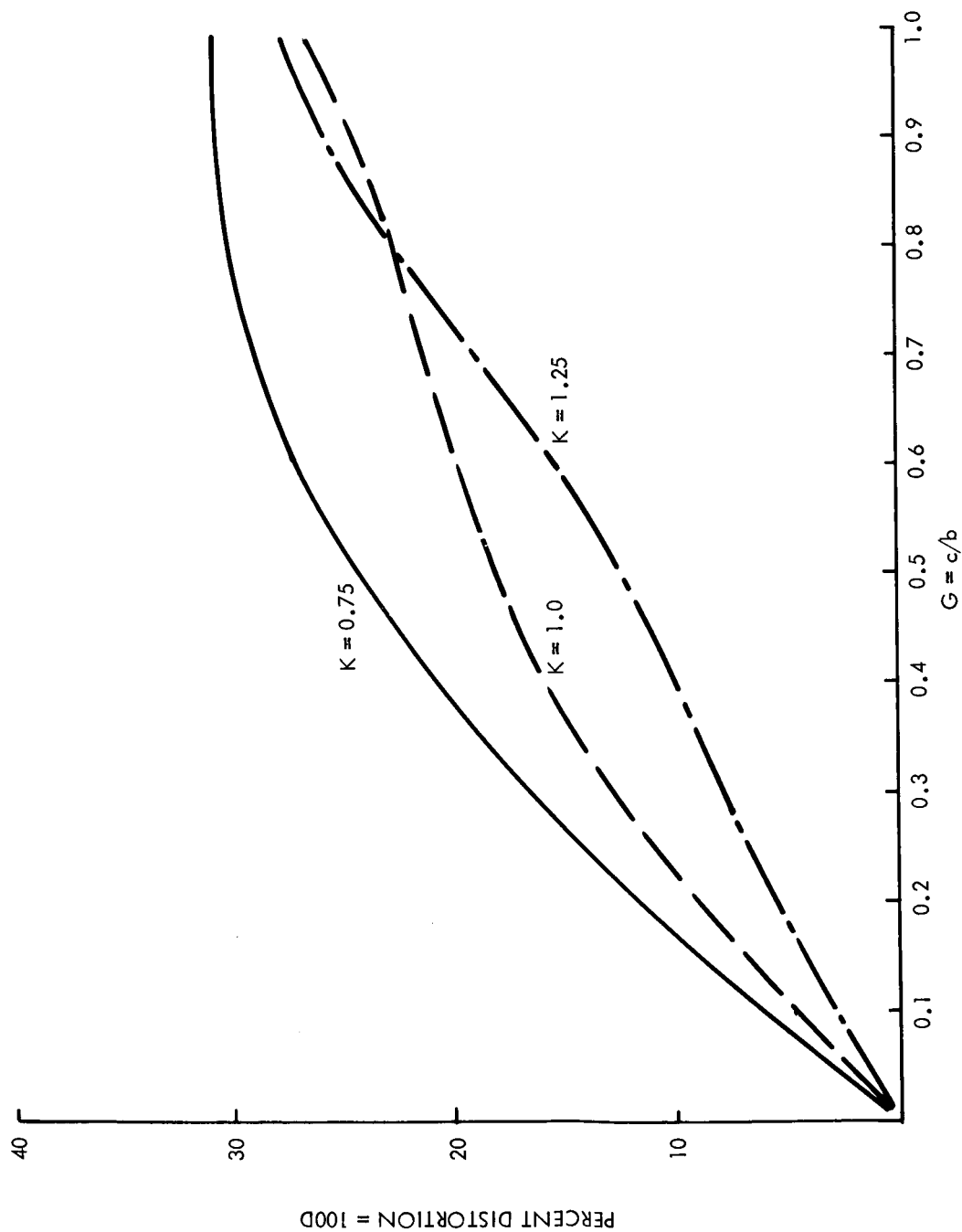Equals 0.75, 1.0, and 1.25

IV-7

Figure IV-2. Percentage Distortion as a Function of G for K Equals 0.75, 1.0, and 1.25
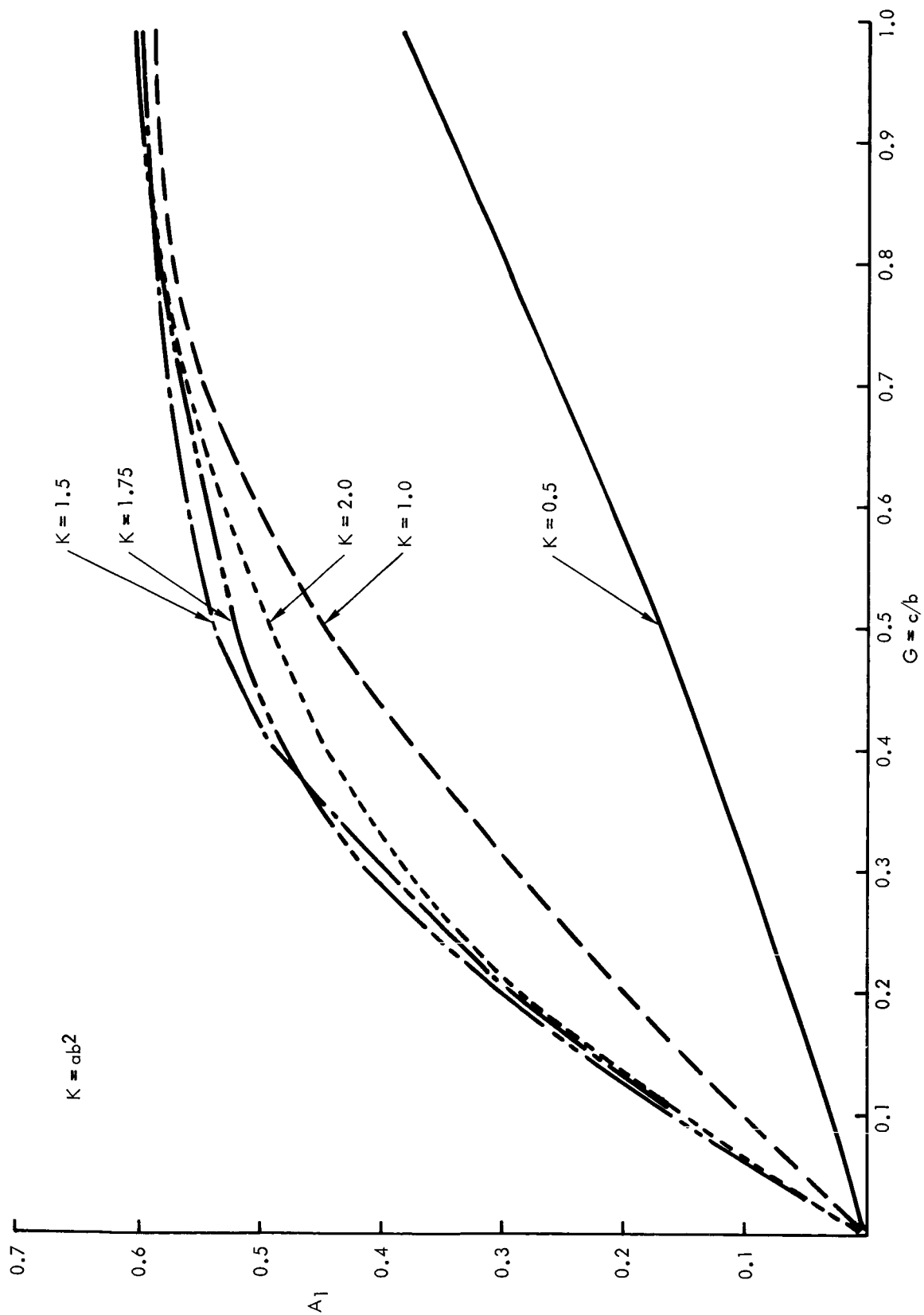
Figure IV-3. Relative Amplitude of Undistorted Output as a Function of G for K Equals 0.5, 1.0, 1.75, and 2.0
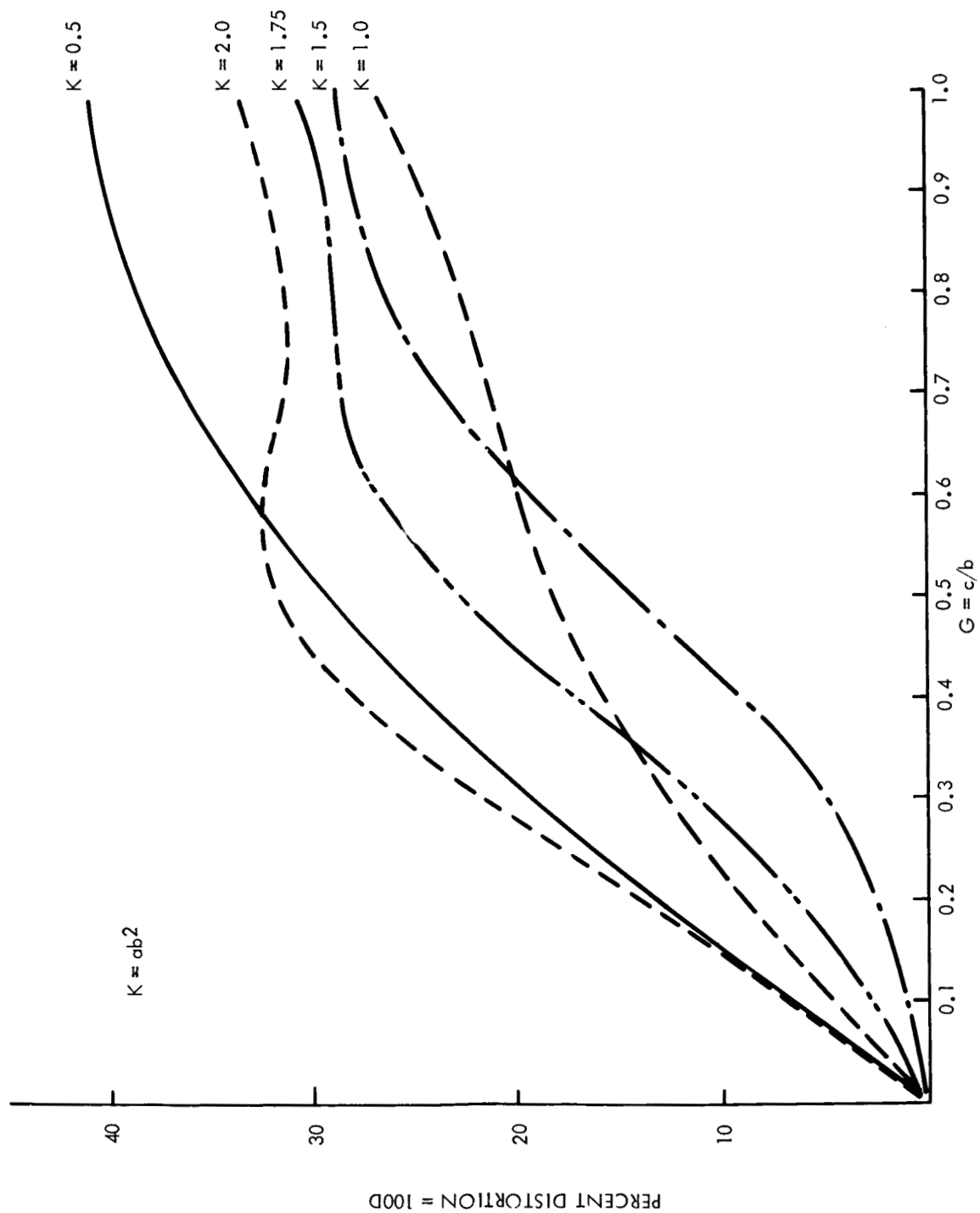
Figure IV-4. Percentage Distortion as a Function of G for K Equals 0.5, 1.0, 1.5, 1.75, and 2.0

APPENDIX V

COMPARISON OF VOLTAGE AND POWER REQUIREMENTS FOR A PIEZOELECTRIC MODULATOR AND A MEMBRANE MODULATOR

The voltage and power requirements of two devices which can be used to convert an electrical signal to mechanical motion are considered in this appendix. The motion in each case is assumed to be a fraction of a wavelength of light, λ, which is taken to be 6328 Angstroms.

The first device is a piezoelectric disk driven by a voltage applied across its thickness. The disk is mounted as the capacitor in a resonant circuit with resonant-frequency-to-bandwidth ratio Q. The resonant frequency, f_o, of the circuit is slightly lower than the piezoelectric disk's lowest mechanical resonance frequency, which will be approximated, however, by f_o. The oscillating voltage of amplitude, V, applied to the resonant circuit produces an oscillating voltage of amplitude, V', across the piezoelectric disk and, because of the piezoelectric effect, causes its thickness to vary by $\pm\delta$. The second device is a pressurized membrane modulator of the type discussed in this report. This device is driven baseband, i.e., over the frequency range from zero to near its resonant frequency. Thus the bandwidth may be assumed equal to the resonant frequency. The voltage applied contains a dc component, V_o, which produces a sagittal displacement,[12] Δ, in addition to an oscillating component, V, which causes the sagitta to vary from $\Delta + \delta$ to $\Delta - \delta$.

It will be shown that the required voltage, V, and the power, P, — or in the case of the membrane device, the volt-ampere product—dissipated in the circuit (each in terms of the radius, r, of the device; the bandwidth, f; and the mechanical motion, δ) will be given by:

$$V = \delta r f / M_v \tag{a}$$

and

$$P = \delta^2 r^3 f^3 / M_p \,, \tag{b}$$

respectively.

---

[12] An applied field produces a spherical depression in the membrane, the extent of which is best discussed in terms of the sagitta.

The quantities M_v and M_p are fundamental parameters of the device, essentially independent of particular dimensions. Obviously, the larger M_v and M_p are, the less the required voltage and power. To the extent of minimizing voltage and power requirements, M_v and M_p may be considered as figures of merit.

Where necessary, the superscripts "Pe" and "M" will be introduced to specify quantities related to the piezoelectric or the membrane device, respectively.

PIEZOELECTRIC DISK

Assuming that the thickness, t, of the piezoelectric disk is less than the radius, r, then the lowest frequency mechanical resonance associated with a thickness change will be due to a transverse wave resonating in a radial mode. With respect to N_R, the appropriate constant of the piezoelectric material, the resonant frequency

$$f_o = N_R / 2r \quad ; \tag{1}$$

hence the operational bandwidth will be

$$f = f_o / Q = N_R / 2rQ \quad . \tag{2}$$

The voltage, V', across the piezoelectric disk necessary to obtain a displacement of δ is

$$V' = \delta / d_{33} \quad , \tag{3}$$

where d_{33} denotes the appropriate electrostrictive coefficient. Equation 2 can be written as $2frQ/N_R = 1$; multiplying Equation 3 by this expression,

$$V' = \frac{\delta}{d_{33}} \, f \, \frac{2rQ}{N_R} = \delta r f \left\{ \frac{2Q}{d_{33} \, N_R} \right\} \quad . \tag{4}$$

V-2

In a resonant circuit operated near resonance, the ratio of the voltage, V', across the capacitor to voltage, V, across the circuit is Q. Thus

$$V = V'/Q = \delta rf \left\{ \frac{2}{d_{33} N_R} \right\} . \tag{5}$$

Substituting Equation 5 for Equation a yields

$$M_v^{pe} = d_{33} N_R / 2 . \tag{6}$$

For the power calculation, observe that the capacitance of the piezo-electric disk is

$$C = k \epsilon_o \pi r^2 / t , \tag{7}$$

where ϵ_o is the dielectric constant of free space ($= 8.85 \times 10^{-12}$), and k is the relative dielectric constant of the piezoelectric material. The peak energy stored in the capacitor is $1/2\, C\, (V')^2$, and since the energy dissipated per cycle is $1/Q$ times the peak energy stored, then the total power dissipated is

$$P = \frac{1}{2} C(V')^2 f_o \frac{1}{Q}$$

$$= \frac{1}{2} k \epsilon_o \pi r^2 \frac{1}{t} \frac{\delta^2}{d_{33}^2} f$$

$$= \delta^2 r^3 f^3 \left\{ \frac{1}{2} k \epsilon_o \pi \frac{1}{t} \frac{1}{d_{33}^2} \right\} \left\{ \frac{1}{r} \right\} \left\{ \frac{2rQ}{N_R} \right\}^2 \tag{8}$$

$$= \delta^2 r^3 f^3 \left\{ 2\pi k \epsilon_o \frac{r}{t} \left(\frac{Q}{d_{33} N_R} \right)^2 \right\} .$$

Referring to Equation b,

$$M_p^{pe} = (d_{33} N_R)^2 \frac{t}{r} \bigg/ Q^2\, 2\pi k \epsilon_o . \tag{9}$$

The quantity, t/r, is being considered a fundamental constant of the material since it is limited to values less than unity. (If it is greater than unity a thickness resonance will occur at an even lower frequency than that given by Equation 1.) Typically t/r would be less than $1/2$.

PRESSURIZED MEMBRANE

For this case, a membrane will be considered with a pressure, P; a gap size (i.e., the depth of the pressure chamber), t; and a membrane area density, ρ. The tensional restoring forces are considered to be negligible compared to the pressure restoring force. Under these assumptions the resonant frequency will be

$$f = \frac{1}{2\pi}\sqrt{\frac{0.4\,p}{\rho t}} \quad .$$ (10)

The voltage required will be

$$V_o + V = \sqrt{\frac{(\Delta + \delta)\,pt}{\epsilon_o}} \quad ,$$ (11a)

$$V_o - V = \sqrt{\frac{(\Delta - \delta)\,pt}{\epsilon_o}} \quad ,$$ (11b)

where V_o has been defined as the dc component of voltage, and V, the ac driving voltage. Since the motion δ is small compared to the bias sagitta we may approximate

$$\sqrt{\Delta \pm \delta} \simeq \sqrt{\Delta}\left(1 \pm \frac{1}{2}\,\frac{\delta}{\Delta}\right) \quad .$$ (12)

Thus

$$V = \frac{1}{2}\sqrt{\frac{pt}{\Delta\,\epsilon_o}}\,\delta$$

$$= \delta r f\,\frac{1}{2}\sqrt{\frac{pt}{\Delta\,\epsilon_o}}\left\{\frac{1}{r}\;2\pi\sqrt{\frac{\rho t}{0.4\,p}}\right\}$$

V-4

$$= \delta r f \left\{ \pi \frac{t}{r} \sqrt{\frac{\rho}{0.4 \, \Delta \, \epsilon_o}} \right\} \qquad . \tag{13}$$

Again, referring to Equation a,

$$M_v^m = \frac{1}{\pi} \frac{r}{t} \sqrt{\frac{0.4 \, \Delta \, \epsilon_o}{\rho}} \qquad . \tag{14}$$

Again it is justifiable to considering r/t as a parameter of the material since it is practical considerations that limit allowed values.

Strictly speaking there is almost no power dissipated in the membrane device. There is a certain amount of power required, however, which must be dissipated in the driving circuitry; this can be estimated as being the product of the rms ac volts and rms ac amperes across the membrane capacitor. The ac current has an amplitude $2\pi \bar{f}$ CV where $\bar{f}$ is the average frequency, which is (1/2)f. Thus the power dissipation is

$$P = \frac{\pi f C V}{\sqrt{2}} \frac{V}{\sqrt{2}}$$

$$= \frac{\pi}{2} f \epsilon_o \pi \frac{r^2}{t} \frac{1}{4} \frac{\rho t}{\Delta \epsilon_o} \delta^2$$

$$= \frac{\pi^2}{8} \frac{\rho}{\Delta} f r^2 \delta^2 \quad , \tag{15}$$

where Equation 7 has been used for the capacitance, with k set equal to unity since the gap is filled with a gas. Equation 15 can be recast as

$$P = \frac{\pi^2}{8} \frac{\rho}{\Delta} f^3 r^3 \delta^2 \left(4\pi^2 \frac{\rho t}{0.4 \, p} \right) \frac{1}{r}$$

$$= \delta^2 r^3 f^3 \left\{ \frac{5}{4} \pi^4 \frac{t}{r} \frac{\rho}{\Delta} \right\} \qquad . \tag{16}$$

Hence, referring to Equation b,

$$M_p^M = \frac{4}{5\pi^4} \frac{r}{t} \frac{\Delta}{\rho} \quad .$$ (17)

NUMERICAL EVALUATION

The constants needed to evaluate Equations 6, 9, 14, and 17 are

$$d_{33} = 3.74 \times 10^{-10} \text{ meters/volt}$$

$$N_R = 2.05 \times 10^3 \text{ cps-meters}$$

$$k = 1.7 \times 10^3$$

(These values are applicable for PZT-5),

$$\Delta = \frac{\lambda}{4} = 1.58 \times 10^{-7} \text{ meters,}$$

(chosen to provide an optimum bias for operation as a modulator), and

$$\rho = 8.9 \times 10^{-3} \text{ kilograms/meter}^2,$$

(based on a nickel membrane on-micron thick). For the piezoelectric disk assume $(t/r)^{PE}$ to be $1/2$, which is nearly the optimum value and also corresponds to a reasonable set of dimensions. For the membrane take $(r/t)^M$ to be 500, which is a value typical of those which have been obtained. Based on these values,

$$M_v^{PE} = 3.84 \times 10^{-7} \qquad\qquad M_p^{PE} = 3.09 \times 10^{-6} Q^{-2}$$

$$M_v^M = 1.26 \times 10^{-6} \qquad\qquad M_p^M = 7.3 \times 10^{-5}$$ (18)

These results, combined with the Equations a and b, yield the desired relationships. Moreover, the quantities in Equation 18 can be used, in the sense discussed in the text, as figures of merit for the two devices. It need only be noted here, that although the Q of the

piezoelectric driving circuit has not been fixed, it cannot be made smaller than unity (it will probably be at least greater than 3), and the larger Q is made, the smaller the piezoelectric power-figure of merit,

APPENDIX VI

COMPARISON OF RETRODIRECTIVE CONFIGURATIONS

In this appendix, expressions are developed for the required area of the modulator elements in a corner reflector retrodirector and in a focusing system retrodirector. The treatment will be restricted to very simple versions of each type of retrodirector. The analysis of the corner reflector retrodirector is based upon the three mirror reflector configuration shown in Figure VI-1. For simplicity in the analysis, the possibility that the "tips" of the corner reflector might be trimmed has not been considered, as this should not affect our results in any significant manner. For the focusing system retrodirector, the analysis is based upon corrected reflective optics of the type shown in Figure VI-2. The choice of this type of focusing system is predicated on the need to achieve operation over a reasonably large field-of-view.

Since all the retrodirected light is reflected from all three mirrors of the corner reflector, it is sufficient that only one surface be modulated to insure that all the retrodirected light will be modulated. If only a fraction, ρ, of the mirror area a_{mir}^{CR} is modulatable, then only a fraction, p, of the retrodirected light will be modulated. The relation between the mirror area and entrance aperture area a_{ent}^{CR} is given by

$$a_{mir}^{CR} = \frac{1}{\sqrt{3}} a_{ent}^{CR} \tag{1}$$

Defining the effective collection area A_{eff}^{CR} as the product of a_{ent}^{CR}, the optical loss L_{opt} and the fraction, p, of the area that is modulated, and letting A_{mod}^{CR} denote the modulator area,

$$A_{mod}^{CR} = p\, a_{mir}^{CR} \quad , \tag{2}$$

and

$$A_{mod}^{CR} \Big/ p = \frac{1}{\sqrt{3}} A_{eff}^{CR} \Big/ p\, L_{opt} \tag{3}$$

VI-1
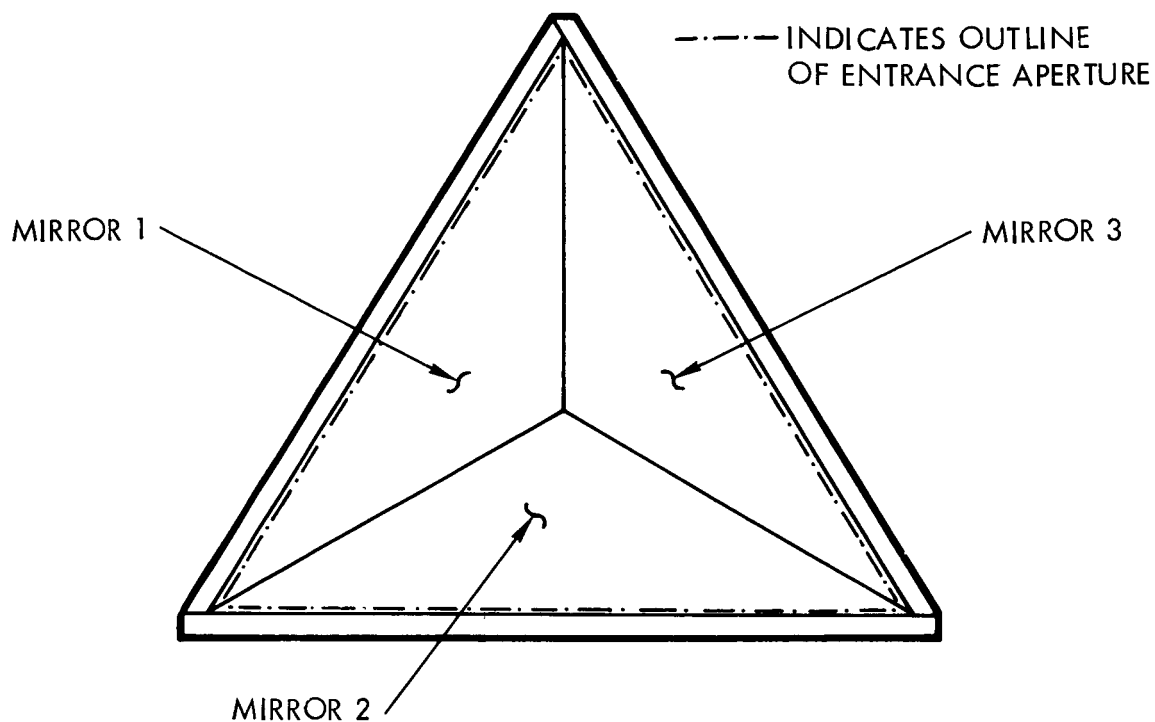
Figure VI-1. Three-Mirror Corner Reflector Configuration
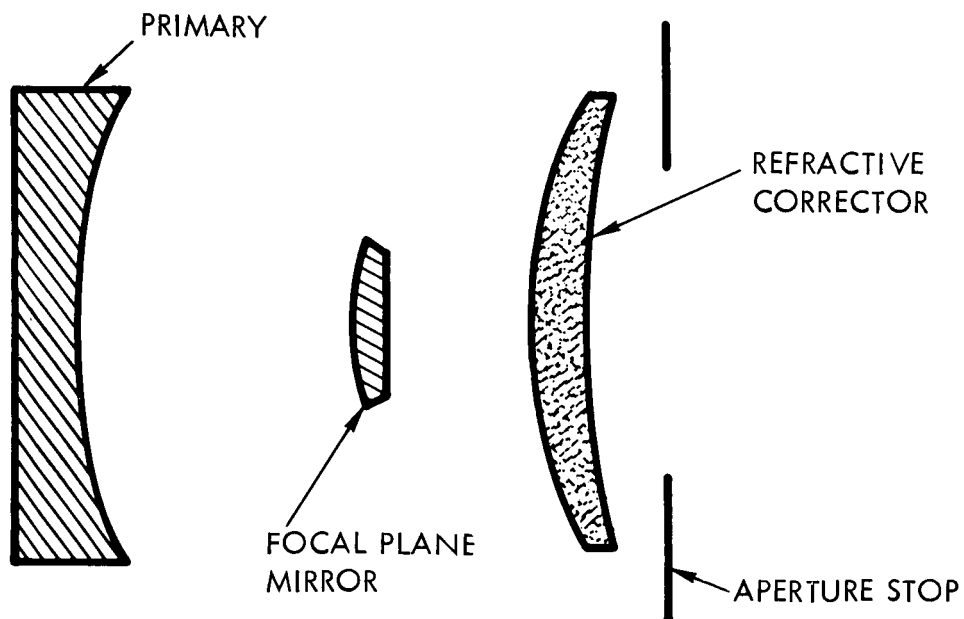
Figure VI-2. Focusing System Retrodirector

VI-2

$$A^{CR}_{mod} = A^{CR}_{eff} \Big/ \sqrt{3} \; L_{opt} \quad . \tag{4}$$

In the focusing system retrodirector, shown in Figure VI-2, the focal plane mirror must be modulatable in order to modulate the retro-directed light. The area A^{FS}_{mod} of the focal plane mirror determines the solid angle Ω over which the system will be retrodirective. If the focal length of the optical system is F, then

$$\Omega \simeq A^{FS}_{mod} \Big/ F^2 \quad . \tag{5}$$

If the entrance aperture area (considering blockage due to such elements as the focal plane mirror) is denoted as a^{FS}_{ent}, and the effective area A^{FS}_{eff} as $a^{FS}_{ent} \times L_{opt}$, where L_{opt} is the optical loss factor, then

$$A^{FS}_{mod} = \frac{F^2}{a^{FS}_{ent}} \frac{A^{FS}_{eff}}{L_{opt}} \Omega \quad . \tag{6}$$

The effective f-number, f_{eff}, of an optical system (considering only the usable, i.e., unblocked, portion of the collector area) can be shown to satisfy the relationship;

$$\frac{F^2}{a^{FS}_{ent}} = \frac{4}{\pi} \left(f_{eff} \right)^2 \quad , \tag{7}$$

so that

$$A^{FS}_{mod} - \frac{4}{\pi} \left(f_{eff} \right)^2 A^{FS}_{eff} \Omega \Big/ L_{opt} \quad . \tag{8}$$

Obviously, the smaller the effective f-number, effective collection area and field-of-view, the smaller the modulator area will be.

Strictly speaking Equations 4 and 8 are the results sought in this appendix. For the purpose of recasting the results into a form in which the two devices can be compared, some measure of the solid angle over which the corner reflector operates must be introduced. A corner reflector, however, has no well defined solid angle of operation. As the angle from normal incidence increases the effective collection area decreases as can be seen in Figure VI-3. There is some retrodirection over a full 2π steradians but it would not be reasonable to consider this to be the field-of-view. A more meaningful definition would be based on considering a corner reflector with an aperture area, a, at normal incidence, and then define the effective solid angle of retrodirection as

$$\Omega^{CR}_{eff} = \frac{1}{a} \int_0^{2\pi} d\phi \int_0^{\pi/2} \sin\theta \, d\theta \, a\,(\theta, \phi) \; , \tag{9}$$

where $a\,(\theta, \phi)$ is the effective area at incidence angle (θ, ϕ). Numerical evaluation of this integral, based on the data of Figure VI-3 yields,

$$\Omega^{CR}_{eff} = 0.63 \text{ steradians.} \tag{10}$$

Now multiplying and dividing by Ω^{CR}_{eff} in Equation 4,

$$A^{CR}_{mod} = \frac{4}{\pi} (0.89)^2 A^{CR}_{eff} \Omega^{CR}_{eff} \Big/ L_{opt}. \tag{11}$$

In this form the equation for the corner reflector modulator area is directly comparable to Equation 8 for the focusing system modulator area.
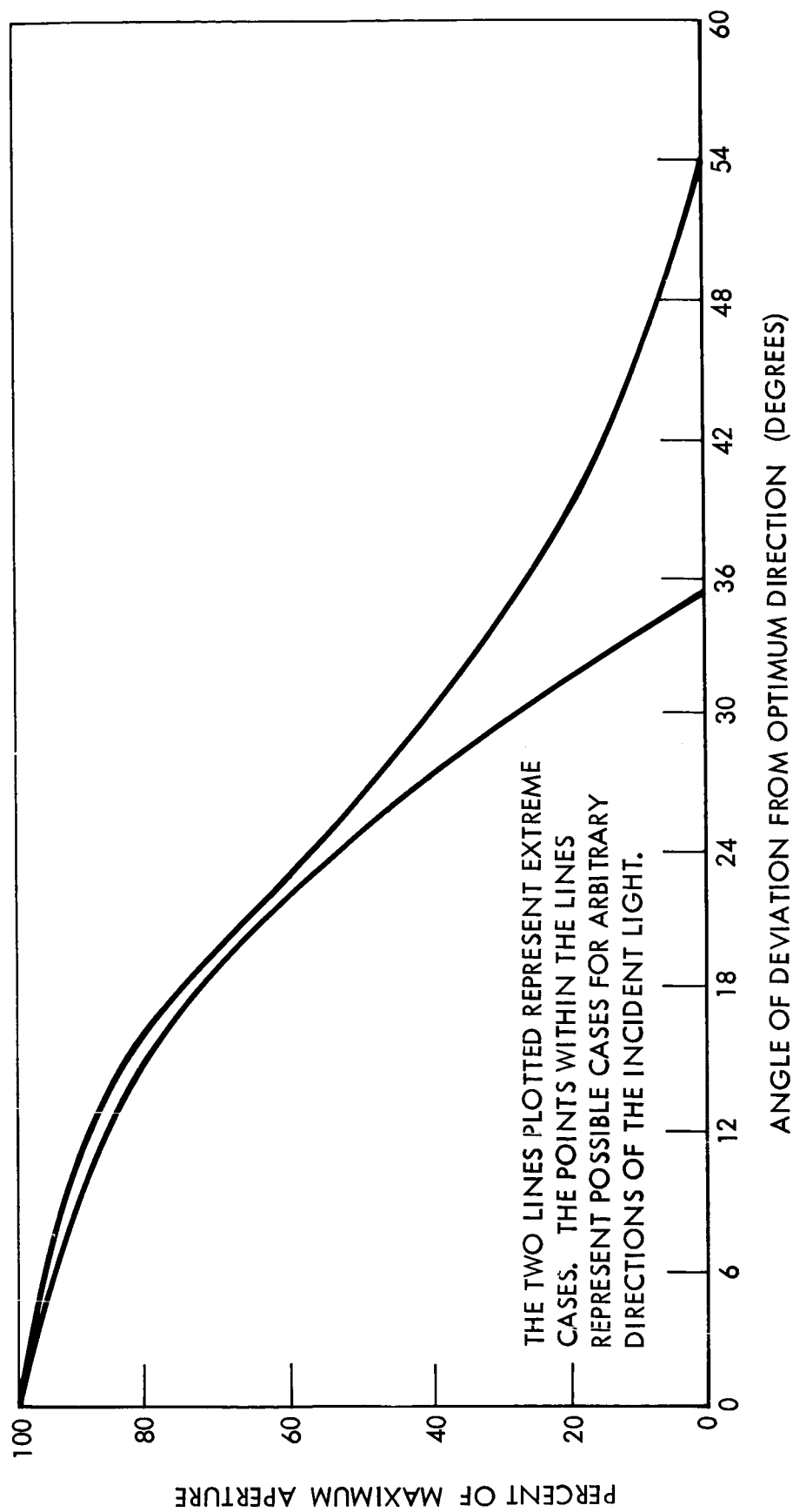
VI-4

Figure VI-3. Percentage of Maximum Aperture Versus Angle of Deviation From Optimum Direction

THE TWO LINES PLOTTED REPRESENT EXTREME
CASES. THE POINTS WITHIN THE LINES
REPRESENT POSSIBLE CASES FOR ARBITRARY
DIRECTIONS OF THE INCIDENT LIGHT.

ANGLE OF DEVIATION FROM OPTIMUM DIRECTION (DEGREES)

PERCENT OF MAXIMUM APERTURE